TRACE ELEMENT PARTITIONING BETWEEN APATITE AND KIMBERLITE-LIKE MELTS – IMPLICATIONS FOR VOLATILE DEGASSING AND FORMATION OF DIFFERENT KIMBERLITE FACIES

by

Richard Chow

Submitted in partial fulfilment of the requirements
for the degree of Master of Science

at

Dalhousie University
Halifax, Nova Scotia
October 2021

Dalhousie University is located in Mi'kma'ki, the
ancestral and unceded territory of the Mi'kmaq.
We are all Treaty people.

TABLE OF CONTENTS

LIST OF TABLES

LIST OF FIGURES

ABSTRACT

Kimberlites are the deepest mantle magmas to reach the surface of the Earth and the hosts of the major primary diamond deposits. The enigmatic nature of kimberlites owing to poorly constrained triggers of kimberlite magmatism, melt composition, and crystallization conditions are mostly limited by unknown composition of volatiles. The content and ratio of H_2O and CO_2 are important parameters of magma emplacement as they are essential for mantle melting and rapid ascent of kimberlites. Volatiles also greatly affect diamond preservation in kimberlites during the ascent to the surface. Apatite is often used as an indicator mineral of magma degassing in other magmatic systems. As such, it should be applied to kimberlite systems to study the volatile behavior during emplacement. Partitioning of trace elements between apatite and a melt is also sensitive to the carbonate component in the melt. This makes apatite a useful indicator for the evolution of melt composition and fluid during kimberlite ascent and emplacement. However, the existing estimates for the trace elements partitioning in apatite give discrepant estimates for carbonatitic melts and estimates for silicate melts use compositions that differ greatly to kimberlites. This study presents experimentally determined trace element partition coefficients (D) between apatite and synthetic analogues of kimberlite (SiO_2 11-23 wt. %) and carbonatite melts (SiO_2 <1 wt. % and 4.5 wt. %). Experiments were conducted in piston-cylinder apparatus at 1150°C, 1250°C, 1350°C, at 1 and 2 GPa, and at oxygen fugacity -3.97, 0.27, 4.83 log units relative to fayalite-magnetite-quartz buffer. Results show the increase of compatibility for rare earth elements (REE) with increase in SiO_2 of the melt and the relationship between the concentration of other elements (Si, Ca, Na, S) in apatite and its REE content uptake using substitution mechanisms. No effect of temperature, pressure, water content, and oxygen fugacity on partition coefficient was present in these low SiO_2 melts. I apply the results to apatite from two types of kimberlite pipes: (i) Class 1 composite kimberlite pipes from Orapa cluster (Botswana) with hypabyssal coherent and volcaniclastic kimberlite facies and (ii) Class 3 kimberlite pipes from Ekati Mine (Northwest Territories, Canada) filled with effusive coherent kimberlites in Leslie pipe and both volcaniclastic and coherent kimberlites in Boa pipe and discuss how changes in SiO_2 content of kimberlite melt affect apatite saturation. I further apply the experimentally determined partition coefficients to model the composition of evolved kimberlite melt using published bulk rock and apatite compositions in kimberlites.

LIST OF ABBREVIATIONS AND SYMBOLS USED

°C	degrees Celsius
apfu	atoms per formula unit
BSE	back scattered electron
CK	coherent kimberlite
CL	cathodoluminescence
CCO	carbon dioxide-carbon oxide
D	partition coefficient
DA	Durango apatite
EMPA	electron microprobe analysis
EVK	extrusive volcaniclastic kimberlite
ECK	extrusive coherent kimberlite
*f*O2	oxygen fugacity
GPa	gigapascal
HFSE	high field strength element
HM	hematite–magnetite oxygen fugacity buffer
HREE	heavy rare earth element
IW	iron-wustite oxygen fugacity buffer
ICK	intrusive coherent kimberlite
KPK	Kimberley-type pyroclastic kimberlite
LA-ICPMS	laser ablation-inductively coupled plasma mass spectrometry
LILE	large ion lithophile element
LREE	light rare earth element
MREE	middle rare earth element
mm	millimeter
NNO	nickel–nickel oxide oxygen fugacity buffer
PK	pyroclastic kimberlite
ppm	parts per million
REE	rare earth elements
RRO	rhenium-rhenium oxide oxygen fugacity buffer

LIST OF ABBREVIATIONS AND SYMBOLS USED

RVK	resedimented volcaniclastic kimberlite
SA	synthetic apatite
SEM	scanning electron microscopy
T	Temperature
μm	micrometer
WDS	wavelength dispersive spectroscopy
wt. %	weight percent
VK	volcaniclastic kimberlite

Chapter 1: Introduction

1.1 Role of volatiles in kimberlite emplacement

Kimberlites are a group of igneous rocks which are volatile-rich, potassic, ultrabasic, olivine-rich, and silica-undersaturated (Scott Smith et al., 2018). They originate from a deep asthenosphere mantle source, which makes them an important transportation mode for mantle diamonds. Kimberlite magmatism produces a variety of surface forms and lithological facies (Scott Smith, 2008). There are two broad subdivisions of the textural-genetic classification of kimberlites, which include coherent kimberlite coherent kimberlite (CK) and volcaniclastic kimberlite (VK). Coherent kimberlite is further classified as either intrusive (ICK) and extrusive (ECK) coherent kimberlites. Volcaniclastic kimberlite is further classified as pyroclastic kimberlite (PK), resedimented pyroclastic kimberlite (RPK), and epiclastic volcanic kimberlite (EVK) (Scott Smith et al., 2013). Pyroclastic kimberlite can have different mechanisms of deposition/emplacement and further comprises of two facies subclassification, KPK (Kimberley-type pyroclastic kimberlite) and FPK (Fort à la Corne-type pyroclastic kimberlite) (Scott Smith et al., 2013). While FPK is a typical pyroclastic rock deposited from an eruption column, the origin of KPK is still poorly understood (Scott Smith, 2008). Combination of different kimberlite facies in a pipe-shaped body is grouped into three classes (Figure 1.2) (Field and Scott Smith, 1999). Class 1 are very large and deep pipes (>3 km) with an upper volcaniclastic zone, followed by a middle steeply-sided in-filled zone of KPK and RPK faces that transitions to a lower coherent facies zone. Class 2 pipes are shallow (<500 m), bowl-shaped, and dominated by FPK facies. Class 3 pipes are typically small with deep steep-sided craters (>500 m) and are filled with mostly RVK facies and a small amount of PK (Skinner and Marsh, 2004).

This diversity in kimberlite geology is proposed to be due to either the different types of country rock that the magma encounters (Field and Scott Smith, 1999) or different kimberlite volatile compositions (Skinner and Marsh, 2004). The first model suggests that environments with competent igneous country rocks impede kimberlite magma ascent leading to pressure build ups that eventually break apart to the surface forming class 1 kimberlites. Ascending kimberlite magma in environments with poorly consolidated sediments interact with the water in the sediments causing a phreatomagmatic eruption forming class 2 kimberlites (Field and Scott Smith, 1999). The second model relates the emplacement mechanism to the influence by the volatile composition of the magma. A CO_2-rich kimberlite magma rises closer to the surface and interacts with water to form a phreatomagmatic eruption. Whereas H_2O-rich magmas exsolve volatiles at depth which drive its eruption (Skinner and Marsh, 2004). Fluid exsolution is suggested to be the main component in driving the ascent of kimberlite magma. Experiments have shown that assimilation of the mantle minerals orthopyroxene and clinopyroxene by carbonate-rich magma at >2.5 GPa results in exsolution of CO_2 (Russell et al., 2012; Stone and Luth, 2016). The resulting decrease in magma density leads to a buoyancy driven ascent. Secondly, near surface decompression also results in a decrease in solubility of CO_2 and H_2O (Moussallam et al., 2016). Providing that the kimberlite magma retains considerable amounts of CO_2 and H_2O gases into the upper crust, this second stage of exsolution is abrupt and forms the distinctive pipe shape through eruption (Moussallam et al., 2016).

Ekati Mine kimberlites located in the Lac de Gras kimberlite field in Northwest Territories, Canada, are predominantly VK pipes with some less common CK pipes. The CK occurs as either small dykes and sills at the base of the pipes or as fill in some kimberlite pipes

such as Leslie, Grizzly, and Aaron (mentioned in this study). The latter of these are called pipe-fill CK (Nowicky et al., 2008). The formation of Ekati Mine CK has been interpreted to be the result of pyroclastic processes. The reduced CO_2 content in pipe-fill CK compared to the CK from dykes suggest that degassing during eruption occurred (Nowicki et al. 2008). Whole-rock geochemical analyses also show enrichment of Ni and SiO_2 content and depletion of Ti, Nb (incompatible element in the liquid component), and CO_2 in pipe-fill CK relative to root zone dykes, which reflect removal of the liquid component in the magma from the separating of fine pyroclastic particles during eruption events. Pyroclastic kimberlite showed a similar depletion trend in incompatible elements (Ti, Nb, V) and an enrichment in SiO_2 but to a greater degree. The lack of any pyroclasts suggest that the pyroclastic origin of CK must represent the coalescence of fluidal magma clasts produced from lava fountain type eruptions (Nowicki et al. 2008). Additionally, this shows that different facies have unique compositions likely linked to their differing formation processes. Non pipe-fill CK forming sheets, dykes, or sills (commonly referred to as hypabyssal) is the result of the kimberlite magma cooling associated with early exsolution (Moussallam et al., 2016). The onset of crystallization at depth forms the intrusive CK structures and slows the magma ascent. A surface level eruption can be prevented in the case where the exsolved gases separate from the magma and ascend on their own (Moussallam et al., 2016).

The origin of KPK in the diatreme of class 1 kimberlite pipes has been a matter of contention for a long time. The largest diamond mines in Botswana and Russia are also of this class of kimberlite pipe. Currently there are two contrasting hypotheses for the formation process of KPK kimberlites facies, which constitutes the diatreme part of class

1 kimberlites. One hypothesis suggests a “top-down” model where initial near surface phreatomagmatic eruptions related to rising kimberlite magma form a surface crater as a precursor to a pipe (Lorenz, 1975; Sparks et. al, 2006; Sparks et. al 2013). The pipe walls fall inward as the pipe widens and deepens via continued eruptions and the material is entrained within kimberlite flows. Eventually infilling overtakes the ability of the flow to remove entrained material and the pipe is filled. The pipe reaches atmospheric exit pressures below surface allowing for magma at the pipe base to exsolve volatiles which forms a central fluidized region in the pipe. This fluidized region driven by continued release of volatiles and fresh magma at the base of the kimberlite pipe mixes the diatreme material while removing finer ash and eroding the pipe walls (Sparks et. al, 2006; Sparks et. al 2013). In contrast, another hypothesis suggests a “bottom-up” approach where there is a concentrated front of volatiles ahead of a rising magma column (Clement, 1982; Clement and Reid, 1989; Field and Scott Smith, 1999). This magma-gas column rises, migrates into and breaks through the country rock until reaching the surface. Once surface breakthrough occurs, the magma column degasses and volatiles within the country rock migrates inward towards the magma column. This results in brecciation of the country rock and further exsolving of volatiles from the magma continues. Fluidization of the magma occurs, and the degassing front migrates downwards. This fluidization process excavates the pipe and infills it simultaneously (Clement, 1982; Clement and Reid, 1989; Field and Scott Smith, 1999)). Both hypotheses indicate a relation to volatiles where the main driving force for emplacement of KPK kimberlites is the exsolving of volatiles from the magma. Thus, a close examination into the volatiles of kimberlites can provide a better understanding on the emplacement processes of different kimberlites.

Volatiles are poorly constrained in kimberlites due to alteration and loss during emplacement. Therefore, it is important to find direct evidence in kimberlite magma for the history of volatile exsolution. Surface features of diamonds can provide a record of volatile presence and composition (Fedortchouk et al., 2010). In Ekati Mine kimberlites, kimberlites which diamonds show low-relief resorption surface features indicative of fluid-rich magma also have olivines with high content of OH defects. This suggests the presence of a fluid rich melt during emplacement which contribute to rapid ascent rates (Fedortchouk et al., 2010). Study of two kimberlite bodies from Orapa kimberlite cluster, Botswana, show that different kimberlite lithologies contain diamonds with different resorption features. KPK facies contain diamonds with low-relief glossy surfaces indicative of H_2O-rich fluid, while CK facies contain rough corroded surfaces indicative of resorption by melts (Fedortchouk et al., 2017). This implies an effect of fluid presence on kimberlite lithology and diamond population. However, diamond is an extremely rare mineral in kimberlites, as it is absent from some kimberlite facies, and predicting its abundance and features are the aim of exploration efforts.

Trace element partitioning behaviour between apatite and kimberlite liquid can help to constrain the behaviour of volatiles in kimberlite magma. For example, if an early fluid phase is to separate from the magma, then a depletion in certain trace elements such as Pb, Cs, and large ion lithophile elements (LILE) would be observed and recorded in apatite (Guzmics et al. 2008). In the proposed hypothesis of KPK formation by Field and Scott Smith (1999), the loss of volatiles such as CO_2 during the eruption of the kimberlite should gradually make the magma more silicic in composition. This increase in SiO_2 component

will affect apatite by increasing its trace element compatibility and as well as apatite saturation in the magma (Watson and Green, 1981; Green and Watson, 1982).

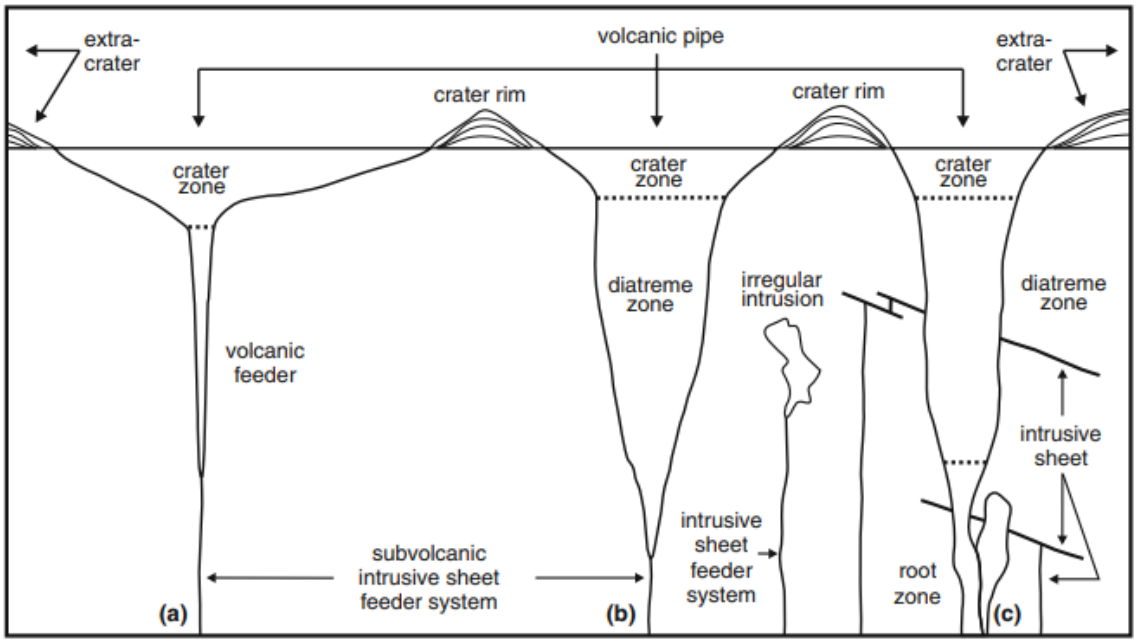

Figure 1.1: Diagram of different kimberlite classes. (a) Class 3 kimberlite (b) Class 2 kimberlite (c) Class 1 kimberlite (Scott Smith, 2013).

1.2 Composition of Apatite

The general structural formula of the apatite supergroup of minerals is $M_{10}(ZO_4)_6X_2$ (where M = Ca, Sr, Pb, Na, etc.; Z = P, As, Si, V, etc.; X = F, OH, Cl). While there are a wide range of apatite species, the most common subgroup found in nature are the calcium-phosphate apatites which have the general formula of $Ca_5(PO_4)_3$(F, Cl, OH). In particular, there is fluorapatite, chlorapatite, and hydroxylapatite, where fluorapatite is a ubiquitous accessory mineral phase in many igneous, metamorphic, and sedimentary rocks (Fleet and Pan, 2002). The $P6_3/m$ space group of fluorapatite is tolerant to a range of elemental substitutions. The hexagonal crystal structure of apatite contains three cation sites. There are two Ca sites in apatite, a larger nine-fold coordinated Ca1 site and a smaller seven-fold

coordinated Ca2 site. Many divalent cations (Sr^{2+}, Ba^{2+}, Mn^{2+}, Pb^{2+}...) can substitute into the Ca sites. In addition, monovalent (Na^{+}), trivalent (REE^{3+}), tetravalent (Th^{4+}, U^{4+}), and hexavalent (U^{6+}) cations can also substitute for Ca. The tetrahedral phosphate site can be substituted by a variety of tetrahedral anion groups (SiO_4^{4-}, AsO_4^{3-}, VO_4^{3-}, etc.). Of particular interest are trace and rare earth elements (REE) since apatite can accommodate significant amounts of them. REE occupy the Ca sites in apatite with larger Light rare earth elements (LREE) preferring the Ca1 site and smaller Heavy rare earth elements (HREE) the Ca2 site (Chakhmouradian et al, 2017). The main substitution mechanisms involving REE for Ca^{2+} are as follows (Fleet and Pan, 2002):

$$REE^{3+} + Na^{+} = 2\ Ca^{2+} \qquad (1)$$

$$REE^{3+} + Si^{4+} = Ca^{2+} + P^{5+} \qquad (2)$$

$$2\ REE^{3+} + \square = 3\ Ca^{2+} \qquad (3)$$

$$REE^{3+} + S^{2-} = Ca^{2+} + F^{-} \qquad (4)$$

Substitution (1) is the coupled substitution of monovalent cations (such as Na^{+}) and REE. In mechanism (2), the coupled substitution of REE in the Ca site and Si^{4+} for P^{5+} site can occur. An increase in SiO_2 content in the melt would increase the substitution of REE into the structure (2). In omission substitution (3), a vacancy in the Ca site can accommodate the incorporation of REEs. Mechanism (4) exchange S^{2-} or O^{2-} ions for F^{-} to compensate for the Ca and REE charge difference (Fleet and Pan, 2002).

1.2.1 Previous experimental studies of partitioning of trace elements in apatite

Partition coefficient (D) is calculated as the ratio of element concentration (C) in the mineral to that of the liquid (melt), where for an element (i), $Di = Ci_{min} / Ci_{liq}$, and is an important tool for interpreting the surrounding environment of the mineral during its growth (Blundy and Wood, 2003). Partition coefficient is highly dependent on the composition of the melt from which the mineral is crystallizing from as well as the temperature (Watson and Green, 1981). It has been shown that D_{REE} in apatite depend on the melt polymerization (Prowatke and Klemme, 2006). The effect of H_2O and oxygen fugacity (for elements with variable valence state) is not well known. Numerous studies have focused on determining the partitioning behaviour of trace elements in apatite using natural samples and experimental studies. The D constrained from natural samples, different experimental conditions, and for different melt compositions are summarized in Figure 1.2 and Table 1.2. Study of trace element partitioning into apatite in basaltic to andesitic silicate melts showed that the REE and Sr are compatible in apatite (Figure 1.2; Prowatke and Klemme, 2006), while LILE such as Cs, Rb, and Ba are highly incompatible ($D << 1$). Uranium, Th, and Pb have Ds of approximately 1. Prowatke and Klemme (2006) determined that Ds of REE are most affected by the melt composition itself where an increasing polymerization of the melt (higher SiO_2 wt.% of the melt) correlated to an increase in apatite/melt Ds by one order of magnitude. The halogen F and H_2O content of the melt is found to have no effect on the D_{REE}. Cl is a halogen that preferentially partitions into the fluid phases present during the degassing of a melt (Piccoli and Candela, 2002). It is reported that for melts with 40-68 wt.% SiO_2, an increase in temperature decreases D_{REE}

but does not affect the partitioning of Sr. The effect of temperature is less pronounced towards lower SiO_2 melt content (Watson and Green, 1981).

The study by Hammouda, et. al (2010) found that the partitioning of REE into apatite in carbonatite melts is dependent on apatite silica content. Apatites that contain 3.5-5 wt.% SiO_2, have $D_{REE}^{apatite/carbonatite}$ values of 1.5 to 4 (Figure 1.2). In apatites containing 0.2 wt.% SiO_2, REE are found to be incompatible (Hammouda et. al, 2010). The high field strength elements (HFSE) U^{4+}, Th^{4+}, and Y^{3+} are compatible in SiO_2-rich apatite giving D values of ≥ 5 for Th and ≥ 2 for Y. Sr is incompatible in apatite with D values ≈ 0.5. No effect of pressure on the compatibility behavior of trace elements in apatite was observed (Watson and Green, 1981, Hammouda et. al, 2010). Klemme and Dalpe (2003) examined apatite Ds in carbonatite melt and found that the middle rare earth elements (MREE) (Sm, Gd) are preferentially incorporated into apatite relative to light (LREE) (La, Ce, Pr) and heavy (HREE) (Lu). The melt composition is found to be a significant factor in influencing the D_{REE}. A decrease in silica-content along with an increase in Ca and P in melts results in the decrease of D_{REE} (Klemme and Dalpe, 2003). However, there is an inconsistency between the findings of the two experimental studies with carbonatite composition studies. Hammouda et. al (2010) obtained much higher compatibility ($D_{REE}^{apatite/carbonatite} = 1.3\text{-}3.17$) than the study by Klemme and Dalpe (2003) ($D_{REE}^{apatite/carbonatite} = 0.34\text{-}0.49$). The two studies used different experimental conditions used such as pressure or temperature (Table 1.2). Results of Hammouda et. al (2010) are similar to $D_{REE}^{apatite/carbonatite}$ estimated by Guzmics et al. (2008) in natural samples using apatite hosted carbonatite melt inclusions in clinopyroxenite xenoliths from lamprophyres in Hungary. They observed similar but

slightly lower REE compatibility compared to Hammouda et. al (2010) ($D_{REE}^{apatite/carbonatite}$ = 1.18-2.15).

All previous experimental studies used melt compositions either more SiO_2-rich than kimberlitic or pure carbonate melt. Presently there are no trace element partitioning studies between apatite and kimberlitic melts. Furthermore, existing estimates of trace element partitioning in carbonatitic melts from experimental studies and in natural samples produced overall contradictory partition coefficient values (Chakhmouradian et. al, 2017).

1.2.2 Apatite in kimberlites

Apatite is a common groundmass mineral in kimberlites (Mitchell, 1986). Due to its structure it has a high affinity towards incorporating halogens, sulfate, carbonate, strontium, and the REEs (Piccoli and Candela, 2002) via substitution mechanisms previously mentioned. As such, it has routinely been used to shed light on the evolutionary history in other magmatic systems such as carbonatite complexes and ignimbrites (Chakhmouradian et. al, 2017; Boyce and Hervig, 2008). In kimberlites, apatite occurs as discrete subhedral-euhedral hexagonal prisms or aggregates of elongate acicular apatite (Soltys et al., 2017; Milligan, 2017). Also reported is the average composition of kimberlitic apatite being mostly fluorapatite with 2.2±0.4 wt.% F, 55.0±1.0 wt.% CaO and 38.9±0.7 wt.% P_2O_5. Minor elements include 0.77±0.48 wt.% SiO_2, 2.1±1.4 wt.% SrO ≤0.4 wt.% Na_2O, ≤0.5 wt.% FeO, and ≤0.3 wt.% Ce_2O_3 (Soltys et al., 2017). Apatites from the Lac de Gras kimberlite field have been documented as spherulites with compositions that classify it as Sr-apatite and Sr-rich carbonate-hydroxylapatite (Chakhmouradian, 2002).

Previous work using apatite as an indicator of kimberlitic fluid and magmatic composition has been conducted on six kimberlite pipes at Ekati Mine (Koala, Panda, Leslie, Misery, Grizzly and Beartooth) and the Snap Lake kimberlite dyke (Milligan, 2017). These pipes differ in their lithologic features which suggests diverse eruption styles and thus likely variation in volatile behaviour, that can be correlated to specific apatite textures and composition. Leslie and Grizzly are CK, while the remaining four kimberlite pipes are volcaniclastic: Panda (RVK), Koala (FPK) , Misery (FPK) and Beartooth (RVK). The diversity of apatite ranging in different forms and abundance that was observed in the study is outlined here. Leslie kimberlite contain abundant groundmass apatite. They occur as euhedral prisms and laths 30-40 μm in size with monticellite inclusions (Milligan, 2017). In Koala kimberlite, apatite grains are observed in a matrix of fine-grained silicates, phlogopite laths, and large perovskite grains. The majority of the apatite grains are 50-80 μm in size and take the shape of subhedral prisms with smooth grain boundaries. The other type of texture is apatite grains with irregularly-shaped edges of monticellite. Apatite from Grizzly kimberlite occurs as anhedral grains 5-30 μm in size embedded in the groundmass (Milligan, 2017). Some hexagonal grains show zonation and edge resorption. Panda kimberlite apatites are abundant subhedral grains 10-20 μm in size with no inclusions or zoning. Groundmass apatite from Misery and Beartooth kimberlites are very low in abundance. The rare grains that are observed occur as a small cluster of fine grain apatite laths (Milligan, 2017). Zonation is observed under cathodoluminescence (CL) in apatite from Leslie, Koala, Grizzly, and Panda. CL spectra peak in Koala reveals the peaks of Ce^{3+}, Sm^{3+}, and Eu^{2+}. Apatite grains from Leslie show spectra peaks corresponding to Ce^{3+} and Dy^{3+}. One apatite grain from Grizzly showed corresponding CL spectra peaks to Ce^{3+},

Dy^{3+}, Tb^{3+} and Sm^{3+}. The Ekati kimberlite apatite compositions can be divided into three groups: hydroxyapatite (Panda), fluor-hydroxyapatite (Leslie and Grizzly), and fluorapatite (Koala and Grizzly) (Milligan, 2017). Strontium and LREE contents are low in apatite from Koala and highest in Leslie (0.2 apfu Sr and 0.1 apfu LREEs). Grizzly shows two distinct groups where high F content apatites are similar to Koala in the field of low Sr and LREEs. The low F apatites are closer to the high Sr and LREEs field of Leslie apatites (Milligan, 2017). Panda apatites have high LREE content similar to Leslie but with significantly lower Sr. Apatite from Leslie and Panda are the most enriched in Sr, Ba and Th, and depleted in Y relative to the other kimberlites. Koala apatites consistently show a depletion in Nb compared with the other kimberlites (Milligan, 2017). Snap Lake kimberlite has three varieties of apatites. One variety (Type 1) occurs as groups of radial acicular apatites with inclusions. Type 2 apatites encompasses subhedral crystals hosted in carbonate veins and Type 3 apatite are non-poikilitic subhedral crystals. Type 1 and 2 apatites have high Sr content and low LREE, while Type 3 has moderate Sr and higher LREE.

It is evident that apatite is unique across different kimberlite bodies; however, changes in the crystallisation, morphology, and chemistry of apatite with depth in a kimberlite pipe or in different facies of the same pipe have not been studied. However, they may provide an important record of crystallization conditions and volatiles in kimberlite pipes during their emplacement in the crust.

A number of processes that accompany ascent and emplacement of kimberlite magma may affect partitioning of trace elements in apatite. Another factor to account for in the natural apatite studies is the effect of crustal contamination particularly in class 1 kimberlites.

Crustal xenoliths can make up 10-30% in volume of kimberlites (Clement, 1982). Such contaminants are typically higher in SiO_2, Al_2O_3, and Na_2O. In this case, an increase of Si content of the melt could be due to assimilated crustal country rock and in turn increases the partitioning of REE into apatite. In addition, loss of volatiles during eruption will decrease the carbonate content while the incorporation of country rock xenoliths will increase Si content of the melt thus increasing compatibility of REE in apatite.

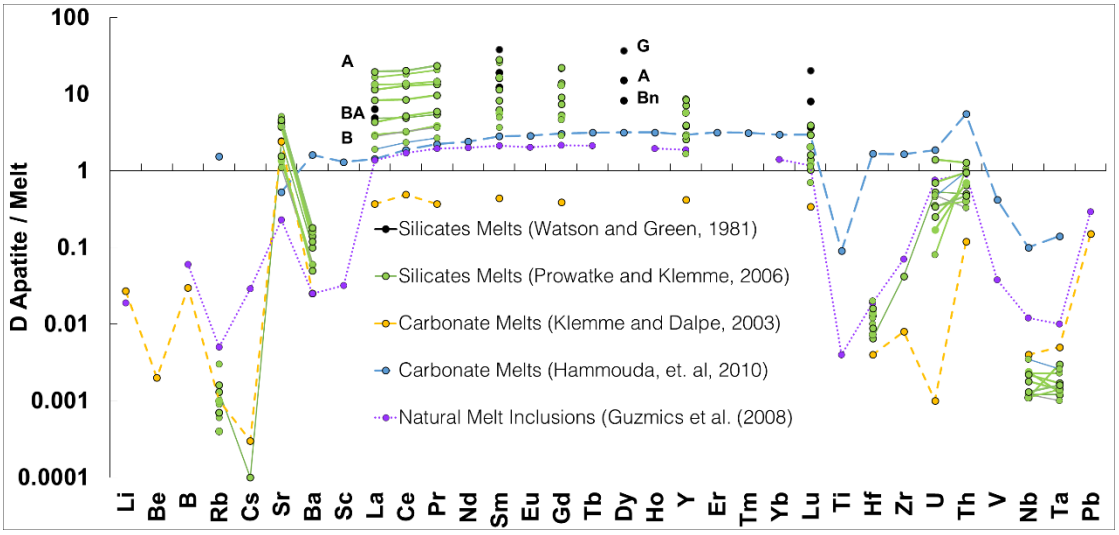

Figure 1.2: Trace element partition coefficients between apatite and various melts from previous experimental studies (data from Prowatke and Klemme, 2006; Watson and Green, 1981; Klemme and Dalpe, 2003; Hammouda et. al, 2010; Guzmics et al., 2008). A = andesite, BA = basaltic andesite, B = basalt, G = granite, Bn = basanite.

Table 1.2: Summary of the apatite trace element partition coefficient data from various experimental studies and their parameters

Melt Composition	Experimental Conditions	Trace element Partition Coefficient Data in Study
Silicate (Basanite) (Prowatke and Klemme, 2006)	1.0 GPa 1250 °C	Cs, Rb, Ba, La, Ce, Pr, Sm, Gd, Lu, Y, Sr, Zr, Hf, Nb, Ta, Y, U, Pb, Th
Silicate melt (basanite, basaltic andesite, andesite, granite) (Watson and Green, 1981)	0.75-2.0 GPa 950-1120 °C	La, Sr, Sm, Lu, Dy
Carbonate Melt (Klemme and Dalpe, 2003)	1.0 GPa 1250 °C	Li, Be, B, K, Cs, Rb, Ba, Th, U, Nb, Ta, La, Ce, Sr, Pr, Hf, Zr, Sm, Gd, Y, Lu, Pb
Carbonate Melt (Hammouda, et. al, 2010)	6 GPa 1350-1380°C	La, Ce, Pr, Nd, Sm, Eu, Gd, Tb, Dy, Ho, Er, Tm, Yb, Rb, Sr, U, Th, Pb

1.3 Objectives of this study

1. To determine the effect of fluid on the emplacement mode of different kimberlite facies by correlating its influence on the variation in apatite abundance, crystal morphology, and chemical composition in complex kimberlite pipes filled with coherent and volcaniclastic kimberlite facies.
2. Obtain the partition coefficients of trace elements between apatite and melts that are close in composition to the estimates of kimberlitic melt and examine the role of temperature, pressure, and fO_2 on trace element partition coefficients for the compositional range of kimberlites.
3. Use the obtained trace element partition coefficients to model the composition of late kimberlite melt in different coherent and volcaniclastic kimberlite facies.
4. Use estimated apatite solubility and partition coefficients to evaluate changes in fluid content in kimberlites and use it for predicting diamond preservation potential of a kimberlite.

Chapter 2: Methods

2.1 Kimberlites Samples

The kimberlite pipes examined in this study are located in the Lac de Gras kimberlite field (Ekati Mine) in Northwest Territories, Canada, and in the Orapa kimberlite cluster in Botswana. The samples were collected from borehole DDH in Boa kimberlite pipe, LDC9 from Leslie kimberlite pipe (Ekati Mine, Canada) (Figure 2.1), one drillhole from AK15 kimberlite intrusion, and three boreholes (H002, H003, and H004) from BK1 kimberlite pipe from the Orapa kimberlite cluster (Botswana) (Figure 2.2). In each kimberlite, samples were collected from different depths in the drillhole with a focus on transitions between the facies (Table 2.1; Fig. 2.3, 2.4, 2.5). Well preserved kimberlite samples were selected from each borehole to provide adequate coverage of its depth profile. Selected samples cover all kimberlite facies present in each borehole. Of the 5 examined boreholes, 23.7-234.6 m depth range was sampled in coherent Leslie kimberlite (Figure 2.3, A), 30-84.8 m depth range in pyroclastic and coherent facies from Boa pipe (Figure 2.3 B), 56.16-151.7 m depth range in magmatic (coherent) AK15 intrusion (Figure 2.4), and in three drill holes (36.7-54.33 m, 8.64-124.41m, and one with no known depth profile (Figure 2.5)) in two coherent and one Kimberly-type pyroclastic facies from BK1 kimberlite pipe. These kimberlite pipes were selected based on their lithologies. Leslie and Boa are class 3 kimberlites where Leslie consists entirely of CK and Boa contains both CK and PK. AK15 and BK1 are class 1 kimberlites. AK15 kimberlite is entirely CK. BK1 kimberlites contains multiple facies including two different CK and one KPK facies. The different geological features of these kimberlites suggests different volatile behaviour and offer an opportunity

to examine the variation of apatite in different kimberlites facies and identify any correlations with the emplacement processes and fluid exsolution.

Diamond studies from BK1 and AK15 kimberlites show very different styles of resorption features on diamonds from CK and KPK facies (Fedortchouk et al., 2017) indicating differences in the fluid behavior during the formation of these facies suggesting different emplacement processes. Here we examine if these differences are accompanied by textural and compositional differences of the groundmass apatite. While diamond surface features can be a proxy of fluid presence and composition, diamond's rarity restricts its usage. Therefore, apatite, as a common kimberlite mineral, is a useful alternative for providing information on the processes and conditions during kimberlite emplacement.

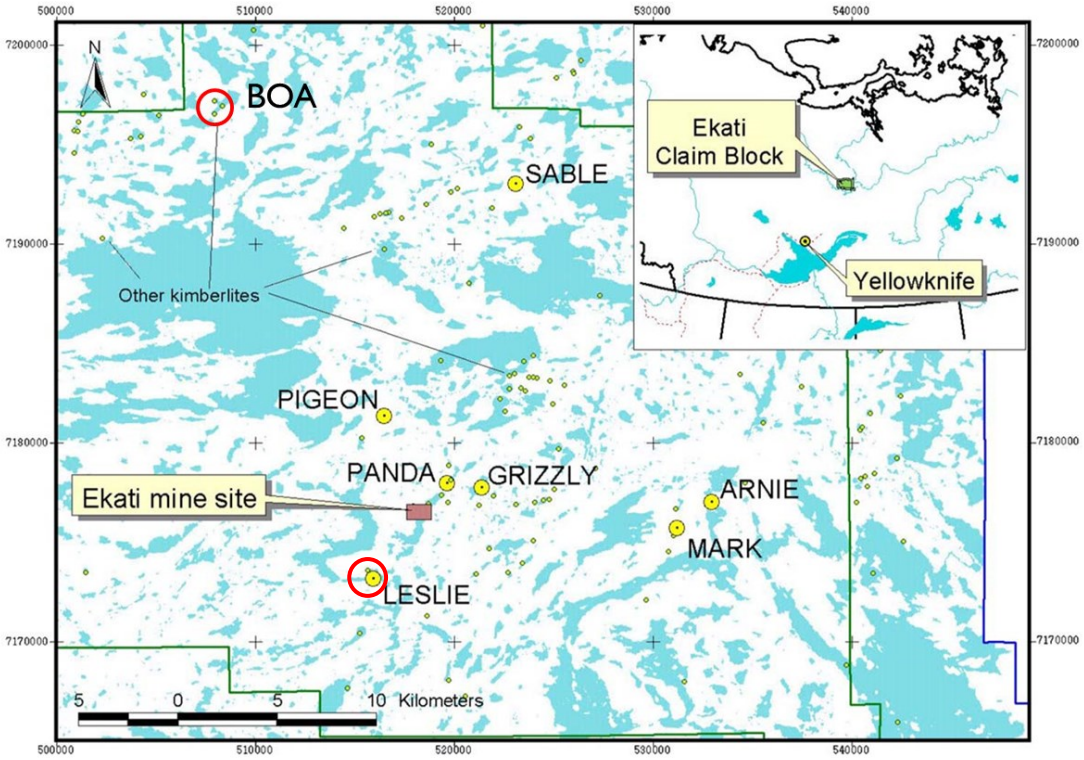

Figure 2.1: Location map with the location of Leslie and Boa kimberlites (modified from Menzies et. al, 2004).

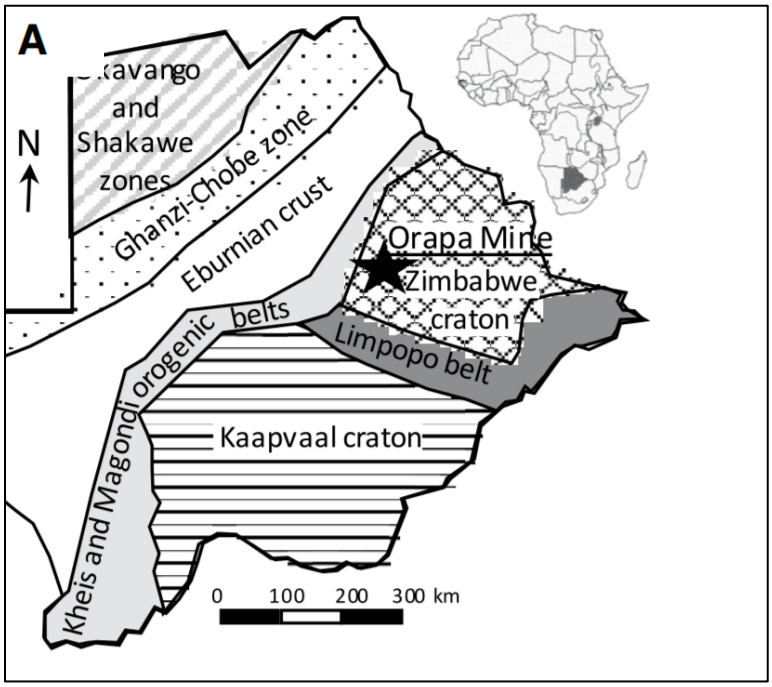

Figure 2.2: Star indicates map location of Orapa kimberlite cluster in Botswana (Fedortchouk et al., 2017).

Table 2.1: Summary of the number of samples selected from each location for this project and their kimberlite facies and depth. Abbreviated terms: ECK (extrusive coherent kimberlite), ICK (intrusive coherent kimberlite), KPK (Kimberley-type pyroclastic kimberlite).

Kimberlite	**Drill hole (total depth)**	**Kimberlite Type**	**Number of samples (depth in meters)**
Leslie	LDC9 (258.17 m)	Coherent (ECK)	**6** (23.7, 60.0, 127.3, 162.0, 194.65, 234.6)
Boa	DDH (112 m)	Pyroclastic, Coherent (ECK)	**5** (52.0, 53.3, 66.2, 84.8)
BK1	BK1 #1 (61.98 m)	Coherent-A (ICK), KPK	**4** (36.7, 40.78, 50.41, 54.33)
BK1	BK1 #2 (142.71 m)	Coherent-A, KPK	**5** (8.64, 18.21, 32.42, 45.65, 124.41)
BK1	BK1 #3 (no depth log)	Coherent-B	**3** (no depth log)
AK15	AK15 (151.7 m)	Coherent	**3** (56.16, 98.48, 151.7)

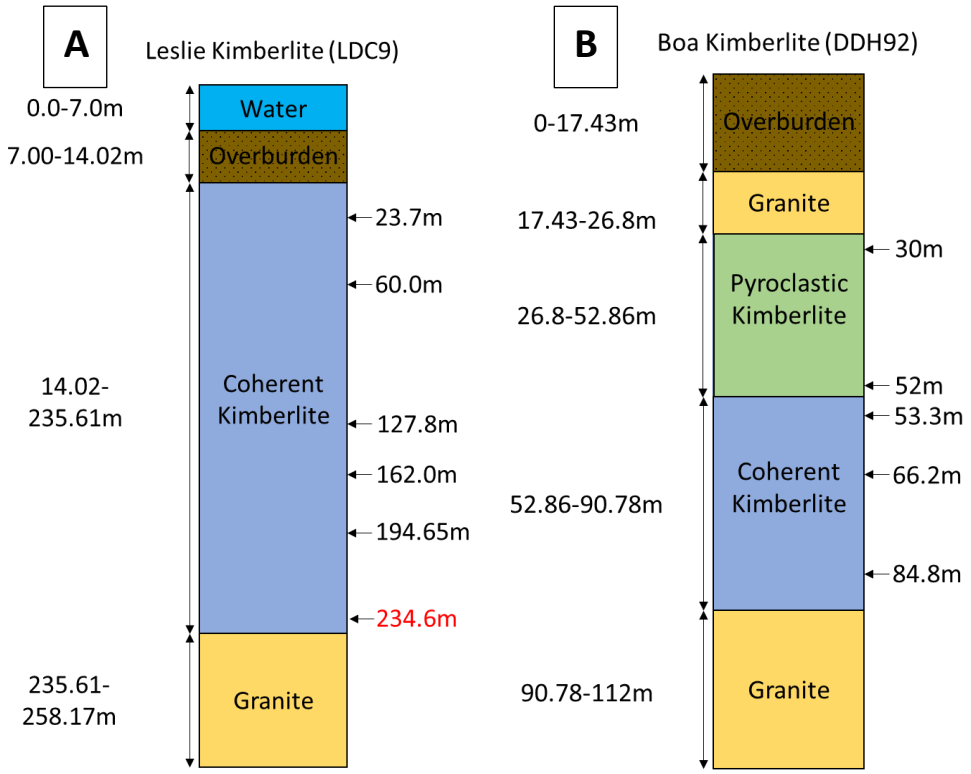

Figure 2.3: Borehole columns from Lac de Gras kimberlites. (A) Borehole column of the Leslie kimberlite showing the samples selected and their depth on the right (Note: red text indicates samples where apatite was not present). (B) Borehole column of the Boa kimberlite pipe showing the samples selected and their depth.

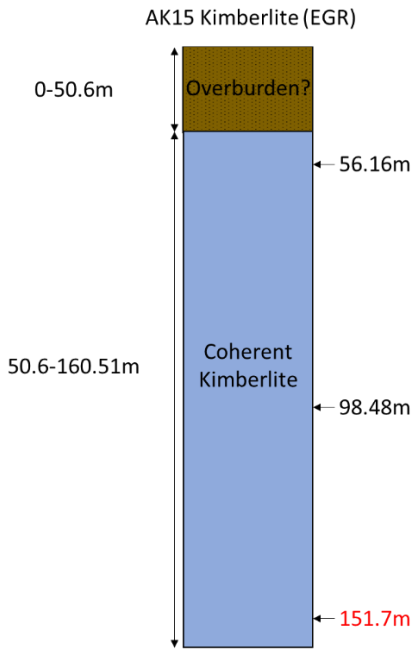

Figure 2.4: Borehole column of AK15 intrusion showing the samples selected and their depth. (Note: red text indicates samples where apatite was not present.)

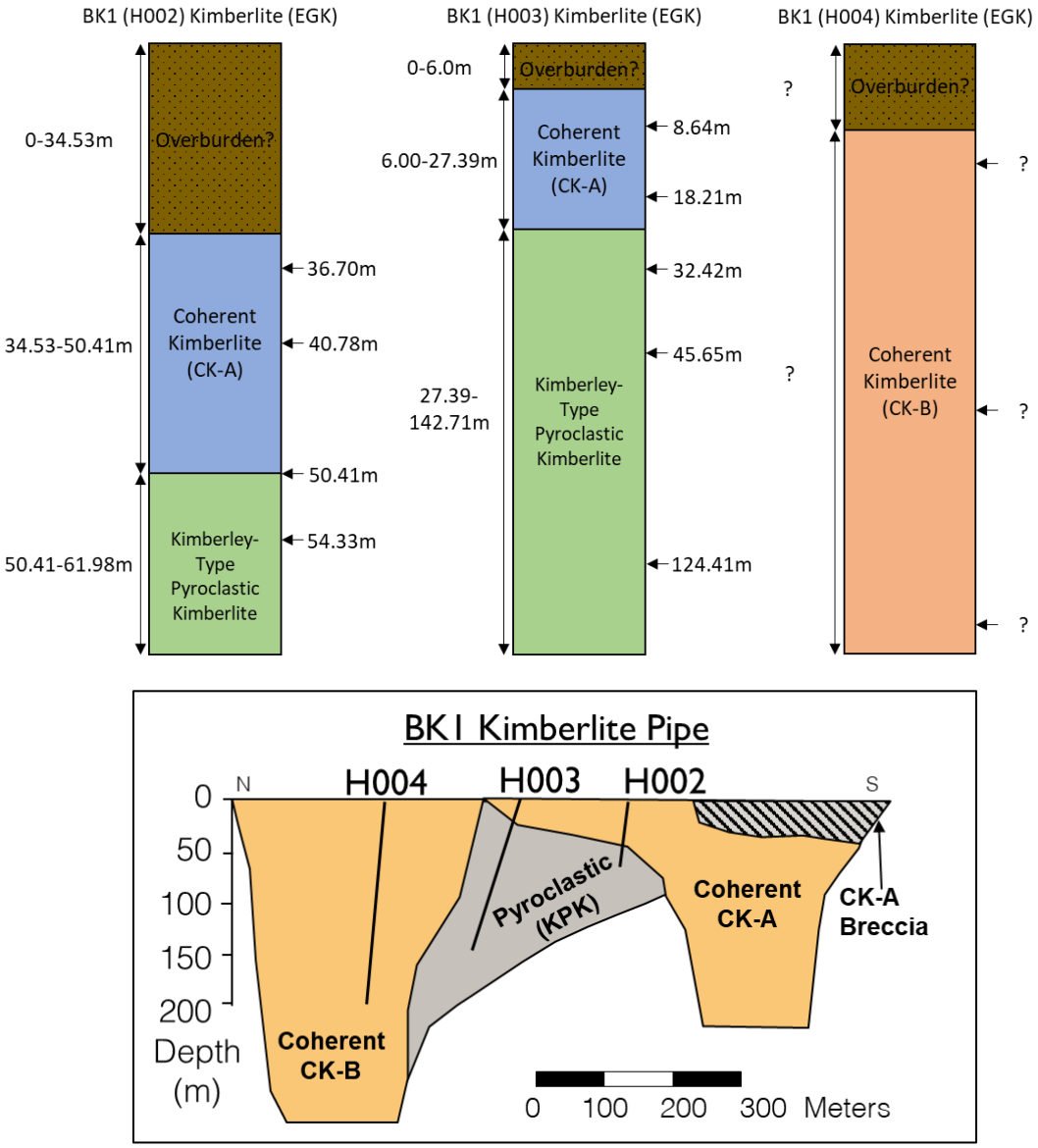

Figure 2.5: Lithologies of the three boreholes in the BK1 kimberlite pipe showing the depths where the samples were selected. Borehole H004 does not have any depth log available and only shows the inferred sample locations and its relative depth to each other. Cross section of the BK1 kimberlite pipe showing the locations of the boreholes and the kimberlite lithologies (after Fedortchouk et al., 2017).

2.2 Scanning Electron Microscope

Identification of apatite, its crystal shape and texture was studied at Saint Mary's University, Halifax, N.S., using a TESCAN MIRA 3 scanning electron microscope (SEM) equipped with an INCA X-Max 80mm^2 energy dispersive spectroscopy (EDS) system. Thin sections of kimberlites and experimental run products were coated with carbon prior to the analysis. In natural samples, apatite was found using backscatter electron (BSE) imaging and confirmed using EDS. For the samples with a low apatite abundance, x-ray mapping was used to locate apatite.

2.3 Electron Microprobe Analyses

Quantitative analysis of natural and experimental apatite and experimental glasses was performed at the Robert M. MacKay Electron Microprobe Lab at Dalhousie University, Halifax, N.S., using wavelength dispersive spectroscopy (WDS) on a JEOL 8200 EPMA with an accelerating voltage of 15 kV, 10 nA beam current, and 1 μm focused beam. Analyses of quenched melts utilized a spot size area of 10-75 μm. Information on the primary elemental standards and peak count times used for the analyses of apatite and glasses are provided in Table 2.2. Data reduction was performed using the ZAF model.

Table 2.2: List of elements analyzed using EMPA, and the standards used for apatite (left column) and glasses (right column).

Element Analyzed	Peak Count Time (s)	kV	Standard Used	Element Analyzed	Peak Count Time (s)	kV	Standard Used
Ca	20	15	Durango fluorapatite	Ca	20	15	BHVO basalt glass, Dolomite
P	20	15	Durango fluorapatite	P	20	15	Durango fluorapatite
Sr	20	15	Celestite	Si	20	15	Sanidine
Si	20	15	Sanidine	Al	20	15	Sanidine
Ba	20	15	Barite	K	20	15	Sanidine
K	20	15	Sanidine	Na	20	15	Sanidine
Na	40	15	Jadeite	Mg	20	15	BHVO basalt glass
Mn	20	15	Rhodonite	Fe	20	15	BHVO basalt glass
V	20	15	V-metal	S	20	15	BHVO basalt glass
Fe	20	15	Magnetite	Co	20	15	BHVO basalt glass
La	20	15	Monazite	Ni	20	15	BHVO basalt glass
Ce	20	15	Monazite	Cl	30	15	Tugtupite
Pr	20	15	REE glass	F	30	15	Fluorite
Nd	20	15	REE glass				
Cl	30	15	Tugtupite				
F	30	15	Fluorite				

2.4 LA-ICP-MS Analyses

Laser ablation inductively coupled plasma mass spectrometry (LA-ICP-MS) analyses were performed on an ESI NWR213 laser ablation system using a frequency quintupled Nd:YAG laser operating at 213 nm coupled to a Thermo Scientific iCAP quadrupole inductively coupled plasma mass spectrometer equipped with a single helium kinetic energy discrimination cell at the Dalhousie University Laser Ablation ICP-MS Laboratory. Tuning was done using NIST610 standard to maximize signal sensitivity while also minimizing oxide production rate to achieve the following: ^{115}In (60000-1000000 CPS), a $^{238}U/^{232}Th$ ratio of approximately 1, and a $^{248}Th/^{232}Th$ ratio of approximately 0.005. Laser

energy density was maintained at 5-10% operating power (5.2 J/cm^2) with 5-10 Hz repetition rate depending on the size of apatite crystals or quenched melt. Gas flow rate through the ablation cell was set at 0.9 L/min. Each analysis involves approximately 20 seconds of background collection with the laser off, followed by 60 seconds of sample ablation and then followed by 60 seconds of cell washout with the laser off. Helium is used as carrier gas flowing from the laser ablation cell to the mass spectrometer where it was mixed with argon at a T-junction with a homogenizer prior to entering the spectrometer. NIST610 synthetic glass was used as the primary external standard and was measured twice before and after every interval of 16 analyses. Durango apatite, BHVO1, and BIR1 basalts were also used as control standards and placed in intervals amongst the analyses. The precision and accuracy of the analyses are illustrated in Figure ES 1.

The spot sizes for apatite analyses were selected on a grain-to-grain basis, which ranged from 10-30 μm depending on the crystal size and presence of zoning. Quenched melt analyses spot sizes ranged from 10-90 μm depending on the area available and the size of the quench crystals. Where quenched melts are large, a line ablation pattern is used in conjunction with a large spot size (75-90 μm) to maximize signal sensitivity. The following isotopes were analyzed for apatite composition: ^{24}Mg, ^{27}Al, ^{29}Si, ^{49}Ti, ^{50}V, ^{75}As, ^{85}Rb, ^{88}Sr, ^{89}Y, ^{91}Zr, ^{93}Nb, ^{133}Cs, ^{139}La, ^{140}Ce, ^{141}Pr, ^{146}Nd, ^{147}Sm, ^{153}Eu, ^{157}Gd, ^{163}Dy, ^{172}Yb, ^{175}Lu, ^{178}Hf, ^{232}Th, and ^{238}U. The analyses used calcium as an internal standard, whose composition was previously obtained from EPMA on the same grains that have been ablated. Data reduction was done using the Iolite software package version 3.6.

Screening of apatite analyses was done by excluding analyses with anomalously high concentrations in ^{24}Mg, ^{27}Al, and ^{29}Si which suggests contamination with the melt

composition. Melt analyses were screened for anomalously low concentrations of ^{24}Mg, ^{27}Al, and ^{29}Si (with the exception of carbonate (CAA) runs) on the basis that the analyses were contaminated with the inclusion of apatite or other phases.

2.5 Experimental Methods

2.5.1 Starting Mixtures

The unknown nature of primary kimberlite melt compositions is in large part due to the high amount of external materials incorporated, alteration, and volatile loss during emplacement making it difficult to determine the original composition (Moussallam et al., 2016). Recent estimates of primary kimberlite composition suggested a melt with very low silica content (18-30 wt.% SiO_2) and high alkaline content (30-45 wt.% MgO + CaO) based on quenched kimberlite melts and geochemical melting models (Moussallam et al., 2016, and references therein). An experimental study of a CO_2 solubility model in kimberlite melts estimate that the CO_2 content ranges from ~30 wt. % CO_2 in melts with 12 wt. % SiO_2 to ~3 wt. % CO_2 in melts of 40 wt. % SiO_2 (Moussallam et al., 2015). The solubility of CO_2 depends on pressure and melt composition with a decrease in solubility with decreasing pressure and increase in SiO_2 content.

In the starting materials for the experiments, we used two approaches for synthetic analogues of an evolved kimberlite melt that reflect low SiO_2 content, high alkaline-earth content, and volatile-rich (Moussallam et al., 2016). First, we used three compositions TA-6, TA-9 and TA-16 from Moussallam et al., (2016) with SiO_2 ranging 16.59-23.13 wt. % and CO_2 ranging 9.20-33.49 wt. % (Table 2.3). Second, we used the bulk composition of a coherent Leslie kimberlite (Ekati Mine), from which we subtracted the composition of xenocrystal and phenocrystal olivine, and added CO_2 lost during the eruption (described

below). In addition, we examined partition coefficient for apatite in $CaCO_3$ melt due to a discrepancy between the previous estimates (Klemme and Dalpe, 2003; Hammouda, et al., 2010).

We used two types of apatite in experiments: 1) a finely ground natural Durango apatite with natural elevated concentrations of trace elements (La, Ce, Sm, Dy, Lu, Sr, Rb, Cs, Zr, Nb, U, Th) and 2) a powder of synthetic apatite free of trace elements. Most of the runs were doped with 4 wt. % of a mixture prepared from powders of the following trace element compounds: Nb, SrO, Rb_2CO_3, ZrO_2, $Sm_2(CO_3)_3$, Cs_2CO_3, Hf, La_2O_3, Yb_2O_3, and Eu_2O_3 providing the concentration for each compound of 0.4 wt.%.

Starting mixtures TA6, TA9, TA16 (Table 2.3) based on Moussallam et al. (2016) were modified by the replacement of FeO with CoO to prevent Fe loss into platinum capsules. The starting mixtures based on the whole-rock composition of Leslie kimberlite from Nowicki et. al (2004) were modified by subtracting stoichiometrically 50 vol% of olivine in order to closer approximate the composition of kimberlitic groundmass without olivine phenocrysts and xenocrysts. This was done because olivine phenocrysts and xenocrysts crystallized before the groundmass. A typical kimberlite contains 25% of its mode consisting of large (>1 mm) irregular or rounded olivine macrocrysts with another 25% of the mode made up by euhedral phenocrystal olivine (Scott Smith, 2008). Composition of both xenocrystal and phenocrystal olivine in kimberlite is approximately 90-92 mol.% forsterite (Mitchell, 1986). Therefore, the density of kimberlite and olivine was used to convert 50 vol% of olivine into 31.38 wt.% MgO and 23.40 wt.% SiO_2 of olivine components (LS6 in Table 2.3).We also added CO_2 to this composition to the total of 15 wt. % and 26 wt. % to account for volatile loss during the emplacement (Nowicki et al.,

2008) (LS15 and LS26 in Table 2.3). In order to explore a possible effect of assimilation of crustal rocks by kimberlite magma we modified LS15 mixture by adding 20% of a granodiorite composition, the country rock for kimberlites in the Slave Province (Cousens, 2000). Mixture LS6M corresponds to the composition of interstitial melt estimated with EPMA in the runs with LS6 composition.

All mixtures were prepared from reagent grade oxides and carbonates (Table 2.3) stored in a desiccation oven at 100°C for at least 24 hours to remove any moisture. The oxides and carbonates were weighed on an electronic balance, mixed in an agate mortar with 95% ethanol for 15 minutes to homogenize the mixture, dried under a heat lamp, and stored in vials. Calcium oxide (CaO), Na_2O and K_2O were added as $CaCO_3$, Na_2CO_3, K_2CO_3 and decarbonated by heating in a platinum crucible at 1000°C for 24 hours. The resultant decarbonated mixture was then melted by heating to 1400°C for 30 minutes in a Lindberg Blue M box furnace and quenched immediately in water into a glass. The glass was recovered from the platinum crucible and grounded with 95% ethanol in an agate mortar for a minimum of 30 minutes until it had the consistency of a fine powder. The powdered glass was dried under a heat lamp and weighed with an electronic balance. After that, CO_2 was added as carbonates ($CaCO_3$, $MgCO_3$, $CoCO_3$). This mixture was mixed for 15 minutes with 95% ethanol to achieve homogeneity and dried. 10-50 wt.% of powdered Durango or synthetic apatite and 4 wt.% of the trace element “cocktail” was added to the mixtures. The final mixture consisting of a starting mixture, apatite, and trace elements was homogenized in a mortar and stored in a desiccation oven. H_2O was added as deionized water with a micro-syringe before welding the capsules. In LS mixtures, an additional amount of water was added as brucite ($Mg(OH_2)$).

Table 2.3: Starting mixtures used in experiments (wt. %).

	CAA	TA6	TA16	TA9	LS6	LS6M	LS15	LS15G20	LS26
SiO_2		16.59	23.13	22.68	16.95	20.26	15.21	28.79	14.37
TiO_2		0.20	0.30	0.30					
Al_2O_3		3.90	5.41	5.29	3.54	2.20	3.17	5.62	3.00
CoO		0.90	1.50	1.20					
Fe_2O_3					22.23		20.76	15.67	17.15
MgO		6.88	8.30	9.49	17.77	14.08	19.92	12.56	18.83
CaO	56.03	35.45	30.22	48.35	23.15	44.17	15.94	16.24	15.72
Na_2O		0.30	0.40	0.40	0.25	0.42	0.23	0.25	0.22
K_2O		2.30	3.20	3.10	0.83	0.87	0.75	2.02	0.71
CO_2	43.97	33.49	27.54	9.20	7.33	18.00	16.91	13.22	29.70
H_2O					7.96		7.11	5.62	0.30
Total	100.00	100.00	100.00	100.00	100.00	100.00	100.00	100.00	100.00

2.5.2 Choice of experimental conditions (T, P, fO_2)

Most of the piston-cylinder runs were conducted for 24 hours at a temperature of 1250 °C and pressure of 1 GPa using the estimates of kimberlite eruption temperature at 1 GPa of 970–1140 ±50°C (Fedortchouk et. al, 2005) and <1200 °C (Sparks, 2013). We selected the conditions of 1150-1350°C at 1 and 2 GPa to ensure that favourable amounts of apatite and melt are produced. The basis for this is from the results observed in experiments performed by Klemme and Dalpe (2006) where no other phases except apatite and melt were produced. Our experiments investigate the effect of temperature, fluid, and fO_2 on the trace element $D_{apatite/melt}$. Temperature was tested in a range from 1150 °C to 1350 °C. The addition of 5 and 10 wt.% distilled water to the starting mixtures was performed to test for any effects that the presence of a fluid may have on the D_{REE}. These parameters were tested to provide additional information about their effect on the D_{REE} between apatite and kimberlite and carbonatite melts.

Attainment of equilibrium was tested by comparing trace element Ds from 24 hours and 48 hours runs and by conducting forward and reverse experiments. In forward experiments with trace element-rich Durango apatite and undoped mixtures, elements diffuse from apatite into the melt. In reverse experiments with synthetic apatite and doped mixtures, elements from the melt are incorporated into the growing apatite. Finally, in the doped runs with Durango apatite some REEs diffuse into apatite, and other REEs diffuse into the melt.

Estimates of the fO_2 during crystallization of chromite inclusions in olivine phenocrysts gave a range of NNO -2.8 to NNO -4.4 and during kimberlite groundmass crystallization using the Fe content of perovskite gave an fO_2 range from NNO -5 to NNO +6 (Bellis and Canil, 2007a,b). Therefore, we selected a range of fO_2 buffers that covers the fO_2 range over 9 log units (iron-wustite (IW), magnetite-hematite (MH), and nickel-nickel oxide (NNO)) due to the large variation observed in natural kimberlites.

2.5.3 Experimental Procedure

The mixtures were loaded into 3 mm outer diameter Pt or Au-Pd capsules and welded with either a triple junction crimped end, an "ash-can" design, or a combination of both. Pt capsules were only used in Fe free experiments, whereas Au-Pd capsules were used in experiments containing Fe with the exception of one run (PC-189). Capsules containing water were welded while wrapped in a Kimwipe soaked in ethanol. The weight of the capsule was measured immediately after welding and placed in a desiccation oven overnight. The capsule was weighed afterwards to ensure that no water is lost.

Five different fO_2 buffers were used in our runs. fO_2 corresponding to carbon -carbon oxide (CCO) buffer was achieved by loading starting mixture into a graphite capsule and inserted

into a Pt capsule in PC-209 and PC-216. PC-213 with fO_2 corresponding rhenium-rhenium oxide (RRO) buffer was prepared by adding rhenium and rhenium oxide (ReO_2) powder directly into the capsule. Runs PC-178 and PC-179 used Ni foil partially oxidized into NiO inserted inside the capsule to buffer the mixture at the fO_2 corresponding to nickel–nickel oxide (NNO) buffer. The preservation of Ni and NiO was checked using BSE imaging and confirmed with EDS. Three runs used a double-capsule technique (Arima and Kozai, 2008) with NNO, iron–wustite (IW), and hematite–magnetite (HM) buffers. Water was added in both the inner and outer capsule to ensure that H^+ was available to migrate through the walls of inner capsule both directions to equilibrate fO_2. Buffers were prepared by mixing equal by weight parts of powders of both components and adding ~20 μL of H_2O loaded into 5mm diameter outer Pt capsule, packed around the 3 mm Pt capsule with the experimental mixture, and welded using a Lampert Puk 3 micro welder. The presence of both buffer phases after each run was confirmed under the optical microscope, with EDS, and X-ray powder diffraction (Figure ES 2). Fluid phases were confirmed by the presence of gas bubbles in the run products (Figure ES3).

The capsules were loaded into MgO ceramic pressure media and together with graphite heater were placed into a NaCl cell with a Pyrex glass sleeve (Figure 2.6). All experiments were run in piston-cylinder apparatus in the Experimental Petrology lab at the Earth Sciences Department of Dalhousie University using ¾" assemblies for runs with multiple samples and with double capsules and using ½" assembly for single-capsule experiments. Experiments were run at 1 or 2 GPa and 1150-1350°C for durations of 24-48 hours. The run procedure begins by pressurizing the sample to approximately 500 PSI prior to the heating. The sample is initially heated to 600°C with the where it is held for 6 minutes and

the pressure was increased to 1 GPa. Two different heating procedures were used to achieve the final run temperature: 1) the temperature is directly increased to final run temperature at the rate 50°C/min and 2) the temperature is increased above the run temperature to 1350°C and slowly decreased to the run temperature with the rate 0.2°C/min. Each run is held at the final run temperature for 24 or 48 hours. At the end of each experimental run, the sample was quenched automatically by terminating the power to sample.

Pressure was measured by a digital gauge with a precision better than 5%. The temperatures were measured and controlled with a Eurotherm controller using W95Re5-W74Re26 thermocouple. Thermal gradients and the hot zone position in the assemblies were determined using a spinel thermometer at 1300°C based on the thickness of the spinel layer developed between the Al_2O_3 thermocouple sleeve and the MgO ceramic (Watson et al.,2002). The temperature variation along the length of the capsule within the hotspot of the assembly is ± 25°C (Figure 2.7).

The extracted sample was mounted in 1-inch diameter epoxy resin pucks and cured on a hot plate for a minimum of 4 hours. The sample puck is cut in half using a Buehler IsoMet low speed cutting machine. Samples are then sanded progressively with coarser to finer sandpaper (180, 240, 320, and 600 grit) and polished with 1.0 μm and 0.3 μm alumina powder. Samples are cleaned in water with an ultrasonic cleaner between each step of sanding and polishing.

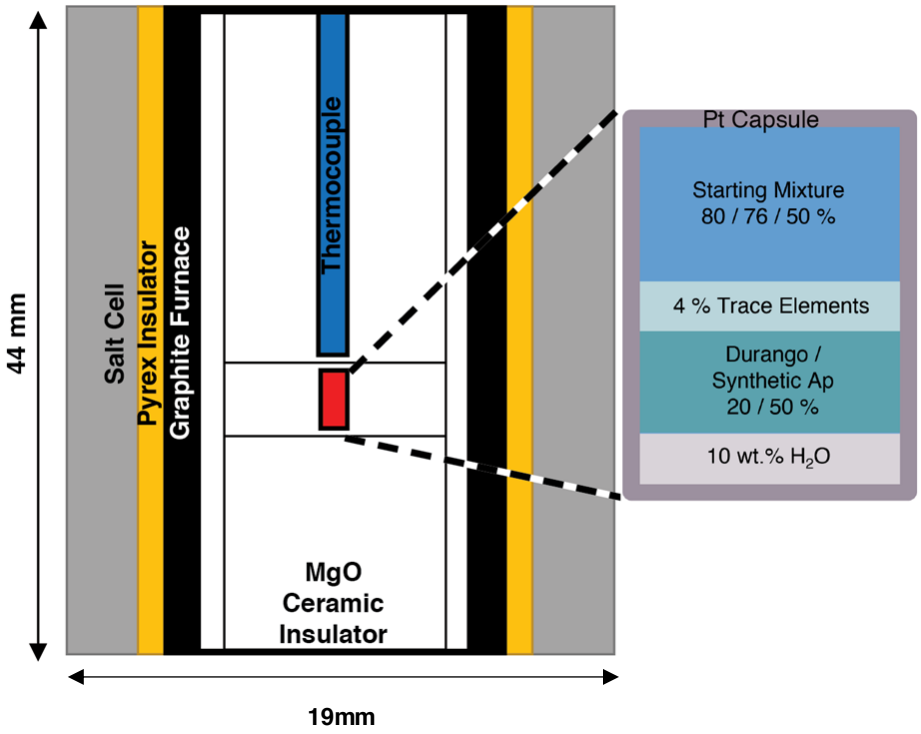

Figure 2.6: ¾" Piston-cylinder experimental assembly layout. Blue: thermocouple, red: platinum capsule, white: ceramic insulator, black: graphite heater, yellow: Pyrex insulator, grey: salt cell. Inset: Experiment capsule configuration show different ratios of starting mixture, apatite, trace elements, and water added inside a Pt-capsule.

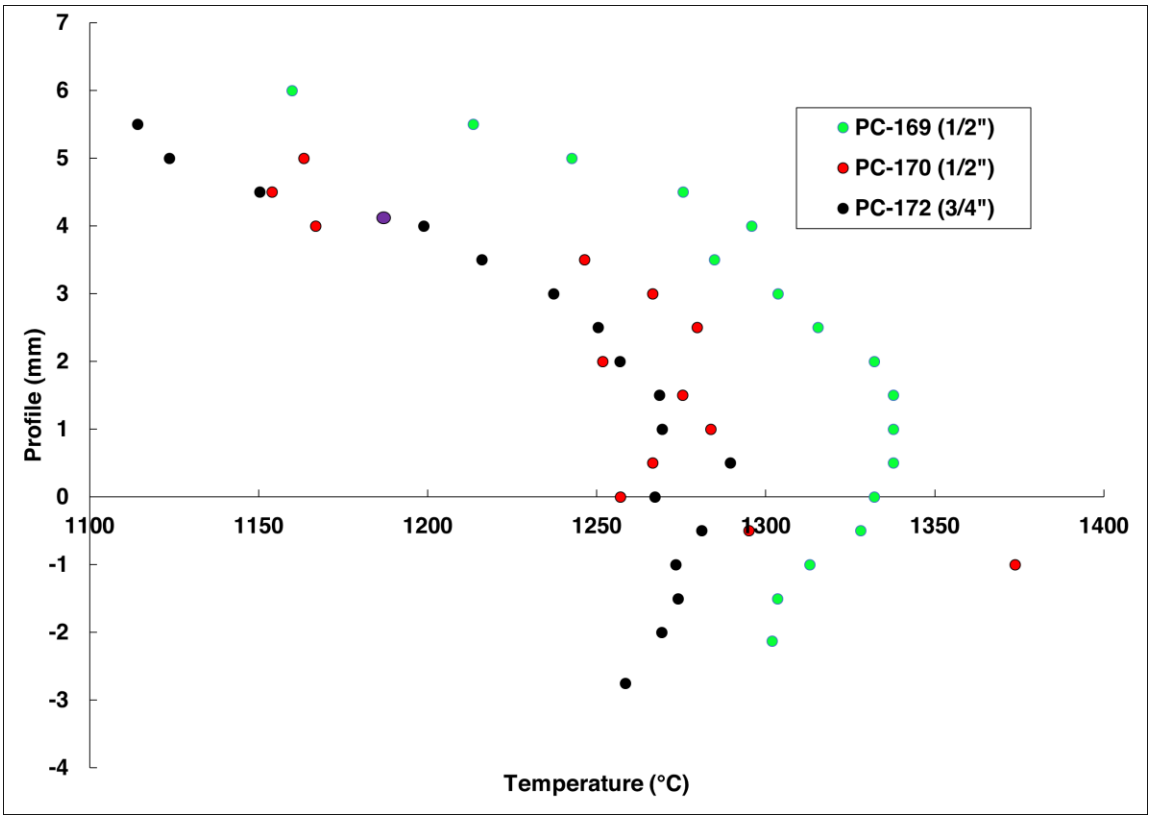

Figure 2.7: Spinel thermometer calibration profile of the pressure vessel performed at a target temperature of 1300°C. The 0 mm is the center point of the assembly.

Chapter 3: Results

3.1 Natural Apatite

The examined kimberlite samples show a notable variation in textures of apatite in groundmass. The textures range from irregular and radial aggregates composed of fine apatite crystals to discrete euhedral to subhedral crystals. Apatite commonly shows poikilitic texture as inclusions of olivine or monticellite within both clusters of radial aggregates of apatite needles and within discrete apatite crystals. The apatite textures and abundances are presented in the figures and accompanying descriptions below according to their sample depth. Apatite EMPA data is provided in Table 3.1.

Leslie Kimberlite

The six studied samples show apatite forming aggregated clusters in the top samples (23.7m), and euhedral prismatic crystals in the depth range 60-195m, and absent in the lowest sample (236.6m) close to the contact with the country rock. The abundance of apatite was highest at 127-162m, less abundant at 60m, and rare at 195m. At 23.7m, apatite occurs as large irregularly shaped aggregates (100-200 μm in diameter) composed of very fine apatite needles (<5 μm in size) (Figure 3.1 A). They are fairly abundant throughout the groundmass and have a poikilitic appearance. Backscatter electron images show fine bright spots of a rare earth element rich mineral commonly embedded in the apatite aggregates. The groundmass is mainly made up of serpentine with some patches of carbonate. At 60m, apatite occurs as fine euhedral grains embedded in the groundmass that are approximately 5-20 μm in size (Figure 3.1 B). The abundance of apatite is low to moderate. Monticellite is common throughout the groundmass. Carbonate segregations are

observed in the groundmass (Figure 3.7, A). At 127.3m, Apatite occurs as discrete euhedral crystals distributed throughout the groundmass (Figure 3.1 C) and forms elongated prisms or hexagonal grains. The elongated prisms are approximately 10-30 μm wide along the short edge. The hexagonal prisms are around 20-50 μm in diameter. Some crystals appear as aggregates of courser crystals as compared to the aggregates of LDC9 23.7. Some apatite crystals have observable poikilitic textures. Fresh monticellite is very abundant in the groundmass. Patches of carbonate segregations is also present with smaller crystals of apatite embedded in the carbonate. At 162.0m, apatite is uniformly distributed and occasionally occurring as clusters in the groundmass (Figure 3.1 D). Apatite is very abundant and is mostly euhedral showing both elongated and hexagonal grains. The thickness of elongated prismatic crystals measure approximately 10-20 μm across the short side. Discrete hexagonal crystals are approximately 5-50 μm in diameter. Fresh monticellite is also very abundant in the groundmass and carbonate is commonly found as well. Smaller discrete apatite crystal is also observed to be embedded in carbonates. At 194.65m, Apatite is very rare and occurs as small prismatic crystals and short elongated crystals in the groundmass (Figure 3.1 E). The prismatic crystals are approximately 3-5 μm in diameter, while the small elongated crystals are approximately 2 μm wide measuring along the short side. The groundmass is made up of mainly serpentine.

The composition of apatite in Leslie kimberlite differs between euhedral and acicular aggregated apatites. Acicular apatites show higher Sr and LREE and lower F content than the euhedral apatites (Figure 3.8, 3.9). The only significant correlation with depth is observed in Leslie kimberlite, where shallower samples tend to be higher in Sr and REE content and lower in F (Figure ES5 and ES6).

Boa Kimberlite

In the five examined samples, apatite is the most abundant in CK at 53.3-66.2m. The abundance is low at 52m in PK and in CK at 84.8m. Non-kimberlitic apatite approximately 20-50 μm in size and subhedral to anhedral in shape is commonly found at 30m embedded in the plagioclase from granite xenoliths (Figure 3.2 A). At 52m, apatite is found embedded in the serpentine-phlogopite groundmass and is relatively low in abundance compared to the deeper samples (Figure 3.2 B). Apatite is approximately 5-20 μm in size and is subhedral to euhedral in shape forming short prismatic crystals. This PK kimberlite appears to be more altered than the deeper samples. Apatite tends to be in close proximity to areas with carbonate. Apatite and carbonate also occur inside an assimilated xenolith (Figure 3.7, B). At 53.3m, the texture transitions to CK (Figure 3.2 C) and apatite is very abundant throughout the groundmass, where it occurs as large aggregate clusters of smaller prismatic elongated crystals approximately 30-100 μm in size commonly bearing inclusions of other minerals. Apatite is also observed as larger discrete euhedral crystals within calcite. within the aggregates of apatite. Groundmass contains monticellite, spinel, phlogopite, apatite, carbonate, and serpentine. At 66.2m, apatite is also very abundant throughout the groundmass (Figure 3.2 D). It also occurs as aggregates of smaller apatite crystals but with more distinct radial appearance. The clusters are approximately 100 μm in size. Unlike 53.3m depth, apatite does not occur as larger, discrete, euhedral crystals embedded in calcite. Inclusions are also common within the apatite aggregate clusters. At 84.8m, apatite shows moderate abundance and is embedded in the serpentine groundmass (Figure 3.2 E). Apatite crystals are approximately 10 μm in size and occur as elongated subhedral crystals or euhedral hexagonal prisms depending on their orientation. Inclusions are commonly

seen in the elongated crystals. Apatite tends to appear near or within calcite. Some elongated crystals appear to be broken up within calcite.

The non-kimberlitic apatite is distinguished by its low Sr and REE content (Milligan, 2017). The discrete and aggregated apatites found at the same sample depth (53.3m) show no significant difference in composition. Apatite composition in Boa kimberlite shows a slight difference between acicular and euhedral apatites. Acicular apatite tends to have slightly higher Sr and REE than the euhedral apatites (Figure 3.8). F content is the same for the two apatite textures (Figure 3.9). No significant correlation is observed in the apatite composition with relation to sample depth (Figure ES 6 and ES 7).

BK1 Kimberlite (H002)

Four samples from BK1 Kimberlite (H002) show distinctly different properties of apatite in accordance with their host facies. The shallower samples 36.7-40.78m from CK-A have higher abundance of apatite, which occurs as aggregates of fine crystals intergrown with mainly phlogopite in the serpentine groundmass (Figure 3.3 A B). Clusters of apatite have irregular shapes and are approximately 10-20μm in size. In addition to occurring throughout the groundmass, apatite is also commonly localized around olivine macrocrysts (Figure 3.7 D). The two deeper samples at 50.41-54.33m from KPK show low abundance and discrete apatite crystals emplaced in the groundmass. At 50.41m near the transition between CK-A and KPK, apatite occurs as euhedral prismatic crystals but some apatite crystals have “atoll” texture with a distinct core of silicate composition (olivine-serpentine based on the EDS spectrum) (Figure 3.3 C D E). Other crystals show a patchy appearance within a prismatic crystal. All observed crystals appear to have nonhomogeneous composition. The euhedral crystals are approximately 10-40μm in size. The abundance of

apatite is low in this sample. In the KPK sample at 54.33m, apatite occurs as both aggregates of small crystals in the groundmass as well as more discrete anhedral grains. The clusters are approximately 5-10 μm in size and the discrete grains are 5-15μm in size. Apatite is very low in abundance in this sample. No correlation can be concluded on apatite composition with relation to sample depth due to insufficient data.

BK1 Kimberlite (H003)

The five samples from BK1 Kimberlite (H003) contain two (8.64-18.28m) from CK-A and three (32.42-124.41m) from KPK. At 8.64m, subhedral apatite crystals are found intergrown with phlogopite in the groundmass and are approximately 10-20μm in size (Figure 3.4 A). The crystals have a mottled appearance possibly due to alteration. Apatite abundance is moderate. Similarly at 18.28m, microphenocrysts of apatite appears intergrown with phlogopite in the groundmass as irregularly shaped clusters within a serpentine groundmass (Figure 3.4 B). Apatite grain sizes range from approximately 10-20 μm in size and are prismatic in shape. The abundance of apatite is moderate. Apatite and phlogopite both exhibit poikilitic texture. At the 32.42m KPK transition, apatite appears as either very fine needle shaped clusters emplaced in the serpentine groundmass or as very fine clusters within magmaclasts or relict grains rimmed with diopside (Figure 3.7 C). The abundance of apatite is low. Apatite crystals are sized approximately 5-10μm. At 45.65m, apatite is very low in abundance. Apatite primarily occur in the core of what appears to be relict grains that has been altered and/or replaced (Figure 3.4 D). This is similar to EGK639 (32.42m) except with a lower abundance of diopside and larger sized apatite. Not all magmaclasts have apatite within the core. Apatite appears to occur as aggregates of small crystals, clumping together in clusters. At 124.41m, apatite forms

exclusively in the cores of relict grains that have been altered and/or replaced but with greater frequency and abundance (Figure 3.4 E). Grain sizes ranged from approximately 10-20 μm. However, the grains appear to be more of an aggregate of finer crystals clumped together. Perovskite is present in the groundmass and appears to be crystallizing before apatite. The composition of euhedral apatite in CK-A is significantly different from acicular apatite in KPK (Figure 3.8). The acicular apatites have significantly higher Sr but similar REE content. F is higher in the euhedral apatites from CK-A compared to the KPK acicular apatites (Figure 3.9). No significant correlation is observed in the apatite composition with relation to sample depth (Figure ES 6 and ES 7).

BK1 Kimberlite (H004)

Three samples from CK-B in BK1 kimberlite are from H004 drillhole. In the shallowest sample, apatite forms clusters of aggregates distributed in the groundmass and intergrown with phlogopite (Figure 3.5 A). The clusters are approximately 10-15 μm in size. Perovskite is moderately abundant and large in size (50-100 μm). In the sample from intermediate depth, apatite is very low in abundance and tends to occur as aggregates of small crystals intergrown around phlogopite in the groundmass (Figure 3.5 B). The clusters are around 5-10μm in size. One cluster exhibits a euhedral shaped edge. Perovskite is commonly present in this sample and appears to form earlier than apatite. In the deepest sample, apatite occurs as discrete, relatively euhedral prismatic crystals emplaced in the groundmass approximately 20-50μm in size (Figure 3.5 C). Zoning is apparent in some of the apatite crystals. They are generally intergrown with adjacent phlogopite in the groundmass. Apatite is moderately abundant, with carbonate, phlogopite and perovskite being commonly found throughout the groundmass. The composition of apatite is low in

Sr and LREE. No correlation can be concluded on apatite composition with relation to sample depth due to insufficient data.

AK15 Kimberlite

In the three samples in CK facies from AK15 kimberlite, apatite was very abundant in the shallowest sample (56.16m) forming discrete euhedral to subhedral crystals approximately 10µm in size as short elongated prisms (Figure 3.6 A). The abundance of apatite becomes scarcer with depth, it is rare at 98.48m and entirely absent at 151.7m. At 56.16m, apatite is found throughout the groundmass in very high abundance. Apatite occurs as discrete crystals approximately 10µm in size. Apatite crystals appear to be euhedral to subhedral in shape and frequently occur as short elongated prisms. Carbonate is present as a secondary mineral in the groundmass. Spinel is high in abundance and large in size and is commonly rimmed with titanite. The groundmass is mainly serpentine with large phenocrysts of phlogopite. At 98.48m, apatite is very low in abundance and very fine grained, approximately 5µm in size (Figure 3.6 B). It is found embedded in the groundmass intergrown with phlogopite/serpentine groundmass. The shape is similar to the apatite found at 56.16m. Only one specimen was observed in the sample. Apatite is very fine grained, approximately 5µm in size. Monticellite, spinel, and perovskite are commonly found throughout the groundmass. The composition of apatite is low in LREE and Sr. No correlation can be concluded on apatite composition with relation to sample depth due to insufficient data (Figure ES 6 and ES 7).

Table 3.1: Average composition of apatite from Leslie, Boa, BK1 and AK15 kimberlites sampled at different depths. Stoichiometry of apatite calculated based on (Ketcham, 2015). OH apfu calculated assuming 1 total anion in the halogen site. * DDH_53.3_A = aggregate apatites; DDH_53.3_E = discrete euhedral apatites.

Kimberlite	Leslie		Leslie		Leslie		Leslie	
Sample	LDC9_23.7		LDC9_60		LDC9_162		LDC9_127.8	
n	20	1σ	10	1σ	10	1σ	20	1σ
Na_2O	0.08	0.05	0.01	0.03	0.03	0.06	0.04	0.07
CaO	49.12	0.76	51.66	1.17	51.00	1.38	50.09	0.57
P_2O_5	36.87	1.04	38.59	0.72	38.12	1.40	37.22	0.84
FeO	0.14	0.09	0.44	0.20	0.43	0.55	0.20	0.09
SiO2	1.07	0.16	1.27	0.13	1.25	0.51	1.03	0.16
BaO	0.00	0.00	0.00	0.01	0.00	0.00	0.00	0.01
Ce_2O_3	1.65	0.23	1.05	0.17	1.37	0.31	1.41	0.22
La_2O_3	1.05	0.22	0.61	0.12	0.74	0.26	0.82	0.15
SrO	3.14	0.60	1.36	0.14	1.79	0.16	2.00	0.28
Pr_2O_3	0.45	0.08	0.48	0.05	0.49	0.12	0.48	0.10
V_2O_3	0.17	0.04	0.14	0.07	0.13	0.04	0.13	0.04
K_2O	0.05	0.02	0.04	0.01	0.11	0.08	0.05	0.03
Nd_2O_3	0.29	0.14	0.19	0.12	0.29	0.09	0.30	0.14
MnO	0.01	0.01	0.00	0.01	0.01	0.02	0.00	0.01
F	1.97	0.15	2.68	0.31	2.93	0.37	2.55	0.25
Cl	0.00	0.00	0.00	0.01	0.01	0.01	0.00	0.00
$-O=(F,Cl)_2$	0.99	0.08	1.34	0.16	1.47	0.19	1.27	0.12
Total	97.08	1.04	99.88	1.76	100.16	1.87	97.59	1.10
Structural formulae calculated on the basis of 8 cations:								
Na	0.010	0.009	0.000	0.004	0.000	0.011	0.010	0.013
Ca	4.760	0.040	4.840	0.029	4.810	0.050	4.830	0.022
P	2.820	0.051	2.860	0.027	2.840	0.067	2.840	0.043
Fe	0.010	0.007	0.030	0.015	0.030	0.041	0.020	0.007
Si	0.100	0.015	0.110	0.012	0.110	0.047	0.090	0.015
Ba	0.000	0.000	0.000	0.000	0.000	0.000	0.000	0.000
Ce	0.050	0.008	0.030	0.005	0.040	0.010	0.050	0.007
La	0.040	0.008	0.020	0.004	0.020	0.008	0.030	0.005
Sr	0.160	0.033	0.070	0.006	0.090	0.007	0.100	0.015
Pr	0.010	0.003	0.020	0.002	0.020	0.004	0.020	0.003
V	0.010	0.003	0.010	0.004	0.010	0.003	0.010	0.003
K	0.010	0.003	0.000	0.001	0.010	0.009	0.010	0.004
Nd	0.010	0.005	0.010	0.004	0.010	0.003	0.010	0.004
Mn	0.000	0.001	0.000	0.001	0.000	0.001	0.000	0.000
∑	8.000		8.000		8.000		8.000	
F	0.560	0.047	0.740	0.085	0.820	0.105	0.720	0.071
Cl	0.000	0.001	0.000	0.001	0.000	0.001	0.000	0.000
OH	0.430	0.047	0.260	0.085	0.180	0.105	0.280	0.071

Kimberlite	Leslie		Boa		Boa		Boa	
Sample	LDC 194.65		DDH GC		DDH 52		DDH 53.3 A*	
n	11	1σ	15	1σ	2	1σ	2	1σ
Na_2O	0.05	0.06	0.11	0.10	0.00	0.00	0.12	0.05
CaO	50.22	1.46	53.41	1.23	54.23	0.71	50.53	0.45
P_2O_5	37.03	0.77	40.67	1.11	40.17	0.30	36.22	0.02
FeO	0.55	0.10	0.04	0.02	0.21	0.03	0.14	0.04
SiO2	1.77	0.70	0.44	0.60	0.64	0.68	1.05	0.28
BaO	0.02	0.00	0.00	0.00	0.01	0.02	0.01	0.02
Ce_2O_3	1.27	0.36	0.26	0.10	0.15	0.09	0.90	0.04
La_2O_3	0.70	0.26	0.06	0.04	0.00	0.00	0.59	0.26
SrO	0.95	0.38	0.00	0.00	0.00	0.00	1.42	0.01
Pr_2O_3	0.40	0.10	0.39	0.07	0.41	0.05	0.40	0.04
V_2O_3	0.18	0.06	0.09	0.05	0.07	0.02	0.11	0.06
K_2O	0.10	0.07	0.04	0.04	0.13	0.06	0.05	0.01
Nd_2O_3	0.16	0.10	0.14	0.09	0.02	0.02	0.15	0.01
MnO	0.01	0.01	0.15	0.04	0.00	0.00	0.01	0.01
F	2.41	0.23	3.53	0.36	3.30	0.09	1.93	0.15
Cl	0.01	0.02	0.01	0.01	0.01	0.01	0.01	0.00
$-O=(F,Cl)_2$	1.21	0.12	1.77	0.18	1.65	0.04	0.97	0.07
Total	97.03	1.03	101.10	2.24	101.00	0.04	94.61	0.24
Structural formulae calculated on the basis of 8 cations:								
Na	0.010	0.011	0.020	0.018	0.000	0.000	0.020	0.008
Ca	4.820	0.086	4.930	0.046	4.980	0.054	4.930	0.028
P	2.810	0.066	2.970	0.040	2.910	0.015	2.790	0.007
Fe	0.040	0.007	0.000	0.002	0.020	0.003	0.010	0.003
Si	0.160	0.063	0.040	0.053	0.050	0.059	0.100	0.025
Ba	0.000	0.000	0.000	0.000	0.000	0.001	0.000	0.001
Ce	0.040	0.012	0.010	0.003	0.000	0.003	0.030	0.001
La	0.020	0.009	0.000	0.001	0.000	0.000	0.020	0.009
Sr	0.050	0.020	0.000	0.000	0.000	0.000	0.070	0.000
Pr	0.010	0.003	0.010	0.002	0.010	0.001	0.010	0.001
V	0.010	0.004	0.010	0.003	0.000	0.001	0.010	0.003
K	0.010	0.008	0.000	0.005	0.010	0.006	0.010	0.001
Nd	0.010	0.003	0.000	0.003	0.000	0.001	0.010	0.000
Mn	0.000	0.001	0.010	0.003	0.000	0.000	0.000	0.000
∑	8.000		8.000		8.000		8.000	
F	0.680	0.065	0.960	0.095	0.890	0.025	0.550	0.041
Cl	0.000	0.003	0.000	0.001	0.000	0.001	0.000	0.000
OH	0.320	0.068	0.040	0.095	0.110	0.025	0.440	0.041

Kimberlite	Boa		Boa		Boa		AK15	
Sample	DDH 53.3 E*		DDH 66.2		DDH 84.8		EGR665 (56.16)	
n	6	1σ	26	1σ	19	1σ	19	1σ
Na_2O	0.17	0.11	0.10	0.09	0.40	0.13	0.04	0.04
CaO	50.14	0.40	51.31	0.70	51.99	0.84	53.43	0.74
P_2O_5	36.41	0.55	37.42	0.99	37.01	0.53	38.01	1.04
FeO	0.12	0.07	0.19	0.10	0.35	0.11	0.37	0.06
SiO2	1.25	0.21	1.43	0.51	1.58	0.12	0.88	0.18
BaO	0.01	0.04	0.01	0.02	0.02	0.04	0.03	0.09
Ce_2O_3	0.83	0.15	1.11	0.24	0.79	0.15	0.50	0.13
La_2O_3	0.57	0.09	0.86	0.20	0.49	0.11	0.29	0.07
SrO	1.58	0.24	1.74	0.19	1.27	0.29	0.84	0.10
Pr_2O_3	0.39	0.05	0.42	0.09	0.40	0.10	0.37	0.09
V_2O_3	0.14	0.04	0.15	0.05	0.15	0.05	0.19	0.06
K_2O	0.06	0.02	0.04	0.02	0.10	0.02	0.03	0.01
Nd_2O_3	0.07	0.08	0.12	0.10	0.07	0.06	0.08	0.10
MnO	0.01	0.01	0.01	0.01	0.01	0.02	0.01	0.01
F	1.90	0.15	1.88	0.13	1.92	0.10	3.07	0.27
Cl	0.01	0.01	0.01	0.01	0.01	0.01	0.01	0.03
$-O=(F,Cl)_2$	0.95	0.07	0.94	0.06	0.96	0.05	1.54	0.13
Total	94.61	0.83	97.72	1.23	97.53	0.93	99.68	1.20
Structural formulae calculated on the basis of 8 cations:								
Na	0.030	0.019	0.020	0.015	0.070	0.021	0.010	0.006
Ca	4.880	0.031	4.860	0.037	4.880	0.033	4.990	0.047
P	2.800	0.027	2.800	0.052	2.750	0.028	2.800	0.060
Fe	0.010	0.005	0.010	0.007	0.030	0.008	0.030	0.005
Si	0.110	0.018	0.130	0.046	0.140	0.011	0.080	0.016
Ba	0.000	0.001	0.000	0.001	0.000	0.001	0.000	0.003
Ce	0.030	0.005	0.040	0.008	0.030	0.005	0.020	0.004
La	0.020	0.003	0.030	0.006	0.020	0.004	0.010	0.002
Sr	0.080	0.012	0.090	0.010	0.060	0.015	0.040	0.005
Pr	0.010	0.002	0.010	0.003	0.010	0.003	0.010	0.003
V	0.010	0.003	0.010	0.003	0.010	0.003	0.010	0.003
K	0.010	0.002	0.000	0.002	0.010	0.003	0.000	0.001
Nd	0.000	0.003	0.000	0.003	0.000	0.002	0.000	0.003
Mn	0.000	0.001	0.000	0.001	0.000	0.001	0.000	0.001
∑	8.000		8.000		8.000		8.000	
F	0.550	0.040	0.530	0.037	0.530	0.031	0.850	0.072
Cl	0.000	0.001	0.000	0.001	0.000	0.001	0.000	0.005
OH	0.450	0.040	0.470	0.037	0.470	0.031	0.150	0.072

Kimberlite	BK1 (H004)		BK1 (H003)		BK1 (H003)		BK1 (H003)	
Sample	EGK619		EGK636 (8.64)		EGK637 (18.28)		EGK639 (32.42)	
n	19	1σ	10	1σ	6	1σ	1	1σ
Na_2O	1.71	0.07	0.71	0.18	0.53	0.13	1.16	-
CaO	51.40	0.34	51.93	0.62	50.07	0.87	46.83	-
P_2O_5	30.15	0.34	35.92	1.01	34.73	0.29	30.68	-
FeO	0.90	0.04	0.26	0.08	1.63	0.04	2.45	-
SiO2	2.70	0.23	0.54	0.04	1.25	0.10	3.36	-
BaO	0.05	0.08	0.09	0.05	0.06	0.06	0.33	-
Ce_2O_3	0.12	0.11	0.15	0.08	0.17	0.10	0.22	-
La_2O_3	0.01	0.00	0.01	0.01	0.02	0.02	0.12	-
SrO	0.14	0.00	2.72	0.28	1.58	0.27	0.59	-
Pr_2O_3	0.32	0.18	0.36	0.09	0.34	0.08	0.33	-
V_2O_3	0.17	0.05	0.90	0.20	0.64	0.11	0.06	-
K_2O	0.17	0.03	0.10	0.03	0.10	0.04	0.28	-
Nd_2O_3	0.03	0.08	0.01	0.02	0.01	0.00	0.06	-
MnO	0.03	0.03	0.01	0.01	0.01	0.01	0.03	-
F	1.99	0.23	3.43	0.26	3.50	0.14	3.29	-
Cl	0.01	0.00	0.01	0.01	0.01	0.01	0.01	-
$-O=(F,Cl)_2$	1.00	0.11	1.72	0.13	1.75	0.07	1.65	-
Total	90.88	0.37	98.87	1.07	96.40	1.10	91.45	-
Structural formulae calculated on the basis of 8 cations:								
Na	0.300	0.010	0.120	0.031	0.090	0.023	0.210	-
Ca	5.010	0.002	4.910	0.033	4.850	0.042	4.720	-
P	2.320	0.009	2.680	0.056	2.660	0.019	2.440	-
Fe	0.070	0.003	0.020	0.006	0.130	0.003	0.200	-
Si	0.250	0.021	0.050	0.003	0.110	0.009	0.320	-
Ba	-	0.003	-	0.002	-	0.002	0.010	-
Ce	-	0.004	-	0.003	0.010	0.003	0.010	-
La	-	-	-	0.000	-	0.001	-	-
Sr	0.010	-	0.140	0.015	0.080	0.013	0.030	-
Pr	0.010	0.006	0.010	0.003	0.010	0.003	0.010	-
V	0.010	0.003	0.050	0.012	0.040	0.006	-	-
K	0.020	0.004	0.010	0.004	0.010	0.004	0.030	-
Nd	-	0.002	-	0.001	-	0.000	-	-
Mn	-	0.002	-	0.001	-	0.001	-	-
∑	8.000		8.000		8.000		8.000	-
F	0.570	0.067	0.960	0.080	1.010	0.046	0.980	-
Cl	-	-	-	0.002	-	0.001	-	-
OH	0.430	0.067	0.040	0.064	0.011	0.030	0.020	-

Kimberlite	BK1 (H003)		BK1 (H003)	
Sample	EGK641 (45.65)		EGK648 (124.41)	
n	8	1σ	4	1σ
Na_2O	1.41	0.14	0.84	0.02
CaO	40.70	3.50	47.62	0.37
P_2O_5	33.20	1.51	34.40	0.57
FeO	0.32	0.09	0.55	0.07
SiO2	1.08	1.12	2.51	0.29
BaO	1.62	0.25	1.50	0.50
Ce_2O_3	0.24	0.09	0.30	0.09
La_2O_3	0.19	0.12	0.06	0.08
SrO	10.53	3.41	1.20	0.19
Pr_2O_3	0.43	0.15	0.40	0.02
V_2O_3	0.09	0.04	0.06	0.03
K_2O	0.07	0.01	0.04	0.02
Nd_2O_3	0.15	0.06	0.05	0.07
MnO	0.01	0.01	0.03	0.02
F	2.54	0.16	2.05	0.10
Cl	0.01	0.01	0.03	0.02
$-O=(F,Cl)_2$	1.27	0.08	1.03	0.05
Total	93.86	0.86	92.64	0.51
Structural formulae calculated on the basis of 8 cations:				
Na	0.260	0.028	0.150	0.002
Ca	4.190	0.261	4.720	0.037
P	2.710	0.107	2.690	0.043
Fe	0.030	0.007	0.040	0.006
Si	0.100	0.106	0.240	0.026
Ba	0.060	0.010	0.050	0.018
Ce	0.010	0.003	0.010	0.003
La	0.010	0.004	0.000	0.003
Sr	0.590	0.199	0.060	0.010
Pr	0.020	0.005	0.010	0.001
V	0.010	0.003	0.000	0.002
K	0.010	0.001	0.000	0.002
Nd	0.010	0.002	0.000	0.002
Mn	0.000	0.001	0.000	0.002
∑	8.000		8.000	
F	0.780	0.055	0.600	0.028
Cl	0.000	0.002	0.000	0.003
OH	0.220	0.054	0.400	0.030

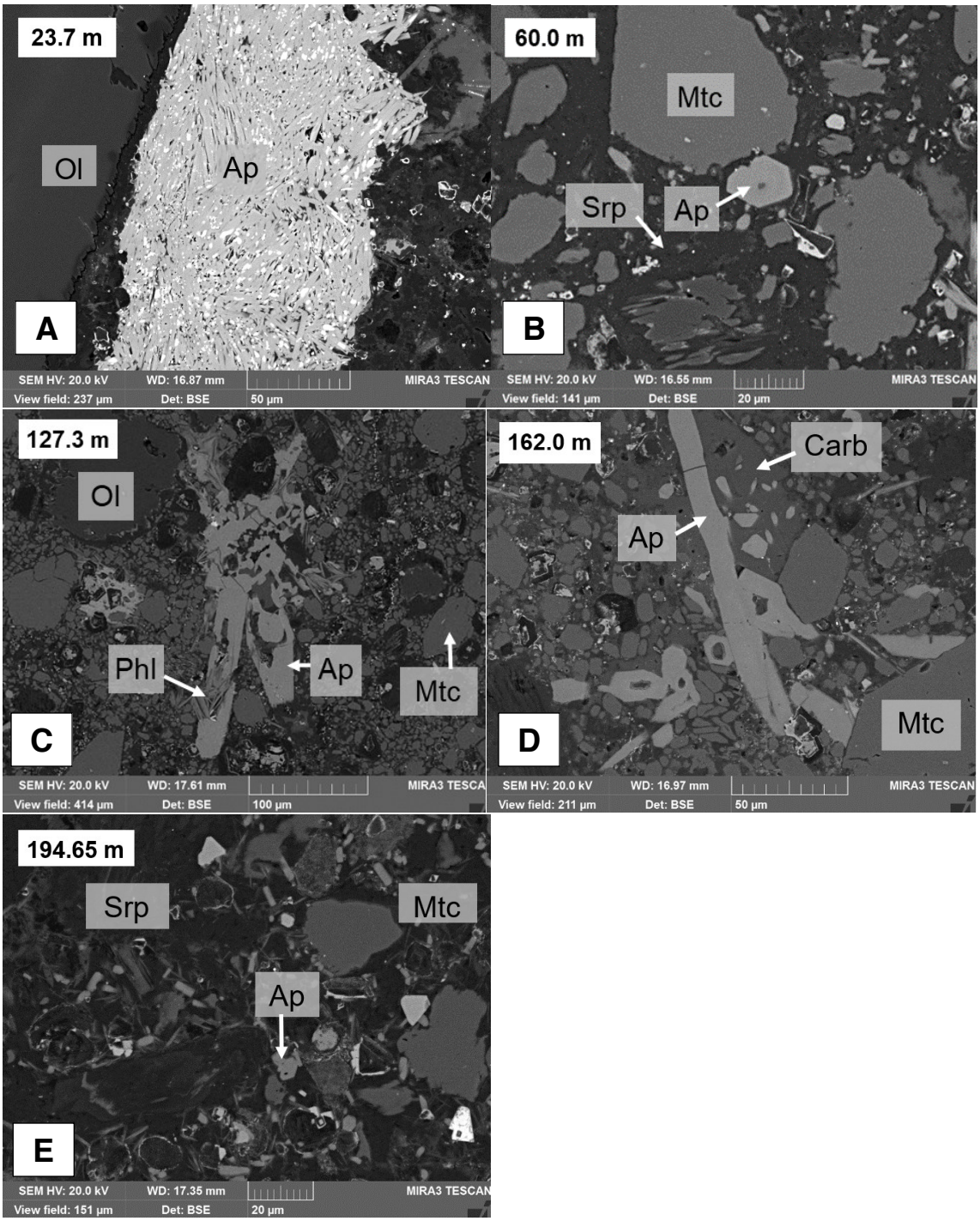

Figure 3.1: BSE images of apatite textures found at different depth intervals of Leslie kimberlite. Ol = olivine, Ap = apatite, Srp = serpentine, Mtc = monticellite, Carb = carbonate / calcite.

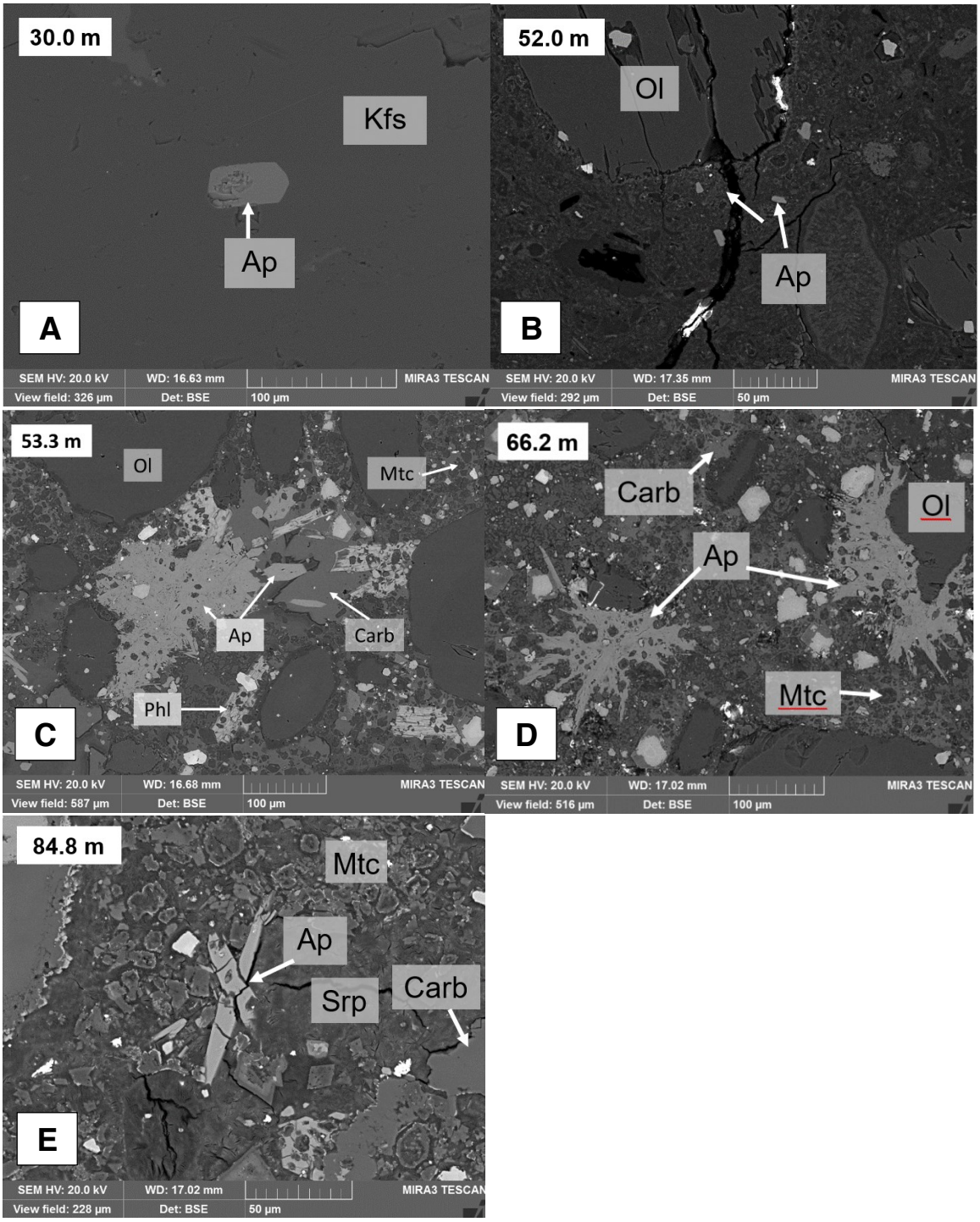

Figure 3.2: BSE images of apatite textures found at different depth intervals of Boa kimberlite. Kfs = K-feldspar

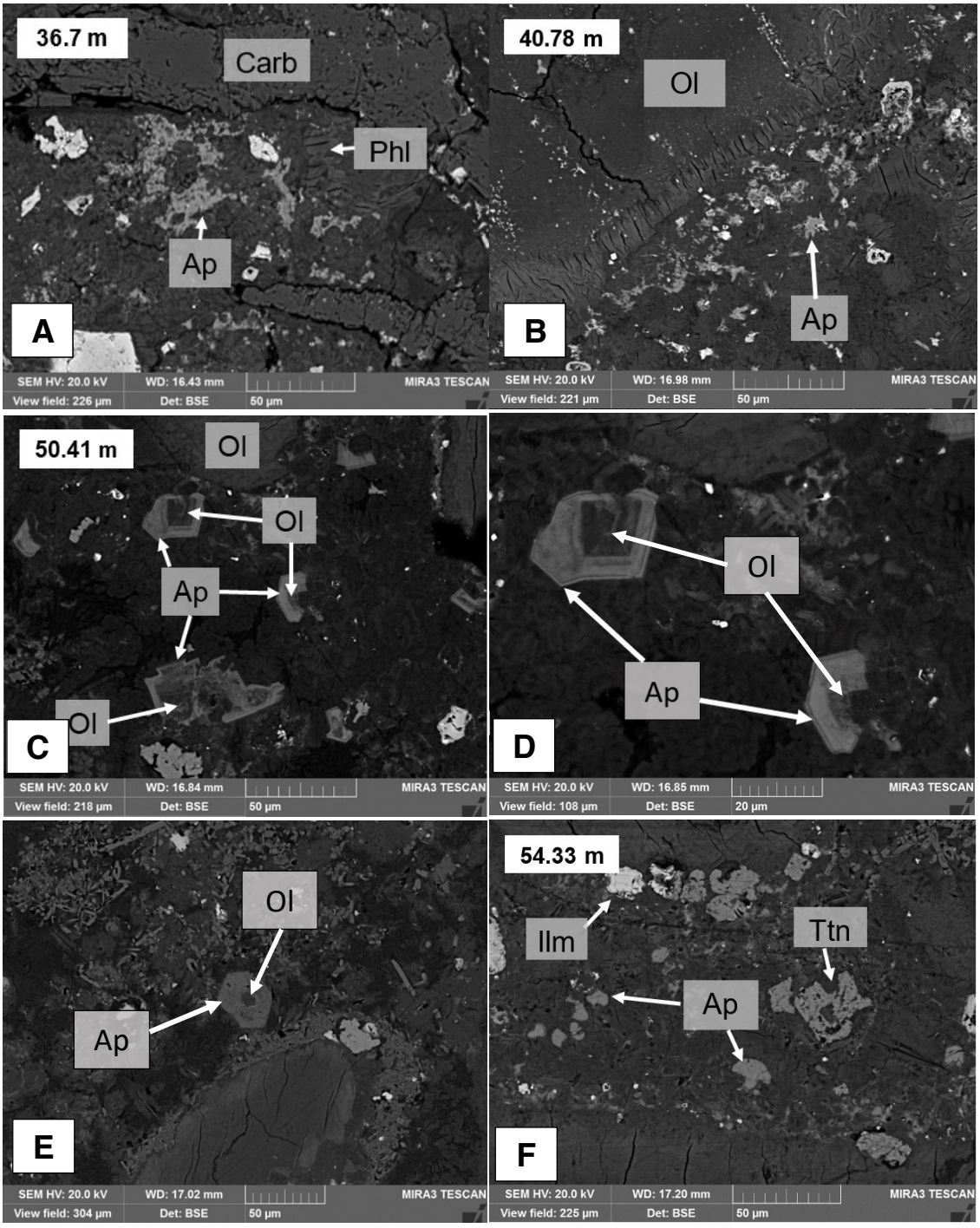

Figure 3.3: BSE images of apatite textures found at different depth intervals of BK1 (H002) kimberlite. Phl = phlogopite, Ilm = ilmenite, Ttn = titanite.

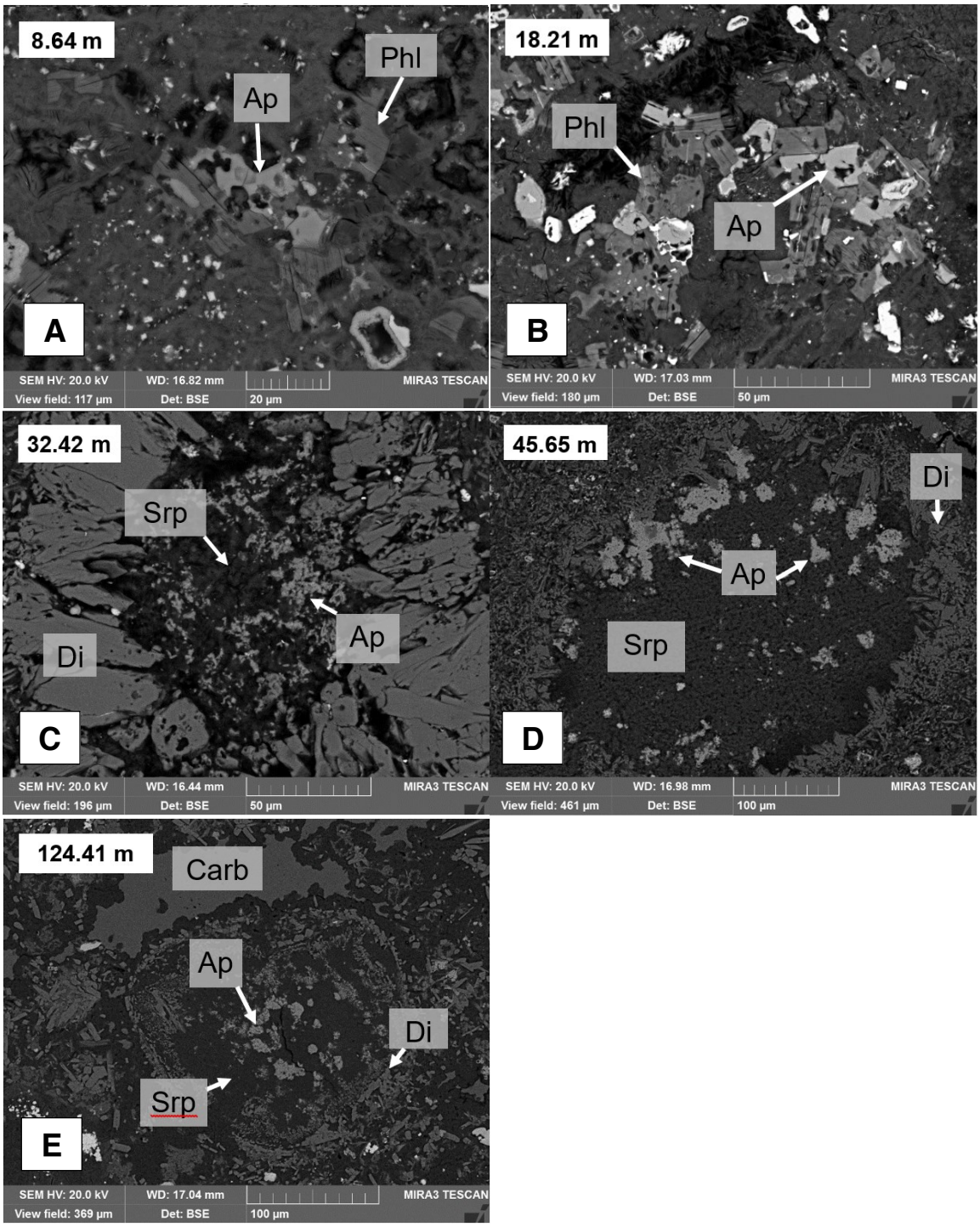

Figure 3.4: BSE images of apatite textures found at different depth intervals of BK1 (H003) kimberlite. Di = diopside.

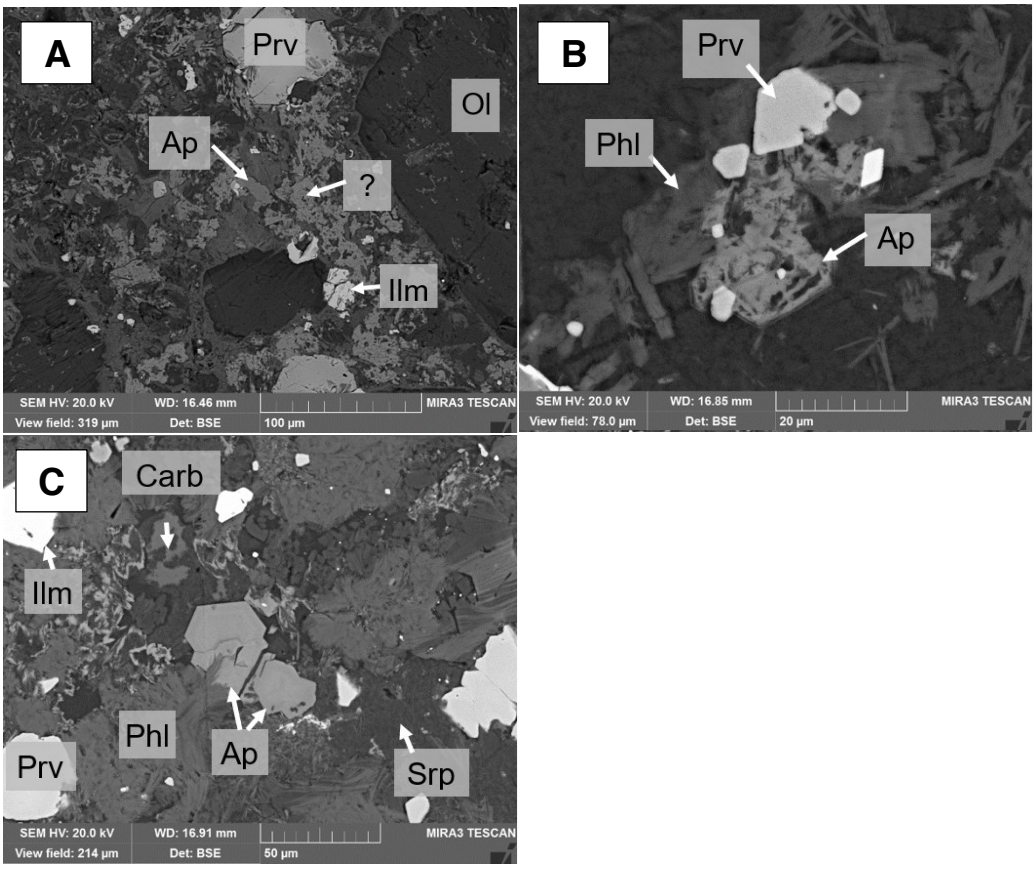

Figure 3.5: BSE images of apatite textures found at different depth intervals of BK1 (H004) kimberlite. Prv = perovskite.

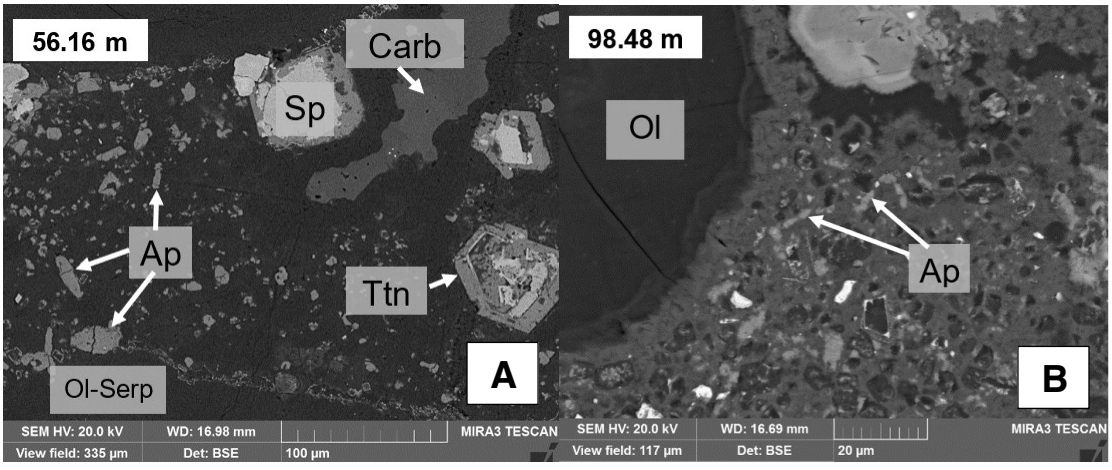

Figure 3.6: BSE images of apatite textures found at different depth intervals of AK15 kimberlite.

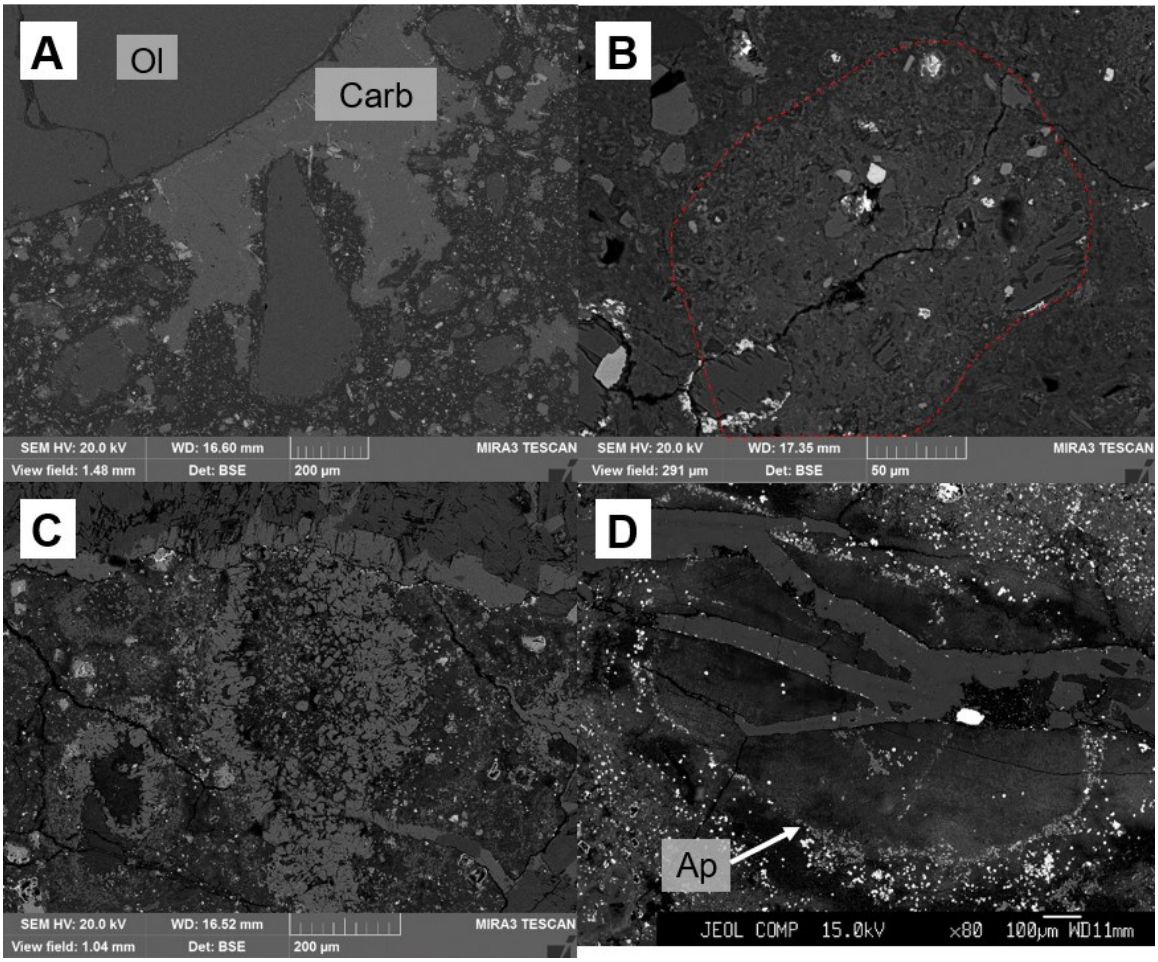

Figure 3.7: BSE images of kimberlite textures. **A**: carbonate segregations in the groundmass in Leslie (sample LDC9_60 (60 m)), **B**: assimilated xenolith (outlined in red) in Boa (sample DDH52 (52 m)), **C**: magmaclasts rimmed with diopside in BK1 H003 (sample EGK639 at 32.42 m), **D**: apatite localized around an olivine megacryst in BK1 H002 (sample EGK569 (40.78 m)).

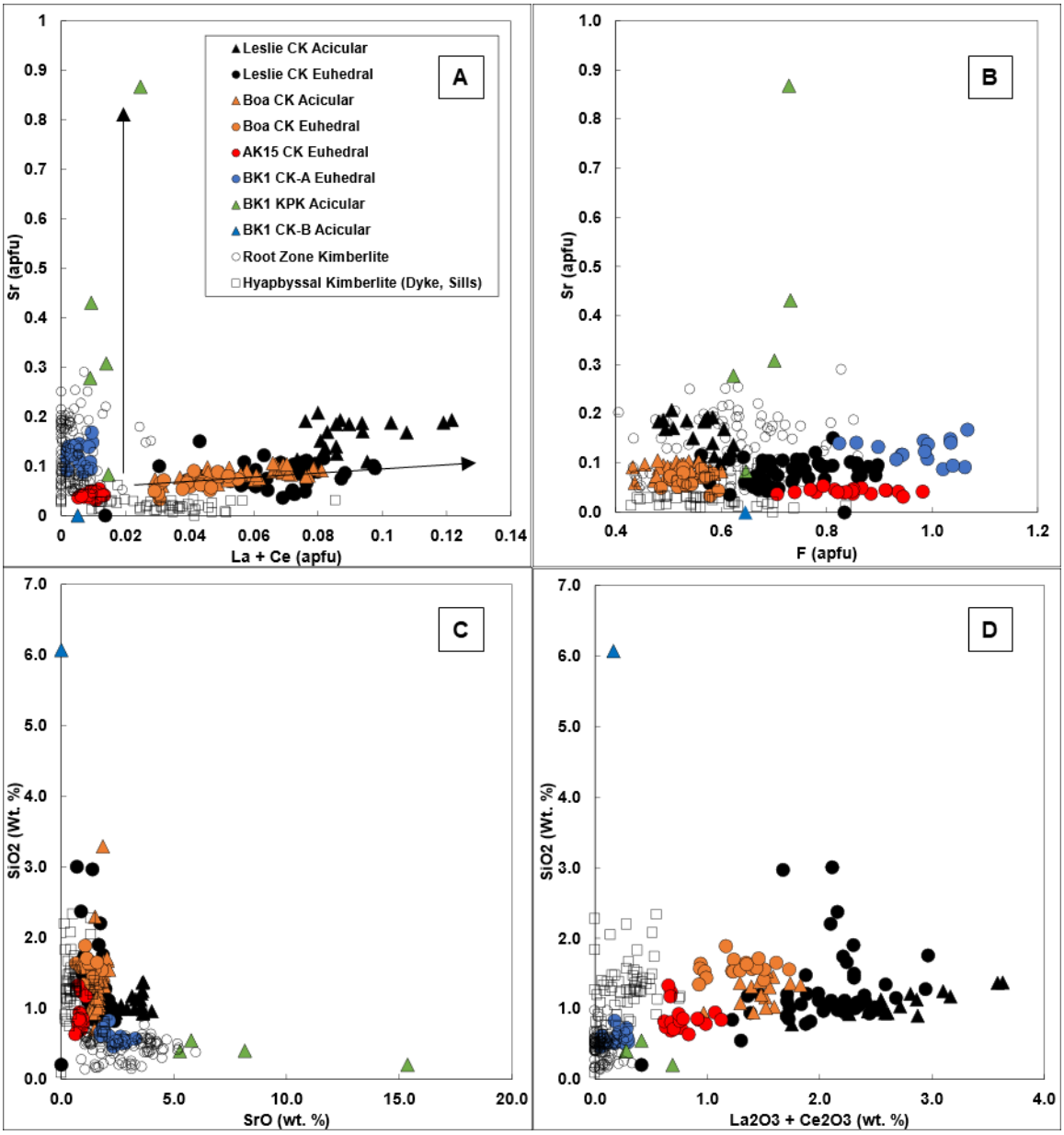

Figure 3.8: A) La + Ce vs. Sr content of apatite for different kimberlite pipe drill holes. The upward Sr trend is indicative of crystallization from a fluid. Whereas the trend moving right with increasing La + Ce suggests a magmatic origin. B) F vs. Sr content of apatite for different kimberlite pipe drill holes. C) SrO vs. SiO_2 content of apatite D) La_2O_3 vs. SiO_2. Hypabyssal and root zone kimberlites from Kimberley Cluster (South Africa) are shown for comparison (Soltys et al., 2020).

3.2 Experimental Results

3.2.1 Run products and composition of quenched melts

The results of the experiments and the summary of the run products are reported in Table 3.2 and Figure ES 3. All run products contain crystals of euhedral apatite ranging 5-50μm in diameter and various amount of quenched melt (Figure 3.10). Apatite typically concentrates along the bottom of the capsule and quenched melt is found along the capsule's sides and the top (Figure ES 3). Runs with overheating step (1350°C → 1250°C) developed large melt pockets (10-25 μm) between the apatite grains (Figure 3.10 B). Some compositions had other liquidus minerals in addition to apatite. H_2O-free runs with doped TA6 composition formed small amounts of REE-rich mineral closely resembling feldspar from its EDS spectrum. TA6 composition at 2 GPa (run PC-198) produced melt with very low SiO_2 (4 wt.%) due to significant diopside crystallization. Starting compositions based on Leslie kimberlite (LS6, LS15, and LS26) produced liquidus forsterite, diopside, spinel, and carbonate (Figure 3.10 D, E, F).

Products of H_2O-bearing runs show the presence of bubbles confirming retention of volatiles in the runs (Figure ES 3 PC-201, 207, 222). However, these textures are not conclusive to determine if volatiles reached the saturation at run conditions and exsolved H_2O-CO_2 fluid or if bubbles formed during quench. However, solubility experiments in with TA6 and TA9 melts (Moussallam et al., 2016) show volatiles are likely below saturation at our experimental conditions. Bubbles are also present in some H_2O-free runs (PC-179, PC-184, PC-185, PC-186, PC-224, 228) with CO_2.

Melt in all runs showed quenched textures with skeletal crystals of apatite, carbonate or silicate phases. To obtain representative melt compositions we used 10-75 μm spot size

area analyzes depending on the size of the quenched crystals (Figure 3.10 A-D). Runs with mixtures LS15 and LS26 formed very small glass pockets (>5 μm), which were not suitable for EMP and LA-ICPMS analyzes.

The study produced a large compositional range of the quenched melts equilibrated with apatite (Table 3.3 and Table 3.4, Figure 3.12) with SiO_2 ranging from 0-23 wt.%, CaO from 32-51 wt.%, MgO from 0-13 wt.%, CO_2 (calculated as a difference between the total of EMP analyzes and 100%) from 18-40 wt.%, and P_2O_5 from 1.5-14.5 wt.%. This range allows examining the effect of composition on element partitioning in apatite for the compositions close to that of an evolved kimberlite melt. TA9 composition in PC-224 run has an unusually low SiO_2 melt content (10.93 wt. %) compared to other TA6 and TA9 derived melts. This is attributed to the abundant crystallization of a diopside phase that is not present in other runs.

The effect of fO_2 was examined in three runs buffered at NNO, MH, and IW buffers giving log fO_2 range of 9 log units. Use of graphite capsule in PC-209 and PC-216 to buffer fO_2 at CCO did not yield useable run products due to the lack of any sizeable apatites and quenched melt pockets that could be successfully analyzed. PC-213 run with RRO buffer did not produce large enough melt pockets to be useable.

Table 3.2: Experimental conditions and results. All percentages are in wt. %. DA = Durango apatite, SA = synthetic apatite. TRC = Trace elements, Ap = apatite, Ap_r = apatite rims Lc = quenched melt with carbonates, Ls = quenched melt with silicates, Lsc = quenched melt with silicates and carbonates, Fl = fluid, Fo = forsterite, Di = diopside, Sp = spinel, Mont = monticellite, Per = periclase, Kfs = K-feldspar, CCO = carbon dioxide-carbon oxide, RRO = rhenium-rhenium oxide. All experiments are run at 1 GPa except for PC-198.

Run #	Composition	T (°C)	Buffer	Duration (hours)	Phases Present
PC-178	CAA (50%) + DA (50%)	1250	NNO[1]	24	Ap + Lc
	TA9 (50%) + DA (50%)	1250	NNO[1]	24	Ap + Lsc + Fl
PC-179	TA6 (48%) + DA (48%) + TRC (4%)	1250	NNO[1]	24	Ap + Lc / Ls + Fl + Kfs
	TA9 (48%) + DA (48%) + TRC (4%)	1250	NNO[1]	24	Ap + Lc / Ls + Fl
PC-184	LS6	1150		1	Mont + Sp + Peri + Lc
	LS15	1150		1	Fo + Di + Sp + Lc + Ls + Fl
	LS15G20	1150		1	Fo + Di + Sp + Lc + Fl
PC-185	LS6	1250		1	Fo + Mont + Sp + Per + Lc
	LS15	1250		1	Fo + Sp + Lc + Fl
	LS15G20	1250		1	Fo + Mont + Sp + Di + Lc + Fl
PC-186	LS6 (80%) + DA (20%)	1150		24	Fo + Sp + Ap + Lsc + Fl
	LS15 (80%) + DA (20%)	1150		24	Fo + Di + Sp + Ap + Lc + Fl
	LS26 (80%) + DA (20%)	1150		24	Fo + Di + Sp + Ap + Lc + Fl
PC-187	LS6 (80%) + DA (20%) + TRC (4%)	1150		24	Mont + Sp + Ap + Ap_r
	LS15 (80%) + DA (20%) + TRC (4%)	1150		24	Fo+Di + Sp + Ap + Ap new + Lc

Run #	Composition	T (°C)	Buffer	Duration (hours)	Phases Present
PC-188	LS6 (80%) + DA (20%) + TRC (4%)	1150		48	Mont + Fo + Sp + Ap + Ap_r
	LS15 (80%) + DA (20%) + TRC (4%)	1150		48	Fo + CPx + Sp + Ap + Lc
PC-189	LS6 (80%) + DA (20%) + TRC (4%) + 5% H2O	1150		24	Fo + Mont + Sp + Ap_r + Lsc + Fl
	TA9 (80%) + DA (20%) + TRC (4%) + 5% H2O	1150		24	Di + Ap + + Ap_r + Lc + Fl
PC-195	LS6M (88%) + DA (10%) + TRC (2%)	1250		24	Ap + Fo + Mont + Lsc + REE-phase
PC-196	TA6 (66%) + DA (10%) + SA (20%) + TRC (4%)	1300-1250		28	Ap + melt + REE-phase
PC-197	TA16 (76%) + SA (20%) + TRC (4%)	1300-1250		28	Ap + Lc + Per + Mont + REE-phase
	TA6 (76%) + SA (20%) + TRC (4%) + 10% H2O	1300-1250		28	Quench Ap + Melt
	CAA (76%) + SA (20%) + TRC (4%)	1300-1250		28	Ap + Lc + TRC
PC-198[2]	TA6 (76%) + SA (20%) + TRC (4%)	1300-1250		28	Ap + Lc + Di + Kfs + REE-Kfs + REE-phase
PC-201	TA6 (46%) + SA (50%) + TRC (4%) + 10% H2O	1300-1250		28	Ap + Lsc + REE-Di + REE-Kfs + REE-phase
PC-207	TA6 (46%) + SA (50%) + TRC (4%) + 10% H2O	1350		24	Ap + Lc? + Di? + Fl
PC-209	TA6 (76%) + SA (20%) + TRC (4%) (Graphite)	1300-1250	CCO[3]	28	Quench Ap + melt
PC-212	TA6 (76%) + SA (20%) + TRC (4%)	1300-1250	NNO[1]	28	Quench Ap + melt
PC-213	TA6 (76%) + SA (20%) + TRC (4%)	1300-1250	RRO[4]	28	Ap + small melt pockets
PC-214	TA6 (76%) + SA (20%) + TRC (4%)	1300-1250	NNO[1]	28	Quench Ap + melt
PC-215	TA9 (76%) + SA (20%) + TRC (4%)	1350		24	Quench Ap + melt

Run #	Composition	T (°C)	Buffer	Duration (hours)	Phases Present
PC-216	TA9 (76%) + SA (20%) + TRC (4%)	1300-1250	NNO[1]	28	Quench Ap + melt
	TA9 (76%) + SA (20%) + TRC (4%) (Graphite)	1300-1250	CCO[3]	28	Quench Ap + melt
PC-219	TA6 (46%) + SA (50%) + TRC (4%) + 10% H2O	1300-1250	NNO[5]	28	Ap + melt + REE-Kfs + REE-phase + Fl
PC-221	TA6 (46%) + SA (50%) + TRC (4%) + 10% H2O	1300-1250	MH	28	Ap + melt + REE-Kfs + REE-phase + Fl
PC-222	TA6 (46%) + SA (50%) + TRC (4%) + 10% H2O	1300-1250	IW	28	Ap + melt + Fl
PC-224	CAA (76%) + SA (20%) + TRC (4%)	1300-1250		48	Ap + Lc + REE-phase
	TA6 (76%) + SA (20%) + TRC (4%)	1300-1250		48	Lsc + quench Ap
	TA9 (76%) + DA (20%) + TRC (4%)	1300-1250		48	Ap + Di + Lsc + Fl
PC-228	TA6 (64%) + SA (32%) + TRC (4%)	1300-1250		48	Ap + Lsc

[1] runs with Ni foil
[2] experimental run at 2 GPa
[3] experiments buffered at CCO using a graphite capsule
[4] experiment buffer at RRO using Re and ReO_2
[5] runs with NNO powder in double capsule configuration

Table 3.3: Major element compositions of quenched melts from the run products (wt. %) obtained with EMPA. * Calculated as average of other runs containing Co and Ni.

Run #	PC-178	PC-197	PC-224	PC-178	PC-179	PC-224	PC-186	PC-189	PC-179	PC-196	PC-198	PC-201	PC-207	PC-219	PC-221	PC-222	PC-228
Mixture	CAA	CAA	CAA	TA9	TA9	TA9	LS6	LS6	TA6	TA6	TA6	TA6	TA6	TA6	TA6	TA6	TA6
# of analyses	11	7	7	5	4	5	7	10	6	6	6	5	4	8	5	7	4
K_2O	**0.03**	0.02	0.03	2.76	1.75	3.01	0.65	1.07	2.39	2.09	1.82	1.93	1.66	2.79	2.00	2.16	1.72
CaO	**50.29**	51.15	51.92	32.72	39.09	39.42	37.99	37.77	34.45	37.42	38.77	36.42	38.08	34.17	34.76	33.59	37.59
Na_2O	**0.40**	0.54	0.92	0.42	0.19	0.63	0.47	0.53	0.63	0.90	1.41	2.22	1.81	3.62	0.91	1.89	0.65
MgO	**0.23**	0.26	0.31	7.37	5.13	5.64	13.37	11.12	6.86	5.58	5.78	6.42	5.28	7.27	6.70	8.39	6.39
Al_2O_3	**0.05**	0.17	0.10	5.31	2.89	1.75	1.51	1.33	3.86	4.20	1.37	3.37	3.21	3.61	3.98	3.54	3.23
FeO	**0.01**	0.00	0.00	0.04	0.02	0.01	4.17	3.38	0.04	0.01	0.01	0.01	0.01	0.01	0.03	0.01	0.01
SiO_2	**0.18**	0.13	0.09	22.50	14.06	10.93	19.08	16.89	17.74	17.36	4.26	12.70	11.87	14.06	14.65	14.14	13.05
P_2O_5	**8.28**	9.50	11.09	4.15	9.60	8.44	3.85	3.91	8.24	8.67	9.24	10.95	14.52	4.61	9.50	5.46	9.33
Cl	**0.09**	0.03	0.00	0.17	0.10	0.12	0.07	0.06	0.24	0.07	0.03	0.01	0.02	0.10	0.01	0.03	0.04
F	**1.39**	0.14	0.19	0.84	1.05	0.75	0.92	0.80	1.01	0.34	0.13	0.15	0.22	0.06	0.15	0.08	0.14
SO_3	**0.02**	0.04	0.07	0.03	0.04	0.14	0.17	0.42	0.02	0.04	0.02	0.01	0.03	0.03	0.05	0.03	0.09
CoO				0.17	0.12	0.03			0.13	0.01	0.06*	0.01	0.00	0.06*	0.26	0.00	0.00
NiO				4.56	3.73	0.00			2.12	0.00	3.47*	0.00	0.00	3.47*	0.00	0.00	0.00
TOTAL	**60.95**	61.97	64.73	81.01	77.75	70.85	82.26	77.28	77.72	76.69	62.83	74.18	76.70	70.29	72.99	69.31	72.22

Table 3.4: Average trace element (ppm) compositions of quenched melts from run products obtained from LA-ICP-MS analyses. b.d.= below detection limit. Limits of detection for each analysis included in electronic supplementary data. * Runs doped with trace elements (shown with larger font).

Run #	PC-178		PC-197*		PC-224*		PC-178		PC-179*		PC-186		PC-189*		PC-179*	
Mixture	CAA		CAA		CAA		TA9		TA9		LS6		LS6		TA6	
# of analyses	8	2σ	6	2σ	7	2σ	6	2σ	6	2σ	6	2σ	10	2σ	5	2σ
Rb	b.d.	b.d.	1517.67	538.70	4302.00	691.59	b.d.	b.d.	3515.00	434.74	2.87	0.19	4126.30	326.30	b.d.	b.d.
Cs	0.01	0.01	886.83	335.75	4791.43	769.08	b.d.	b.d.	1754.50	235.61	3.58	0.38	3601.20	244.03	2469.80	367.40
Sr	468.71	11.36	3442.50	66.25	2460.57	38.87	284.67	17.01	2021.33	98.93	289.50	2.84	4782.60	200.43	3932.20	368.38
La	2298.75	89.74	2318.50	71.56	1210.86	21.17	1137.67	37.66	1831.83	39.79	559.83	26.18	2838.10	181.62	4225.20	347.54
Ce	2894.75	133.93	2.74	0.14	6.21	0.12	1327.33	62.57	1341.33	101.15	762.83	19.31	726.50	82.65	1604.60	118.07
Pr	206.48	7.84	0.17	0.01	0.10	0.00	99.55	4.49	91.55	4.32	51.53	1.63	53.20	6.97	111.00	3.67
Nd	580.94	0.14	0.57	400.87	0.36	0.01	300.00	0.03	262.02	50.12	146.48	0.03	160.34	217.80	316.48	781.53
Sm	67.04	1.67	1487.50	22.78	886.71	19.84	37.63	2.16	1373.50	89.39	19.36	1.22	1521.40	120.71	1884.40	95.63
Eu	8.49	0.21	2640.00	60.69	1896.14	31.53	4.57	0.27	1264.67	99.52	3.06	0.15	1997.50	185.30	2286.60	75.81
Gd	56.65	1.22	0.10	b.d.	0.15	0.01	32.05	2.09	26.54	2.00	15.16	0.99	19.55	2.53	31.88	1.63
Dy	35.28	0.89	b.d.	b.d.	0.13	0.00	21.72	1.24	18.14	1.22	10.56	0.65	15.78	1.63	21.94	0.88
Y	245.39	6.84	0.55	0.01	0.56	0.01	142.88	5.48	119.80	6.27	67.20	4.48	102.77	9.43	145.40	7.59
Yb	15.26	0.63	1257.00	57.55	1014.71	25.43	9.39	0.53	1799.67	36.76	5.66	0.32	2942.70	171.54	3141.20	140.49
Lu	2.05	0.11	0.98	0.07	1.00	0.02	1.35	0.07	3.65	0.20	0.66	0.03	3.70	0.22	4.12	0.24
Ti	1720.25	89.96	869.00	13.10	904.04	5.31	1737.83	195.72	1393.33	87.70	636.42	3.08	636.03	5.24	1675.40	132.69
Hf	0.86	0.09	62.93	5.19	51.67	1.61	0.52	0.07	565.33	50.26	0.54	0.03	3812.10	231.96	5160.60	690.81
Zr	33.09	4.19	127.40	11.23	164.54	5.06	6.48	0.82	813.17	74.45	4.51	0.19	3547.80	191.16	4469.20	604.79
U	12.03	2.14	0.30	0.03	1.27	0.03	4.44	0.24	4.55	0.31	3.94	0.06	4.67	0.07	4.51	0.36
Th	94.39	11.05	b.d.	b.d.	0.02	0.00	60.38	1.81	43.03	1.65	21.77	1.64	21.51	4.87	52.84	2.51
V	885.00	96.65	16.83	1.36	30.87	0.92	1299.83	207.87	893.67	77.35	26.63	0.88	26.60	1.39	1139.20	130.00
Nb	0.84	12.06	2876.83	0.04	4624.29	257.757	0.17	19.51	566.00	15.16	0.99	7.51	4053.10	22.99	5016.40	12.03

Run #	PC-196*		PC-198*		PC-201*		PC-207*		PC-219*		PC-221*		PC-222*		PC-228*	
Mixture	TA6		TA6		TA6		TA6		TA6		TA6		TA6		TA6	
# of analyses	10	2σ	6	2σ	6	2σ	6	2σ	5	2σ	5	2σ	5	2σ	7	2σ
Rb	3860.00	76.11	3928.00	445.41	5480.33	252.98	6628.50	521.72	7236.00	692.59	8152.00	600.27	6339.80	238.53	5003.14	274.00
Cs	2883.50	46.79	3007.00	302.31	3007.17	142.05	6414.50	497.32	3878.00	368.01	5424.00	398.88	3852.00	150.46	5441.57	325.74
Sr	3727.20	38.22	4314.83	53.61	3962.33	70.01	3704.00	116.44	4034.00	160.27	4161.40	60.56	4135.60	69.07	4063.71	78.11
La	3951.00	42.66	3963.00	80.40	2809.33	48.02	2750.50	47.09	2453.00	74.61	2919.20	89.28	3150.20	69.44	2669.00	61.61
Ce	496.83	13.60	5.17	0.16	8.11	0.14	6.88	0.07	13.73	0.66	8.41	0.32	20.01	0.26	6.60	0.10
Pr	37.66	0.67	0.48	0.02	0.33	0.00	0.33	0.01	0.27	0.01	0.36	0.02	0.35	0.01	0.31	0.01
Nd	121.71	94.88	1.92	897.79	1.11	148.88	1.12	407.72	0.92	776.58	1.18	519.69	1.20	217.44	1.15	0.04
Sm	2684.40	44.54	3180.33	96.84	1808.50	39.52	1873.50	77.53	1489.60	65.45	1859.40	66.92	1999.20	59.60	2202.57	72.07
Eu	3309.10	37.75	3649.17	48.86	2328.50	33.90	2349.33	59.92	1800.00	74.20	2232.00	89.27	2471.60	56.00	2728.00	54.87
Gd	14.22	0.39	0.70	0.14	0.33	0.00	0.31	0.02	0.25	0.01	0.31	0.02	0.44	0.02	0.43	0.02
Dy	10.94	0.36	0.75	0.07	0.33	0.01	0.34	0.02	0.29	0.02	0.33	0.02	0.37	0.01	0.46	0.02
Y	71.11	1.03	3.10	0.42	1.52	0.04	1.55	0.03	1.48	0.05	1.63	0.08	1.76	0.08	1.98	0.07
Yb	3611.60	88.08	4018.67	421.08	2756.67	62.94	2852.33	87.79	2751.40	104.09	3017.80	154.42	3157.60	111.99	2963.14	90.03
Lu	2.84	0.27	4.07	0.50	2.93	0.07	3.03	0.09	2.87	0.14	3.21	0.17	3.21	0.15	2.93	0.09
Ti	1072.60	9.47	1462.50	87.25	1065.17	14.71	1003.38	34.11	1171.40	73.36	1231.00	47.95	1132.20	17.56	1002.29	13.00
Hf	5378.40	137.31	8614.17	11348.97	4027.50	87.84	5156.00	446.32	5214.00	382.21	5796.20	380.96	5328.60	256.92	4038.71	95.95
Zr	3239.40	79.63	7764.83	10202.99	3456.50	96.14	4359.33	327.35	3588.20	286.67	4808.80	335.91	4395.80	161.38	3452.71	71.14
U	1.63	0.16	1.40	0.18	0.36	0.01	0.56	0.01	0.49	0.03	1.05	0.07	0.48	0.01	0.93	0.01
Th	21.49	0.41	0.30	0.03	0.14	0.01	0.15	0.00	0.12	0.00	0.20	0.01	0.16	0.01	0.13	0.01
V	530.98	12.85	836.67	85.61	532.50	17.67	454.32	38.09	667.80	67.18	700.20	51.87	565.92	21.79	431.11	11.98
Nb	4423.60	1.67	9748.33	0.12	5829.67	0.01	4945.67	0.04	7212.00	0.04	7198.00	0.07	6751.80	0.05	3616.43	111.65

3.2.2 Textures, composition, and zoning in apatite

Apatite is present in all run products where it was added (Table 3.2). It occurs as euhedral prismatic crystals ranging in size from ~5μm to ~50 μm and as skeletal crystals within the quenched melt (Figure 3.10 ABC). Durango apatite from the runs doped with trace elements developed compositional zoning, where the cores preserve the initial composition and the rims are enriched in the added elements (Figure 3.10 DEF) matching closely the compositions of the synthetic apatites (Figure 3.12). Run PC-196 which uses both Durango and synthetic apatite shows no zoning in apatites. The composition of apatite in PC-196 is enriched in trace elements and similar to both the apatite rims previously mentioned and the apatite produced using synthetic apatite. In the undoped runs, the composition of Durango apatite evolves towards a decrease in trace element concentrations as expected due to their loss to the melt, and increase in SiO_2 (Figure 3.12 A B). The increase in SiO_2 is unlikely to be analytical contamination from the matrix as other major elements such as MgO did not show elevation in any of the runs where it was measured (Runs #219, 221, 222, 224, 228). In the runs with CAA composition, SiO_2 content is higher in apatite than the melt itself which would indicate that Durango apatite naturally contained higher SiO_2 content. In the doped runs with Durango apatite, the composition is enriched in trace elements along with higher SiO_2 content trending away from the composition of Durango. The apatite composition (reported in Table 3.5 and Table 3.6) from the doped runs have lower totals (approximately 88-95 wt.%) compared to apatites from undoped runs (97.5-98.8 wt.%). It has been suggested that substitution of CO_2 into the P site in apatite can lower the total in EMP analyses (Chakhmouradian et al. 2017). However, Raman spectra of our apatites (Figure ES 4) does not show any discernible difference in the intensity of

the peaks associated with the carbonate component (675-725 cm^{-1}, 1070 ± 1 $cm^{-1,}$ and 1102–1107 cm^{-1}) in apatite (Chakhmouradian et al. 2017). Yet we assume that the low totals of EMP analyzes are due to the missing CO_2 . Apatite from undoped runs have higher totals and lower SiO_2 than doped runs (Figure 3.12 C). Apatite from the doped runs shows a positive correlation between elevated SiO_2 content and higher concentrations of trace elements (Table 3.5; Figure 3.12 A B). A trend is also observed where CaO and P_2O_5 content decreases as SiO_2 increases (Figure 3.12 D, G). The F and Cl content of apatites is lower in the runs with synthetic apatite which are hydroxylapatite compared to fluorapatites of Durango.

Table 3.5: Average major element compositions (wt. %) of apatites from run products analyzed by EPMA and stoichiometry of apatite calculated based on (Ketcham, 2015). OH apfu calculated assuming 1 total anion in the halogen site. DA = Durango Apatite, SA = synthetic apatite.

Run #	PC-178		PC-197		PC-224		PC-178	
Trace El.	Undoped		Doped		Doped		Undoped	
Ap. Type	DA		SA		SA		DA	
Mixture	CAA		CAA		CAA		TA9	
n	10	1σ	10	1σ	10	1σ	10	1σ
Na_2O	0.07	0.08	0.24	0.02	0.30	0.04	0.04	0.05
K_2O	0.02	0.01	0.02	0.01	0.02	0.01	0.07	0.01
CaO	53.62	0.56	53.16	0.49	52.97	0.41	53.30	0.78
MgO					0.07	0.01		
Al_2O_3					0.02	0.01		
FeO	0.01	0.02	0.01	0.01	0.01	0.01	0.01	0.01
V_2O_3	0.06	0.05	0.1	0.05	0.08	0.04	0.06	0.05
MnO	0.04	0.03	0	0.01	0.02	0.01	0.03	0.02
SrO	0.11	0.03	0.26	0.04	0.19	0.04	0.15	0.03
BaO	0.08	0.06	0.09	0.05	0.09	0.06	0.09	0.09
La_2O_3	0.17	0.15	0.31	0.05	0.19	0.10	0.19	0.10
Ce_2O_3	0.39	0.14	0.12	0.08	0.11	0.10	0.47	0.09
Pr_2O_3	0.4	0.08	0.37	0.11	0.30	0.12	0.42	0.10
Nd_2O_3	0.09	0.10	0.05	0.05	0.07	0.09	0.09	0.08
SiO_2	0.53	0.31	1.45	0.20	1.03	0.40	0.70	0.61
P_2O_5	39.5	0.91	34.78	0.80	37.32	1.17	39.56	1.37
SO_3	0.13	0.14	0.08	0.02	0.10	0.03	0.15	0.18
F	2.35	0.17	0.33	0.03	0.55	0.04	2.24	0.25
Cl	0.19	0.06	0.08	0.02	0.01	0.01	0.17	0.03
$-O=(F,Cl)_2$	1.03	0.08	0.16	0.01	0.23	0.02	0.98	0.10
Total	98.82	1.15	91.61	0.67	93.66	1.17	98.75	1.82
Structural formulae calculated on the basis of 8 cations:								
Na	0.012	0.013	0.041	0.004	0.051	0.006	0.007	0.008
K	0.003	0.002	0.002	0.001	0.002	0.001	0.007	0.002
Ca	4.981	0.049	5.122	0.045	5.010	0.037	4.954	0.030
Mg					0.010	0.002		
Al					0.001	0.001		
Fe	0.001	0.001	0.001	0.001	0.001	0.001	0.001	0.001
V	0.003	0.003	0.006	0.003	0.004	0.003	0.004	0.003
Mn	0.003	0.002	0.000	0.000	0.001	0.001	0.002	0.002
Sr	0.006	0.001	0.013	0.002	0.010	0.002	0.008	0.001
Ba	0.003	0.002	0.003	0.002	0.003	0.002	0.003	0.003
La	0.006	0.005	0.010	0.002	0.006	0.003	0.006	0.003
Ce	0.012	0.005	0.004	0.002	0.003	0.003	0.015	0.003
Pr	0.013	0.003	0.012	0.003	0.010	0.004	0.013	0.003
Nd	0.003	0.003	0.002	0.002	0.002	0.003	0.003	0.003
Si	0.047	0.027	0.130	0.018	0.091	0.037	0.061	0.054
P	2.9	0.051	2.647	0.055	2.788	0.061	2.905	0.064
S	0.008	0.009	0.005	0.002	0.006	0.002	0.010	0.012
∑	*8*		*8*		*8*		*8*	
F	0.644	0.047	0.094	0.008	0.153	0.011	0.614	0.064
Cl	0.028	0.009	0.013	0.002	0.001	0.001	0.024	0.004
OH	0.327	0.052	0.893	0.009	0.846	0.010	0.362	0.064

Run #	PC-179		PC-224		PC-186		PC-189	
Trace El.	Doped		Doped		Undoped		Doped	
Ap. Type	DA		DA		DA		DA	
Mixture	TA9		TA9		LS6		LS6	
n	7	1σ	10	1σ	10	1σ	8	1σ
Na_2O	0.02	1σ	0.03	0.01	0.07	0.10	0.00	0.00
K_2O	0.05	0.01	0.09	0.01	0.04	0.01	0.04	0.01
CaO	52.92	0.58	51.35	0.51	54.32	0.52	48.94	0.55
MgO			0.69	0.05				
Al_2O_3			0.01	0.01				
FeO	0.01	0.01	0.01	0.01	0.27	0.06	0.36	0.12
V_2O_3	0.09	0.04	0.08	0.04	0.10	0.02	0.11	0.04
MnO	0.04	0.03	0.01	0.01	0.00	0.00	0.01	0.01
SrO	0.28	0.04	0.39	0.04	0.12	0.04	0.43	0.06
BaO	0.06	0.04	0.09	0.04	0.07	0.07	0.06	0.05
La_2O_3	0.38	0.12	0.75	0.12	0.25	0.09	1.74	0.09
Ce_2O_3	0.40	0.12	0.31	0.08	0.40	0.12	0.52	0.10
Pr_2O_3	0.36	0.09	0.36	0.12	0.37	0.09	0.36	0.08
Nd_2O_3	0.06	0.05	0.06	0.07	0.11	0.07	0.08	0.09
SiO_2	2.18	0.09	3.63	0.14	1.42	0.91	4.24	0.12
P_2O_5	35.91	0.40	33.34	0.73	37.89	1.57	31.87	0.44
SO_3	0.03	0.03	0.02	0.02	0.27	0.05	0.21	0.02
F	1.96	0.11	1.71	0.05	1.21	0.07	0.93	0.04
Cl	0.16	0.01	0.14	0.01	0.06	0.01	0.07	0.02
$-O=(F,Cl)_2$	0.86	0.05	0.75	0.02	0.52	0.03	0.41	0.02
Total	95.78	0.62	93.82	0.96	97.50	1.27	90.39	0.86
Structural formulae calculated on the basis of 8 cations:								
Na	0.004	0.003	0.005	0.002	0.012	0.017	0.000	0.000
K	0.006	0.001	0.011	0.001	0.004	0.001	0.005	0.001
Ca	5.032	0.054	4.948	0.040	5.012	0.039	4.905	0.066
Mg			0.092	0.007				
Al			0.000	0.000				
Fe	0.000	0.000	0.001	0.001	0.020	0.005	0.028	0.009
V	0.006	0.003	0.005	0.002	0.005	0.001	0.007	0.002
Mn	0.003	0.002	0.000	0.001	0.000	0.000	0.001	0.001
Sr	0.015	0.002	0.020	0.002	0.006	0.002	0.024	0.003
Ba	0.002	0.001	0.003	0.001	0.002	0.002	0.002	0.002
La	0.012	0.004	0.025	0.004	0.008	0.003	0.060	0.003
Ce	0.013	0.004	0.010	0.003	0.013	0.004	0.018	0.004
Pr	0.012	0.003	0.012	0.004	0.012	0.003	0.012	0.002
Nd	0.002	0.002	0.002	0.002	0.004	0.002	0.003	0.003
Si	0.193	0.008	0.327	0.014	0.123	0.079	0.397	0.007
P	2.698	0.029	2.538	0.034	2.762	0.092	2.524	0.052
S	0.002	0.002	0.001	0.001	0.017	0.003	0.015	0.001
∑	*8*		*8*		*8*		*8*	
F	0.549	0.031	0.487	0.017	0.330	0.019	0.277	0.014
Cl	0.024	0.002	0.021	0.002	0.009	0.002	0.011	0.003
OH	0.427	0.031	0.492	0.016	0.661	0.020	0.712	0.014

Run #	PC-179		PC-196		PC-198		PC-201	
Trace El.	Doped		Doped		Doped		Doped	
Ap. Type	DA		DA + SA		SA		SA	
Mixture	TA6		TA6		TA6		TA6	
n	10	1σ	12	1σ	9	1σ	13	1σ
Na_2O	0.02	0.02	0.13	0.03	0.42	0.04	0.48	0.04
K_2O	0.07	0.01	0.12	0.01	0.29	0.05	0.10	0.01
CaO	52.08	0.34	50.61	0.41	49.99	0.99	50.29	0.64
MgO								
Al_2O_3								
FeO	0.02	0.02	0.00	0.01	0.00	0.01	0.01	0.02
V_2O_3	0.09	0.04	0.08	0.04	0.10	0.04	0.07	0.05
MnO	0.02	0.01	0.00	0.01	0.01	0.01	0.00	0.01
SrO	0.46	0.04	0.38	0.04	0.37	0.05	0.42	0.04
BaO	0.12	0.06	0.08	0.08	0.08	0.06	0.11	0.06
La_2O_3	0.71	0.12	0.56	0.07	0.32	0.08	0.44	0.08
Ce_2O_3	0.32	0.09	0.21	0.10	0.12	0.09	0.10	0.13
Pr_2O_3	0.40	0.07	0.36	0.09	0.34	0.11	0.35	0.12
Nd_2O_3	0.13	0.08	0.02	0.03	0.02	0.05	0.04	0.04
SiO_2	2.59	0.07	3.72	0.14	1.73	0.26	2.90	0.08
P_2O_5	35.42	0.40	31.88	0.41	34.13	0.67	32.84	0.49
SO_3	0.01	0.01	0.02	0.02	0.02	0.01	0.02	0.02
F	2.02	0.08	0.79	0.07	0.35	0.04	0.42	0.04
Cl	0.22	0.02	0.13	0.01	0.02	0.01	0.02	0.01
$-O=(F,Cl)_2$	0.90	0.03	0.36	0.03	0.15	0.02	0.18	0.02
Total	95.59	0.36	89.47	0.57	88.44	1.09	88.79	0.93
Structural formulae calculated on the basis of 8 cations:								
Na	0.003	0.004	0.023	0.005	0.075	0.007	0.086	0.007
K	0.008	0.002	0.014	0.001	0.034	0.006	0.012	0.002
Ca	4.989	0.030	5.040	0.029	4.983	0.047	4.992	0.027
Mg								
Al								
Fe	0.001	0.002	0.000	0.001	0.000	0.001	0.001	0.002
V	0.005	0.002	0.005	0.002	0.006	0.002	0.005	0.003
Mn	0.002	0.001	0.000	0.001	0.001	0.001	0.000	0.001
Sr	0.024	0.002	0.020	0.002	0.020	0.003	0.023	0.002
Ba	0.004	0.002	0.003	0.003	0.003	0.002	0.004	0.002
La	0.023	0.004	0.019	0.002	0.011	0.003	0.015	0.003
Ce	0.010	0.003	0.007	0.003	0.004	0.003	0.003	0.004
Pr	0.013	0.002	0.012	0.003	0.011	0.004	0.012	0.004
Nd	0.004	0.003	0.001	0.001	0.001	0.002	0.001	0.001
Si	0.232	0.008	0.346	0.013	0.162	0.025	0.269	0.009
P	2.681	0.033	2.508	0.031	2.688	0.046	2.576	0.035
S	0.000	0.001	0.001	0.001	0.002	0.001	0.001	0.001
∑	*8*		*8*		*8*		*8*	
F	0.571	0.026	0.233	0.022	0.102	0.012	0.123	0.012
Cl	0.033	0.002	0.021	0.002	0.003	0.002	0.003	0.002
OH	0.396	0.026	0.746	0.021	0.895	0.012	0.874	0.011

Run #	PC-207		PC-219		PC-221		PC-222	
Trace El.	Doped		Doped		Doped		Doped	
Ap. Type	SA		SA		SA		SA	
Mixture	TA6		TA6		TA6		TA6	
n	10	1σ	10	1σ	9	1σ	10	1σ
Na_2O	0.35	0.03	0.52	0.04	0.37	0.04	0.41	0.03
K_2O	0.09	0.02	0.10	0.02	0.06	0.01	0.09	0.01
CaO	51.41	0.54	52.44	0.34	52.57	0.22	51.41	0.30
MgO			0.63	0.04	0.57	0.02	0.65	0.03
Al_2O_3			0.01	0.01	0.01	0.01	0.01	0.02
FeO	0.01	0.01	0.01	0.01	0.02	0.02	0.03	0.02
V_2O_3	0.06	0.05	0.07	0.03	0.06	0.04	0.10	0.05
MnO	0.00	0.01	0.02	0.02	0.02	0.02	0.01	0.01
SrO	0.41	0.04	0.41	0.02	0.39	0.03	0.34	0.04
BaO	0.09	0.06	0.09	0.08	0.08	0.07	0.06	0.06
La_2O_3	0.40	0.04	0.37	0.09	0.40	0.10	0.38	0.08
Ce_2O_3	0.10	0.08	0.13	0.08	0.13	0.11	0.09	0.06
Pr_2O_3	0.35	0.06	0.32	0.10	0.34	0.06	0.36	0.08
Nd_2O_3	0.02	0.03	0.00	0.01	0.01	0.03	0.03	0.06
SiO_2	2.61	0.09	2.78	0.21	2.28	0.08	2.70	0.10
P_2O_5	34.83	0.49	33.77	1.10	35.55	0.46	34.47	0.45
SO_3	0.02	0.02	0.00	0.01	0.00	0.01	0.01	0.01
F	0.44	0.04	0.38	0.05	0.39	0.05	0.51	0.04
Cl	0.01	0.01	0.01	0.01	0.02	0.01	0.01	0.00
$-O=(F,Cl)_2$	0.19	0.02	0.16	0.02	0.17	0.02	0.22	0.02
Total	91.39	0.94	92.23	1.18	93.46	0.39	91.89	0.61
Structural formulae calculated on the basis of 8 cations:								
Na	0.061	0.006	0.089	0.007	0.063	0.006	0.071	0.005
K	0.010	0.002	0.011	0.002	0.007	0.002	0.011	0.001
Ca	4.972	0.015	4.979	0.045	4.951	0.025	4.924	0.022
Mg			0.083	0.005	0.074	0.003	0.087	0.005
Al			0.001	0.001	0.000	0.000	0.001	0.001
Fe	0.001	0.001	0.001	0.001	0.001	0.001	0.002	0.001
V	0.003	0.003	0.004	0.002	0.004	0.002	0.006	0.003
Mn	0.000	0.001	0.001	0.002	0.002	0.001	0.001	0.001
Sr	0.021	0.002	0.021	0.001	0.020	0.001	0.018	0.002
Ba	0.003	0.002	0.003	0.003	0.003	0.002	0.002	0.002
La	0.013	0.001	0.012	0.003	0.013	0.003	0.013	0.003
Ce	0.003	0.003	0.004	0.003	0.004	0.004	0.003	0.002
Pr	0.011	0.002	0.010	0.003	0.011	0.002	0.012	0.002
Nd	0.000	0.001	0.000	0.000	0.000	0.001	0.001	0.002
Si	0.236	0.010	0.247	0.019	0.201	0.007	0.241	0.008
P	2.662	0.015	2.533	0.059	2.645	0.027	2.609	0.033
S	0.001	0.001	0.000	0.000	0.000	0.001	0.001	0.001
∑	*8*		*8*		*8*		*8*	
F	0.126	0.011	0.106	0.015	0.109	0.012	0.144	0.010
Cl	0.002	0.001	0.001	0.001	0.002	0.002	0.002	0.001
OH	0.872	0.011	0.893	0.015	0.888	0.012	0.854	0.010

Run #	PC-228	
Trace El.	Doped	
Ap. Type	SA	
Mixture	TA6	
n	10	1σ
Na_2O	0.12	0.03
K_2O	0.05	0.01
CaO	51.77	0.29
MgO	0.38	0.02
Al_2O_3	0.02	0.01
FeO	0.01	0.01
V_2O_3	0.09	0.05
MnO	0.00	0.00
SrO	0.35	0.05
BaO	0.08	0.05
La_2O_3	0.49	0.11
Ce_2O_3	0.14	0.09
Pr_2O_3	0.42	0.13
Nd_2O_3	0.04	0.06
SiO_2	2.30	0.06
P_2O_5	36.81	0.46
SO_3	0.10	0.01
F	0.55	0.03
Cl	0.01	0.01
$-O=(F,Cl)_2$	0.23	0.01
Total	93.66	0.65
Structural formulae calculated on the basis of 8 cations:		
Na	0.021	0.004
K	0.005	0.001
Ca	4.903	0.016
Mg	0.000	0.002
Al	0.005	0.000
Fe	0.000	0.001
V	0.018	0.003
Mn	0.003	0.000
Sr	0.016	0.002
Ba	0.004	0.002
La	0.016	0.004
Ce	0.004	0.003
Pr	0.013	0.004
Nd	0.001	0.002
Si	0.203	0.005
P	2.754	0.022
S	0.001	0.001
∑	*8*	
F	0.155	0.008
Cl	0.002	0.001
OH	0.843	0.008

Table 3.6: Average trace element compositions (ppm) of apatites analyzed by LA-ICP-MS. *b.d.= not detected due to below detection. DA = Durango Apatite, SA = synthetic apatite.

Run #	PC-178		PC-197		PC-224		PC-178	
Trace El.	Undoped		Doped		Doped		Undoped	
Ap. Type	DA		SA		SA		DA	
Mixture	CAA		CAA		CAA		TA9	
n	10	2σ	10	2σ	5	2σ	7	2σ
Rb	b.d.	b.d.	49.1	4.6	62.86	19.72	b.d.	b.d.
Cs	b.d.	b.d.	6.1	2	25.65	14.55	b.d.	b.d.
Sr	269.6	44.1	1677.8	33.9	1290	64.78	420.9	42.5
La	1512.4	440.8	2464.4	134.6	1412.4	63.67	3288.6	348
Ce	2052.7	486.8	3	0.4	7.87	0.14	4292.9	386.2
Pr	167.8	35.2	b.d.	b.d.	0.17	0.01	341.9	33.3
Nd	549.2	107.2	0.9	b.d.	0.61	0.02	1022.9	85.9
Sm	71	12.3	2902	145.5	1594.2	32.3	128.9	12.5
Eu	8.1	1.7	2035.9	68.1	1456.2	34.04	14.8	1.1
Gd	62.5	11.1	b.d.	b.d.	0.28	0.05	108.6	9.6
Dy	37.7	6.7	b.d.	b.d.	0.16	0.03	63.7	5.1
Y	231.2	42.7	0.4	b.d.	0.61	0.03	418.7	38.4
Yb	12.8	2.7	1330.4	75.3	862.4	29.17	21.8	2.7
Lu	1.6	0.3	0.7	b.d.	0.76	0.04	2.9	0.4
Ti	807.2	9.9	868.2	8	905	6.47	863	10.3
Hf	0.03	0.02	2	0.5	1.01	0.05	b.d.	b.d.
Zr	2.8	1	9.5	1	5.38	0.39	b.d.	b.d.
U	3.2	1.2	b.d.	b.d.	0.1	0.01	7.6	1.9
Th	101.4	12.1	b.d.	b.d.	0.02	0.01	154.9	27.8
V	16	8.6	13.5	6.5	18.73	2.89	b.d.	b.d.
Nb	b.d.	b.d.	202.8	12.1	207.8	13.25	b.d.	b.d.

Run #	PC-179		PC-224		PC-186		PC-189	
Trace El.	Doped		Doped		Undoped		Doped	
Ap. Type	DA		DA		DA		DA	
Mixture	TA9		TA9		LS6		LS6	
n	6	2σ	9	2σ	7	2σ	6	2σ
Rb	56.8	59	9.78	1.09	b.d.	b.d.	11.41	13.21
Cs	23.8	21.9	0.6	0.28	b.d.	b.d.	10.78	13.5
Sr	1516	215.2	2646.11	73.05	230.3	21.9	3341.67	871.3
La	3811.5	563.3	5115.67	469.17	2016	95.5	14953.33	434.21
Ce	3212.3	418.3	1711.67	140.83	2663.9	96.5	3346.67	59.16
Pr	259.3	29.5	154.09	13.13	225.7	6.2	300.67	7.01
Nd	831.3	88.8	535.33	47.3	748.1	20.7	1048.33	20.6
Sm	4835	1072.6	5572.67	508.49	101.8	2.3	11960	464.23
Eu	3808.3	909.5	5919.11	510.5	14.9	0.7	14516.67	718.95
Gd	86.3	1.2	75.19	6.96	81.7	3.3	133.05	11.46
Dy	53.2	2.8	45.15	4.67	45.4	1.6	83.83	12.89
Y	351.1	43.7	258.98	28.35	262.3	9.5	477.17	18.81
Yb	3003.3	631.2	4077.22	539.56	12.8	0.8	8550	152.75
Lu	5.8	0.4	4.65	0.62	1.4	0.1	9.92	1.34
Ti	863.8	24.9	848.22	5.16	879.6	8.5	788.67	7.05
Hf	33.6	1.8	236.54	13.95	b.d.	b.d.	273.83	25.16
Zr	113.8	17.6	518.5	80.07	b.d.	b.d.	492.67	46.33
U	4	0.6	4.31	0.76	1.1	0.9	0.95	4.22
Th	113.1	10.4	102.12	19.72	108.8	5.3	199.83	28.66
V	b.d.	b.d.	7.04	0.39	b.d.	b.d.	29	-
Nb	7.6	5.3	47.57	8.65	b.d.	b.d.	32.87	13.11

Run #	PC-179		PC-196		PC-198		PC-201	
Trace El.	Doped		Doped		Doped		Doped	
Ap. Type	DA		DA + SA		SA		SA	
Mixture	TA6		TA6		TA6		TA6	
n	8	2σ	10	2σ	7	2σ	10	2σ
Rb	b.d.	b.d.	36.4	27.5	70.8	32.1	37.95	17.06
Cs	5.5	4.9	26.3	29.8	36	32	7.74	9.66
Sr	3150	253.9	2592.3	34.8	2639.7	97.7	2881.6	18.13
La	6466.3	350.5	4538.6	86	2382	100.7	3370.4	50.42
Ce	2666.3	181.5	679	11.2	4.2	0.4	9.65	0.53
Pr	213	11.9	62.3	1.2	1.1	0.4	0.5	0.03
Nd	686.4	30.6	222.5	3.4	6.2	2.3	1.95	0.09
Sm	4602.5	418.8	5103	80.9	3473.4	123.3	3535.6	59.71
Eu	5040	466.2	5303	141	3768.7	135.4	3813.9	59.4
Gd	75.4	3.6	32	1.4	5.9	2.1	0.51	0.07
Dy	43.9	1.8	20.9	0.8	4.1	1.3	0.56	0.03
Y	271.4	13.2	115.4	2.5	3.8	0.9	2.22	0.07
Yb	3808.8	397.1	3874	79.6	3467.9	116.3	3314.2	47.78
Lu	5.1	0.3	4	0.1	3.8	0.6	3.21	0.07
Ti	830.6	8.2	838.9	12.1	839	19.9	831.9	5.38
Hf	266.3	39.5	457	22.2	94.2	11.5	377.79	16.51
Zr	543.9	71.1	661.3	16.3	259.8	29.9	677.7	14.32
U	3.9	0.5	3.1	0.1	1.9	0.4	0.67	0.03
Th	92.8	6.3	53.9	1.6	1.1	0.4	0.31	0.01
V	20.1	5.6	29.9	10.3	46.8	12	11.06	3.81
Nb	40.2	9.7	72.9	20.8	242.6	84.7	84.04	20.19

Run #	PC-207		PC-219		PC-221		PC-222	
Trace El.	Doped		Doped		Doped		Doped	
Ap. Type	SA		SA		SA		SA	
Mixture	TA6		TA6		TA6		TA6	
n	10	2σ	9	2σ	9	2σ	7	2σ
Rb	60.8	31.17	39.76	17.89	19.79	7.96	49.51	39.41
Cs	26.77	30.99	8.47	10.05	5.59	7.28	16.91	25.56
Sr	2731.8	35.86	2878.11	18.7	3746.44	32.68	2839.14	18.28
La	3337.9	37.96	3319.33	81.71	3271.33	66.3	3249.57	40.73
Ce	8.55	0.14	14.72	2.14	7.7	1.08	14.67	2.83
Pr	0.51	0.01	0.53	0.02	0.51	0.02	0.48	0.01
Nd	2.01	0.06	2.05	0.05	1.95	0.16	1.88	0.05
Sm	3588.2	38.95	3563.22	45.64	3526.89	59.2	3392.71	28.79
Eu	3802.3	31.24	3973	62.4	4017	68.29	3825.86	25.57
Gd	0.54	0.03	0.51	0.03	0.52	0.02	0.71	0.08
Dy	0.58	0.03	0.59	0.03	0.56	0.04	0.55	0.02
Y	2.13	0.03	2.32	0.09	2.24	0.06	2.2	0.04
Yb	3095.7	43.68	3302.67	51.91	3233	63.48	3110.43	44.43
Lu	2.95	0.04	3.17	0.06	3.14	0.08	2.94	0.05
Ti	845.02	6.84	862.72	4.44	863.52	4.35	862	11.92
Hf	425.19	32.1	449.03	19.03	333.66	10.69	409.06	44.54
Zr	672.96	21.26	701.38	18.08	617.98	20.8	710.26	33.92
U	0.57	0.02	0.42	0.01	0.28	0.01	0.5	0.02
Th	0.34	0.01	0.38	0.01	0.33	0.02	0.31	0.01
V	6.42	2.39	6.94	1.66	3.85	0.46	7.46	3.31
Nb	61.4	23.78	79.61	18.02	53.1	4.05	88.89	51.82

Run #	PC-228	
Trace El.	Doped	
Ap. Type	SA	
Mixture	TA6	
n	10	2σ
Rb	6.71	0.5
Cs	0.63	0.54
Sr	2380	30.36
La	3962.2	79.19
Ce	8.7	0.34
Pr	0.52	0.01
Nd	2.24	0.05
Sm	5054.9	84.41
Eu	5450.8	115.5
Gd	0.82	0.04
Dy	0.91	0.03
Y	3.11	0.08
Yb	3877.8	85.55
Lu	3.58	0.09
Ti	862.54	2.68
Hf	289.09	7.21
Zr	516.67	15.1
U	0.72	0.1
Th	0.27	0.02
V	2.32	0.33
Nb	2.24	0.05

3.2.3 Apatite/melt partition coefficients

Apatite/melt partition coefficients (D_i) are reported in Table 3.7 and Figure 3.13. Apatite and melt analyses were carefully screened for any outliers, contamination with the neighbouring phases or with the composition of unreacted Durango apatite core when used for the partition coefficients calculation. Apatite analyses with anomalously high concentrations in Si, Mg, and Al (Si >15000 ppm, Mg >5000 ppm, and >500 ppm Al) were excluded on the basis that the analysis may be contaminated with the melt composition. Melt analysis with anomalously low concentrations of Si, Mg, and Al (with the exception of carbonate (CAA) runs) were excluded on the basis that the analysis is contaminated with the inclusion of apatite or other phases. When melt from the same run showed a range of compositions, the preference was given to the analyzes obtained in larger melt pockets. Rims on Durango apatites showed some compositional variation and the compositions diverging from the initial Durango composition (Figure 3.12 ABEF) were selected.

The effect of melt composition on D_i in apatite was examined in the runs with Durango apatite in order to examine a larger range of elements including the trace elements which were not added to the mixture but naturally occurring in Durango apatite (Figure 3.13 A). Most elements are incompatible or very weakly compatible when apatite is equilibrated with a carbonate melt (Figure 3.13 A). In the runs with silicate melts REE, Yb, Ti, and Th are compatible and $D_{REE,Yb,Ti,Th}$ increase in order from runs with TA6 , TA9 and LS6 mixture, whereas $D_{Sr,\ Hf,\ Zr}$ are similar in all the compositions. Rb, Cs, and Nb (as well as Hf, Zr, V) are extremely incompatible in all studied compositions. Sr is not sensitive to the melt composition and shows similar compatibility to REE in carbonate melts $D_{Sr} \sim D_{REE}$ but $D_{Sr} < D_{REE}$ in silicate melts. U is mostly incompatible in all melt compositions with

Durango apatite but becomes more compatible in runs with synthetic apatite. It is unclear if melt composition or U valence state affects compatibility. Th shows compatibility in all experimental melt compositions with higher compatibility in silicic melts. Major elements Na, K, Mg, Al, and Fe are highly incompatible in apatite. F and Cl are compatible in apatite. F shows higher D_F in experiments with synthetic apatite. The trend of increasing D with an increasing SiO_2 in the melt is evident in runs with Durango apatite except for runs with LS6 composition. In runs with synthetic apatite, the Ds in apatite show a much less pronounced difference between runs of different composition (CAA vs TA6) (Figure 3.13 B).

This study observed no effect of temperature, pressure or H_2O (5 wt.% and 10 wt.%) on D_i in apatite (Figure 3.14 A B, Figure 3.15 A) which is in agreement with Watson and Green (1981). The Run with TA6 composition at 2 GPa produced low D_i in apatite compared to the runs with TA6 composition at 1 GPa (Figure 3.14 B). However, due to the pressure effect on the solidus and extensive crystallization of diopside, the melt of the 2 GPa run contains only 4.3 wt.% SiO_2 (compared to 12.7-17.7 wt.% SiO_2 in 1 GPa runs, Table 3.3). As a result, trace element partitioning is similar to that in the runs with carbonate melt (CAA) at 1 GPa and the observed difference is due to melt composition rather than the effect of pressure. The effect of fO_2 on element partitioning in apatite examined with HM, WM, and IW buffers cover log fO_2 range of 9 log units. It shows no effect of fO_2 on REE, Sr, and HFSE partitioning (Figure 3.15 B). D of the highly incompatible Rb, Cs, U, V, Nb is lower in the most oxidized run with the HM buffer. However, due to the low concentrations of these elements, the difference between the runs with different buffers is within the uncertainties.

Error bars were calculated as the propagated error in the quotient of two variables: $E_{D_{el}} = \left(\sqrt{\left(\frac{Cap_{std}}{Cap_{avg}}\right)^2 + \left(\frac{Cmlt_{std}}{Cmlt_{avg}}\right)^2} \right) \times D_{el}$ (where E_{Del} is the error for the D of an element, Cap = concentration of element in apatite, C_{mlt} = concentration of element in melt, std = standard deviation, avg = average, D_{el} = partition coefficient of an element).

Table 3.7: Apatite/melt partition coefficients of trace elements. Left column is the partition coefficient, and the right column is the standard error. (*) Major elements based on EMPA analyses.

Run #	PC-178		PC-197		PC-224		PC-178	
Mixture	CAA		CAA		CAA		TA9	
Rb			0.032	0.015	0.015	0.006		
Cs			0.007	0.005	0.005	0.004		
Sr	0.575	0.153	0.487	0.02	0.524	0.032	1.478	0.23
La	0.658	0.312	1.063	0.102	1.166	0.066	2.891	0.43
Ce	0.709	0.275	1.087	0.248	1.267	0.042	3.234	0.437
Pr	0.812	0.278			1.642	0.115	3.434	0.491
Nd	0.945	0.299	1.624	-	1.704	0.1	3.41	0.476
Sm	1.059	0.298	1.951	0.162	1.798	0.068	3.424	0.512
Eu	0.956	0.316	0.771	0.047	0.768	0.027	3.233	0.407
Gd	1.103	0.318			1.837	0.383	3.388	0.489
Dy	1.07	0.31			1.25	0.305	2.932	0.379
Y	0.942	0.283	0.743	-	1.101	0.064	2.93	0.389
Yb	0.842	0.288	1.058	0.114	0.85	0.044	2.326	0.417
Lu	0.763	0.278	0.69	-	0.757	0.05	2.166	0.449
Ti	0.469	0.037	0.999	0.024	1.001	0.011	0.497	0.07
Hf	0.039	0.043	0.032	0.013	0.019	0.001		
Zr	0.084	0.05	0.075	0.015	0.033	0.003		
U	0.263	0.18			0.082	0.011	1.704	0.596
Th	1.075	0.275			1.26	0.307	2.565	0.629
V	0.018	0.016	0.799	0.624	0.607	0.109		
Nb			0.07	0.014	0.045	0.005		
Na*	0.183	0.449	0.435	3.014	0.326	1.401	0.04	0.277
K*	0.87	4.402	1.164	4.019	0.508	1.527	0.023	0.255
Mg*					0.237	0.78		
Al*					0.165	0.228		
Fe*	2.913	5.131			2.557	2.168	0.312	0.595
F*	1.687	8.785	2.297	5.591	2.922	9.507	2.328	27.375
Cl*	2.056	5.894	2.698	12.389	2.934	3.125	0.588	7.324

Run #	PC-179		PC-224		PC-186		PC-189	
Mixture	TA9		TA9		LS6		LS6	
Rb	0.016	0.021	0.004	0.001			0.003	0.004
Cs	0.014	0.016	0	0			0.003	0.005
Sr	0.75	0.141	0.539	0.024	0.796	0.103	0.699	0.233
La	2.081	0.388	1.003	0.142	3.601	0.312	5.269	1.625
Ce	2.395	0.45	1.166	0.158	3.492	0.203	4.607	1.202
Pr	2.832	0.436	1.359	0.18	4.38	0.238	5.651	1.385
Nd	3.173	0.482	1.576	0.215	5.107	0.379	6.538	1.635
Sm	3.52	1.017	1.802	0.254	5.257	0.444	7.861	3.104
Eu	3.011	0.946	1.636	0.219	4.866	0.428	7.267	2.975
Gd	3.25	0.311	1.85	0.265	5.392	0.528	6.806	1.601
Dy	2.929	0.31	1.58	0.254	4.298	0.386	5.312	1.35
Y	2.931	0.494	1.43	0.242	3.903	0.378	4.643	1.27
Yb	1.669	0.44	1.01	0.206	2.254	0.258	2.905	1.125
Lu	1.59	0.181	0.911	0.188	2.119	0.324	2.679	0.52
Ti	0.62	0.054	0.585	0.027	1.382	0.02	1.24	0.022
Hf	0.059	0.008	0.132	0.014			0.072	0.011
Zr	0.14	0.031	0.192	0.047			0.139	0.02
U	0.879	0.184	0.812	0.225	0.29	0.321	0.204	1.13
Th	2.629	0.328	1.75	0.521	4.998	0.575	9.29	3.782
V			0.008	0.001			1.09	
Nb	0.013	0.012	0.009	0.003			0.008	0.004
Na*	0.051	0.12	0.022	0.563	0.159	0.553	0.001	0.004
K*	0.02	0.092	0.029	1.066	0.054	0.172	0.036	0.103
Mg*			0.122	6.358				
Al*			0.003	0.15				
Fe*	0.111	0.271			0.066	0.99	0.105	0.771
F*	2.085	8.59	2.098	35.74	1.317	6.313	1.163	11.63
Cl*	1.729	2.966	1.12	18.163	0.89	2.768	1.177	2.71

Run #	PC-179		PC-196		PC-198		PC-201	
Mixture	TA6		TA6		TA6		TA6	
Rb			0.009	0.011	0.018	0.011	0.007	0.005
Cs	0.002	0.003	0.009	0.017	0.012	0.014	0.003	0.005
Sr	0.801	0.127	0.696	0.019	0.612	0.032	0.727	0.018
La	1.53	0.187	1.149	0.04	0.601	0.038	1.2	0.039
Ce	1.662	0.215	1.367	0.071	0.82	0.113	1.189	0.108
Pr	1.919	0.171	1.653	0.069	2.241	1.089	1.517	0.129
Nd	2.169	0.168	1.828	0.061	3.21	1.601	1.751	0.126
Sm	2.442	0.351	1.901	0.07	1.092	0.067	1.955	0.075
Eu	2.204	0.306	1.603	0.075	1.033	0.053	1.638	0.051
Gd	2.364	0.213	2.25	0.192	8.373	4.606	1.539	0.364
Dy	2.003	0.149	1.913	0.15	5.398	2.411	1.665	0.155
Y	1.866	0.172	1.622	0.068	1.235	0.458	1.464	0.086
Yb	1.213	0.193	1.073	0.055	0.863	0.12	1.202	0.044
Lu	1.245	0.137	1.409	0.224	0.924	0.232	1.097	0.051
Ti	0.496	0.045	0.782	0.021	0.574	0.047	0.781	0.016
Hf	0.052	0.014	0.085	0.008	0.011	0.018	0.094	0.007
Zr	0.122	0.03	0.204	0.011	0.033	0.055	0.196	0.01
U	0.866	0.184	1.907	0.325	1.377	0.47	1.893	0.142
Th	1.757	0.195	2.506	0.144	3.763	1.737	2.314	0.219
V	0.018	0.195	0.056	0.031	0.056	0.021	0.021	0.012
Nb	0.008	0.003	0.016	0.008	0.025	0.012	0.014	0.006
Na*	0.018	0.065	0.08	1.574	0.295	2.884	0.12	4.513
K*	0.027	0.524	0.053	1.583	0.16	1.771	0.05	1.092
Mg*								
Al*								
Fe*	0.486	1.299			0.717	1.799	4.003	10.877
F*	1.806	6.324	2.698	19.895	2.641	8.067	2.897	26.653
Cl*	0.883	2.706	1.825	14.867	0.669	1.116	1.624	3.321

Run #	PC-207		PC-219		PC-221		PC-222	
Mixture	TA6		TA6		TA6		TA6	
Rb	0.009	0.008	0.005	0.004	0.002	0.002	0.008	0.008
Cs	0.004	0.008	0.002	0.004	0.001	0.002	0.004	0.009
Sr	0.738	0.033	0.713	0.033	0.66	0.016	0.687	0.014
La	1.214	0.034	1.353	0.069	1.121	0.052	1.032	0.031
Ce	1.243	0.036	1.072	0.246	0.915	0.201	0.733	0.191
Pr	1.561	0.085	1.957	0.136	1.435	0.122	1.378	0.038
Nd	1.795	0.117	2.218	0.128	1.657	0.228	1.567	0.098
Sm	1.915	0.105	2.392	0.129	1.897	0.092	1.697	0.061
Eu	1.618	0.056	2.207	0.117	1.8	0.095	1.548	0.042
Gd	1.739	0.222	2.094	0.205	1.654	0.138	1.601	0.246
Dy	1.685	0.17	2.024	0.2	1.672	0.229	1.51	0.072
Y	1.373	0.048	1.568	0.112	1.376	0.096	1.25	0.072
Yb	1.085	0.049	1.2	0.059	1.071	0.07	0.985	0.044
Lu	0.971	0.041	1.103	0.069	0.978	0.071	0.916	0.054
Ti	0.842	0.037	0.737	0.053	0.701	0.032	0.761	0.02
Hf	0.082	0.013	0.086	0.009	0.058	0.005	0.077	0.012
Zr	0.154	0.016	0.195	0.019	0.129	0.012	0.162	0.012
U	1.034	0.073	0.864	0.066	0.263	0.027	1.055	0.062
Th	2.312	0.149	3.198	0.188	1.714	0.172	1.939	0.153
V	0.014	0.009	0.01	0.004	0.006	0.001	0.013	0.008
Nb	0.012	0.008	0.011	0.004	0.007	0.001	0.013	0.01
Na*	0.099	0.784	0.143	0.598	0.179	1.949	0.102	2.227
K*	0.046	0.204	0.035	0.161	0.032	1.257	0.046	0.929
Mg*			0.087	0.457	0.092	3.104	0.102	1.679
Al*			0.003	0.011	0.002	0.03	0.004	0.062
Fe*			1.028	1.561	0.761	1.146	0.613	0.519
F*	2.293	11.758	6.853	7.771	3.093	8.179	2.97	14.788
Cl*	1.306	2.65	0.087	0.137	1.273	2.21	0.999	1.726

Run #	PC-228	
Mixture	TA6	
Rb	0.001	0
Cs	0	0
Sr	0.586	0.019
La	1.335	0.057
Ce	1.317	0.086
Pr	1.684	0.074
Nd	1.951	0.12
Sm	2.295	0.119
Eu	1.998	0.087
Gd	1.926	0.18
Dy	1.986	0.147
Y	1.568	0.105
Yb	1.309	0.071
Lu	1.224	0.071
Ti	0.861	0.016
Hf	0.072	0.004
Zr	0.15	0.008
U	0.775	0.183
Th	2.068	0.281
V	0.005	0.001
Nb	0.007	0.001
Na*	0.098	1.418
K*	0.025	1.587
Mg*	0.012	0.295
Al*	0.005	0.122
Fe*		
F*	4.049	13.359
Cl*	4.146	3.086

3.2.4 Henry's Law

Henry's law behaviour was observed to be obeyed in doped and undoped runs as the partition coefficients is independent of the element concentration. Figure 3.17 shows that for all experimental runs an increase in element concentration does not significantly affect the partition coefficient with all variations being within the uncertainties.

3.2.5 Achievement of equilibrium

Use of undoped and doped mixtures with Durango apatites allowed for the use of forward and reverse paths to reach equilibrium. In undoped runs, Durango apatite has higher initial concentrations of all trace elements relative to the melt and trace elements are diffusing into the melt. On the contrary, the doped runs have the concentration of the ten elements much higher in the melt compared to the Durango apatite so that these elements were diffusing into the apatite. Figure 3.16 and Figure 3.17 A shows that both doped and undoped runs produce a similar partitioning pattern indicating that our runs reached equilibrium concentrations. We also tested the achievement of equilibrium by comparing the products of 24 hour with 48 hour runs. Both 24- and 48-hour experiments produce the same partitioning coefficients (where slope =1) (Figure 3.17 B) indicating that equilibrium has been reached in 24 hour runs.

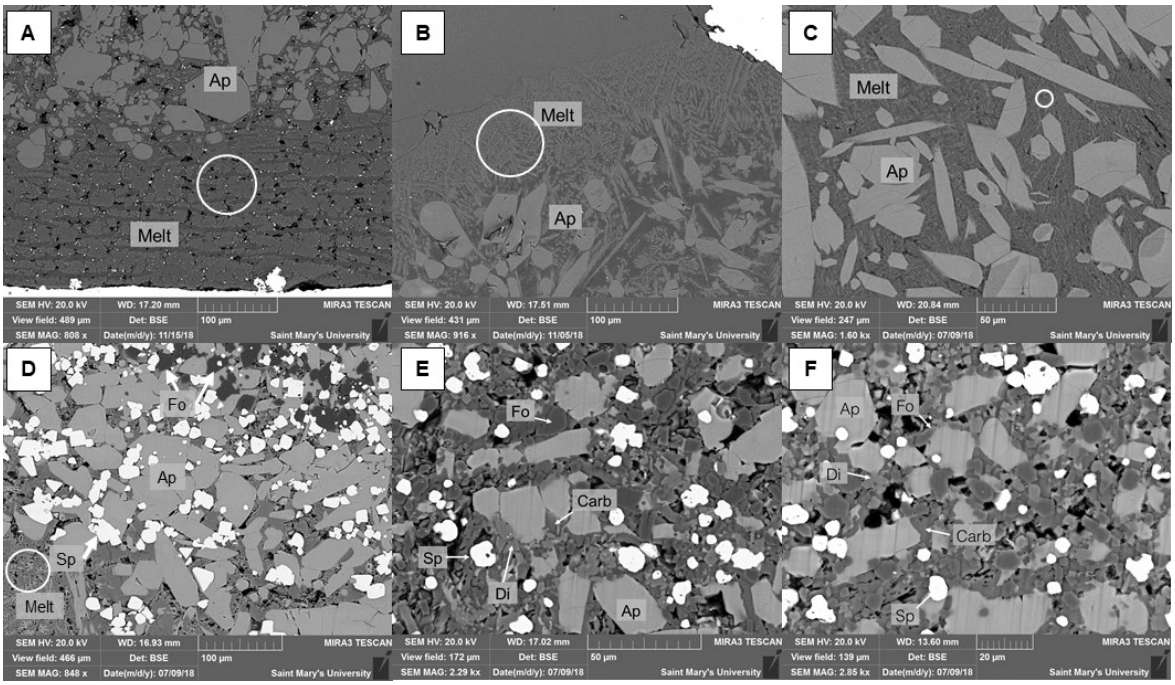

Figure 3.9: BSE images of the experimental run products. (A) run PC-197 (CAA, SA) shows concentration of apatite towards the top of the capsule and segregation of melt with skeletal quench apatite and sparks of tiny REE-minerals towards the bottom. (B) run PC-196 (TA6, DA & SA) shows separation of apatite crystals and the melt with quench skeletal apatite. (C) run PC-179 (TA9, DA) shows apatite crystals surrounded by the quenched melt. Note the presence of compositional rim and core in some apatites. (D, E, F) run PC-186 (with DA) showing melt pockets in LS6 composition (D) and the lack of any quenched melts in LS15 (E) and LS26 (F). White circles show representative areas used in EMP analysis of the melts. Ap=apatite, Di=diopside, Fo=forsterite, Sp=spinel, Carb=carbonate, DA=Durango apatite, SA =synthetic apatite.

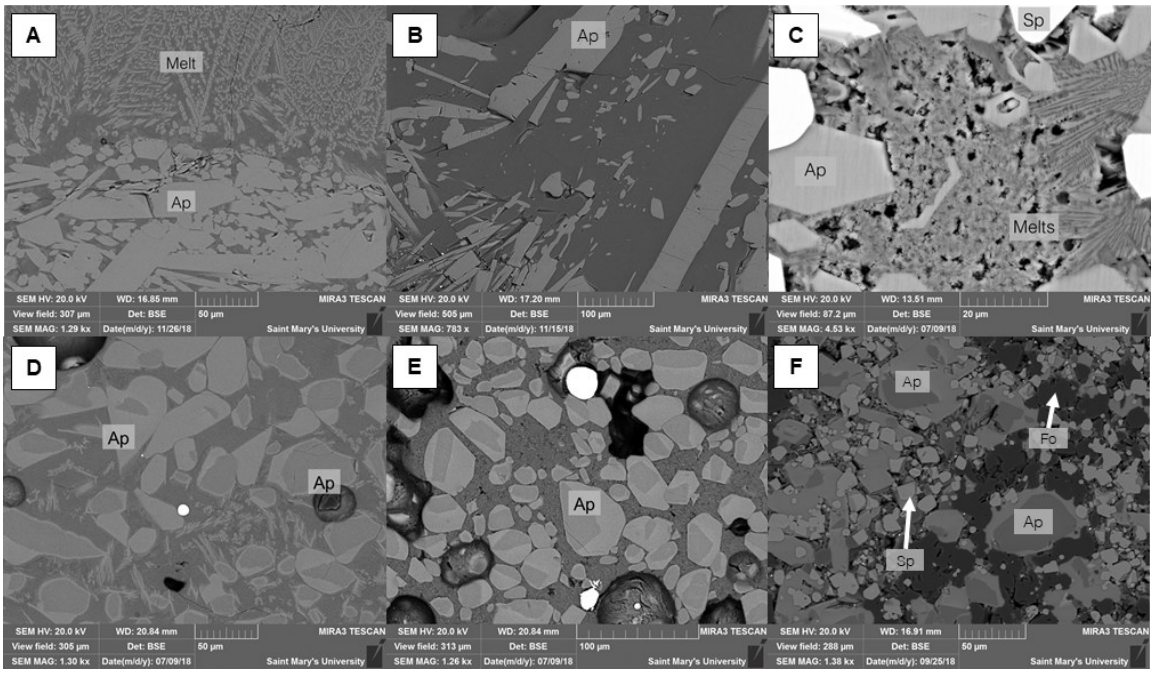

Figure 3.10: BSE images of (A – C) apatite textures in the runs not doped with trace elements and (D - F) compositional zoning showing trace-element enrichment in apatite rims in the runs doped with trace elements with Durango apatite. (A) Euhedral prisms of liquidus apatite and fine skeletal apatite in quenched melt in PC-201 with TA6 and SA. (B) Large euhedral lathes of apatite in PC-197 with CAA and SA. (C) Euhedral apatite prisms and skeletal quench apatites in the melt in PC-186 with LS6 and DA. (D) Compositional zoning in PC-179 with TA6. (E) Zoning in PC-179 with TA9. (F) Zoning in PC-189 with LS6.

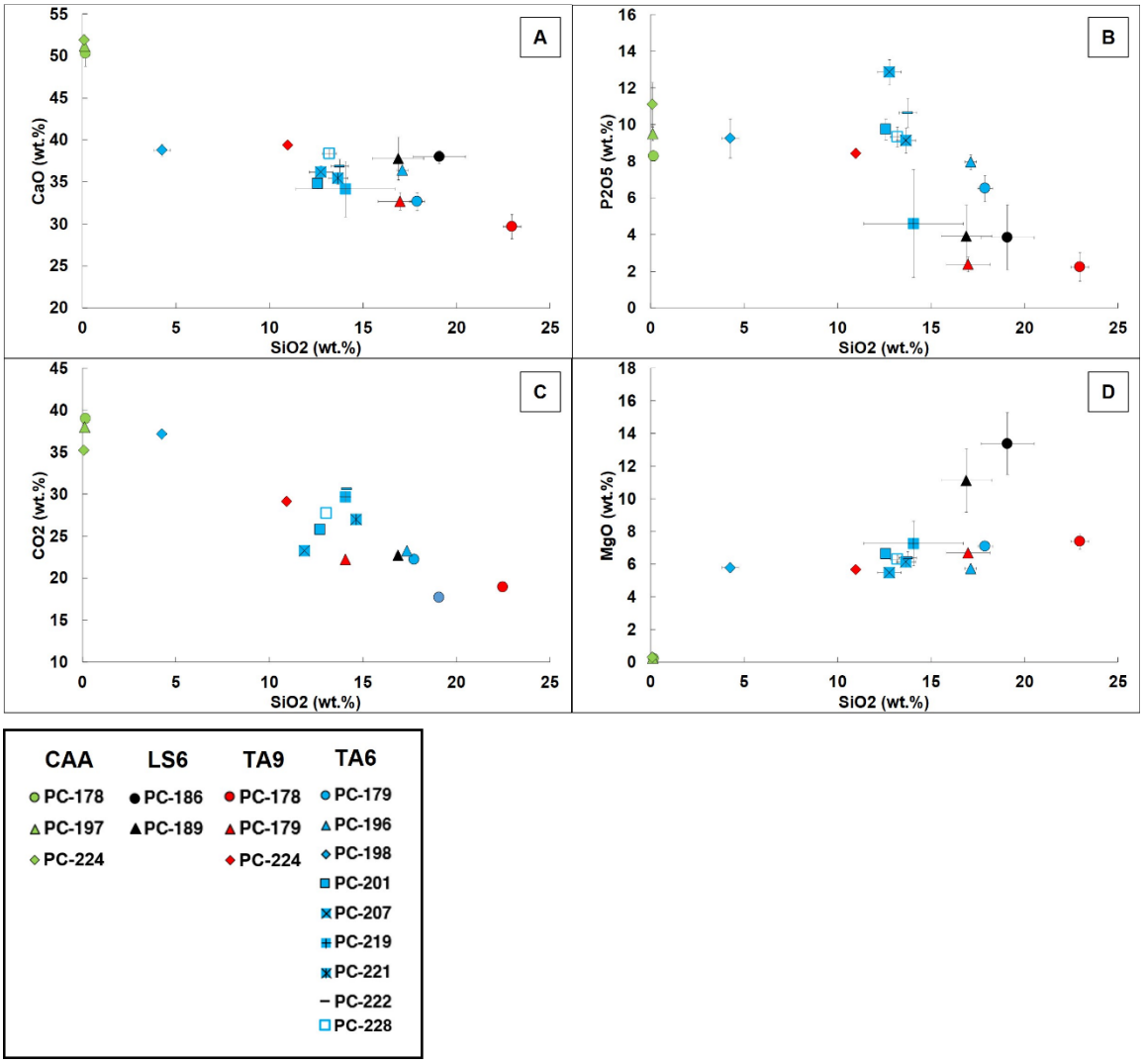

Figure 3.11: Composition of quenched melts in the experiments from EMPA. CO_2 content was calculated as a difference between the total in EMP analyses and 100%.

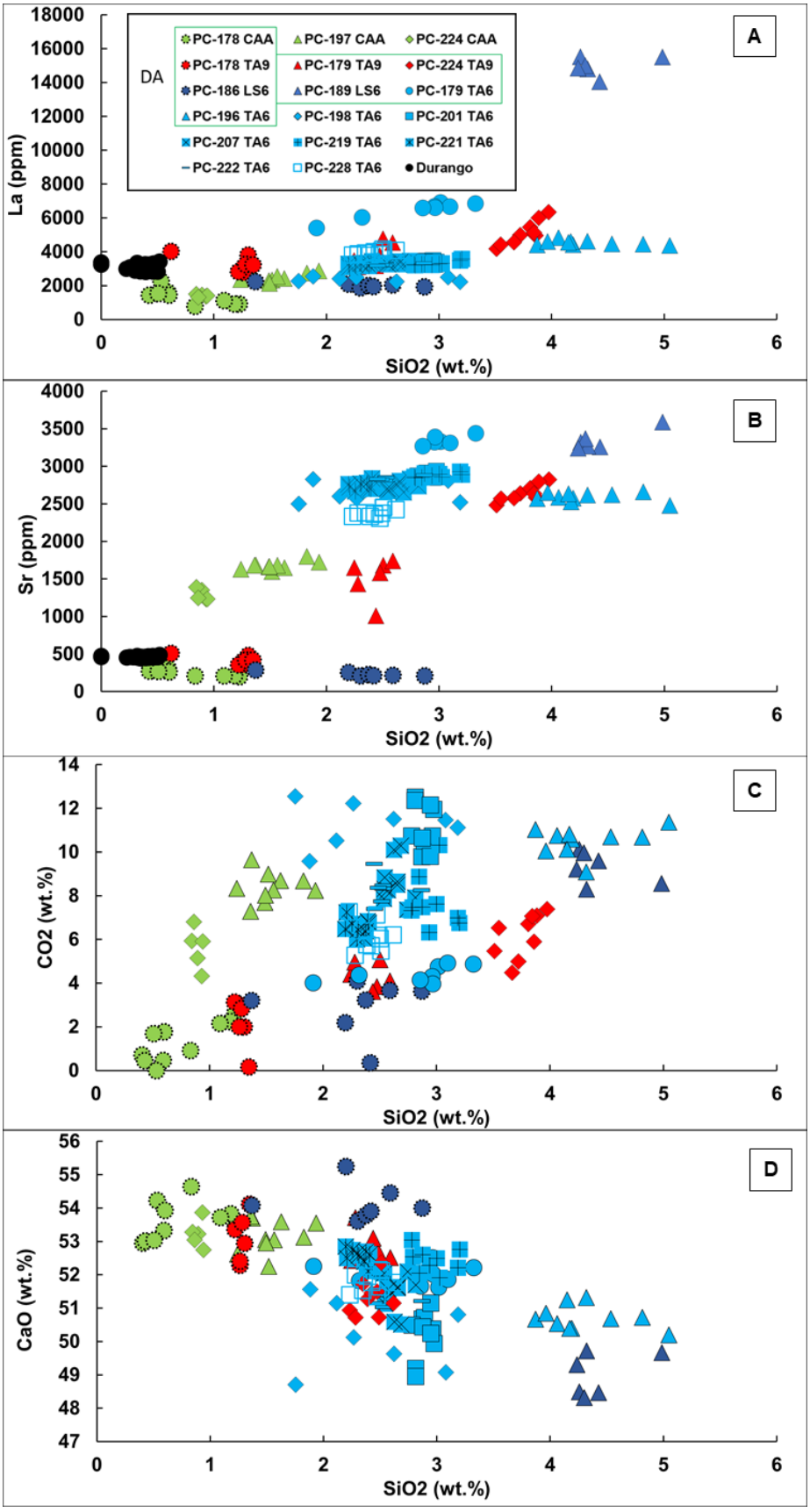
A
DA
PC-178 CAA
PC-197 CAA
PC-224 CAA
PC-178 TA9
PC-179 TA9
PC-224 TA9
PC-186 LS6
PC-189 LS6
PC-179 TA6
PC-196 TA6
PC-198 TA6
PC-201 TA6
PC-207 TA6
PC-219 TA6
PC-221 TA6
PC-222 TA6
PC-228 TA6
Durango
La (ppm)
SiO2 (wt.%)
B
Sr (ppm)
SiO2 (wt.%)
C
CO2 (wt.%)
SiO2 (wt.%)
D
CaO (wt.%)
SiO2 (wt.%)

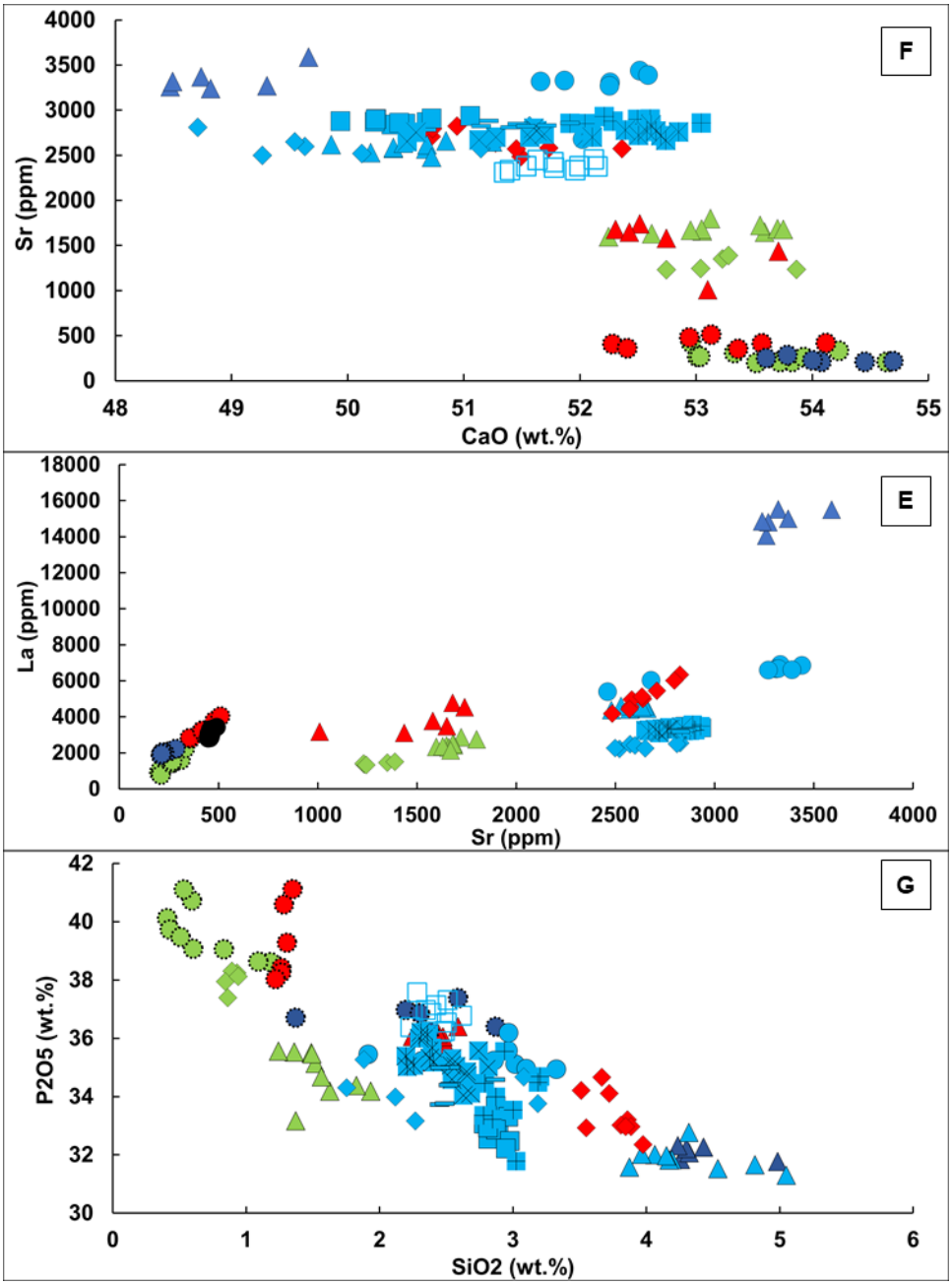

Figure 3.12: Composition of apatite in the experimental runs. SiO_2 (wt.%), La (ppm) and Sr (ppm) are from LA-ICP-MS analyses, CaO (wt.%) is from EMPA, and CO_2 (wt.%) is calculated as a difference between the total in EMP analyses and 100%. Composition of Durango apatite from LA-ICP-MS analyses is shown for comparison. Runs with no trace element added are shown as symbols with dotted outline.

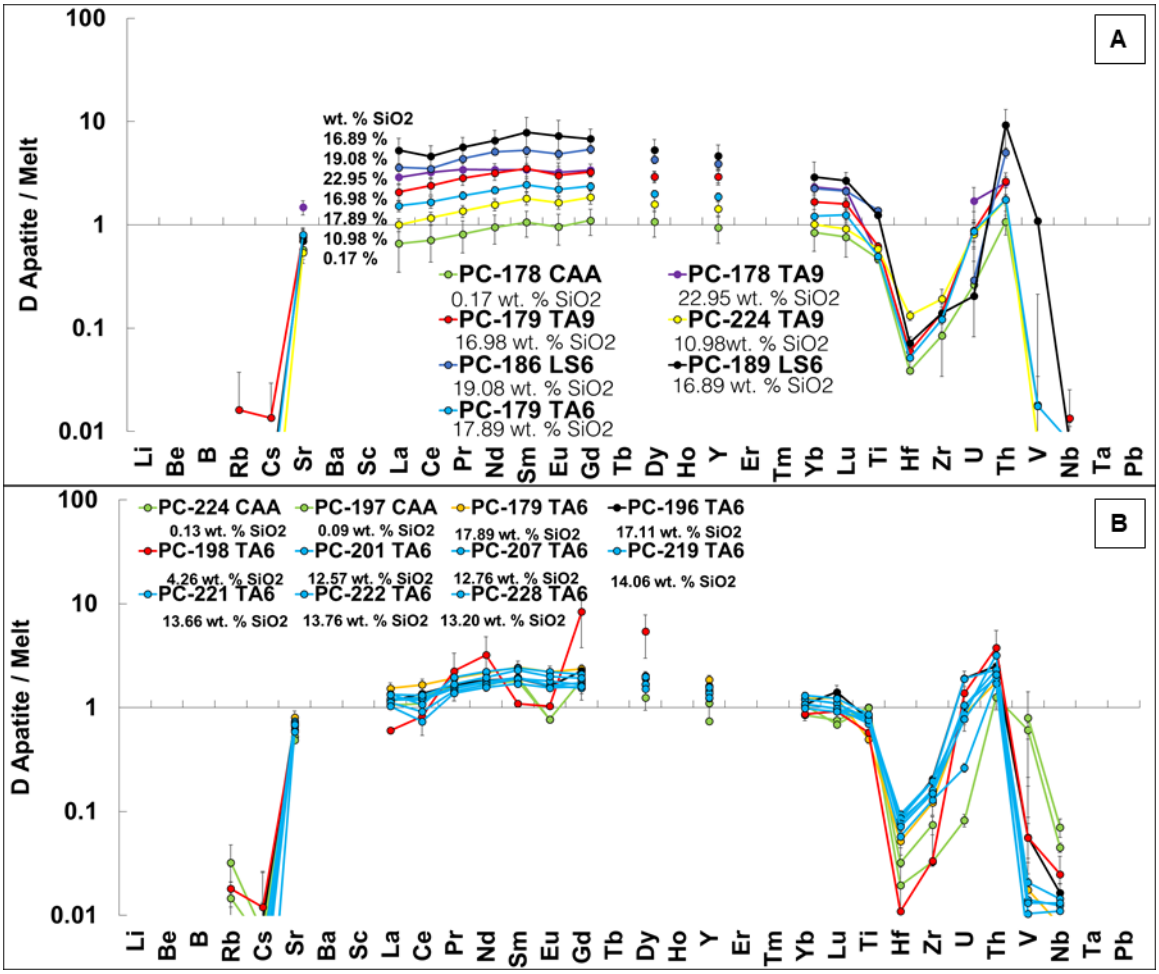

Figure 3.13: The effect of different factors on partition coefficients of trace elements between apatite and melts. The effect of melt composition in runs with Durango apatite (**A**) and with synthetic apatite (**B**); PC-178 and PC-186 are undoped runs; the content of SiO_2 wt. % of the melt is shown for each run.

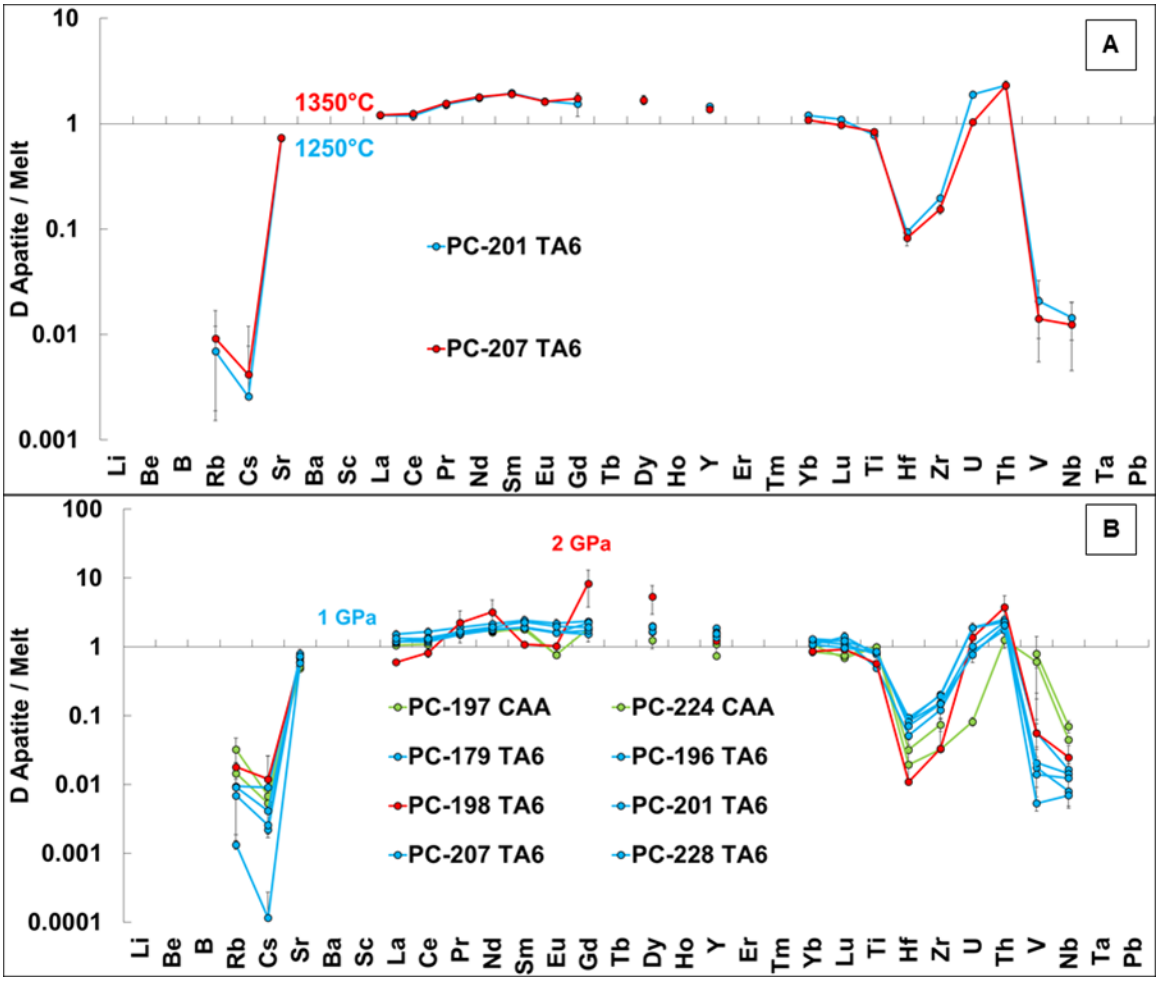

Figure 3.14: The effect of different factors on partition coefficients of trace elements between apatite and melts. **A**) Shows no effect of temperature. **B**) The effect of pressure. TA6 composition at 2 GPa (run PC-198) formed a melt with only 4.26 wt. % SiO2 and D close to that for CAA mixtures. Other runs with TA6 at 1 GPa and SiO2 (12-57-17.89 wt. % SiO2 are shown for comparison.

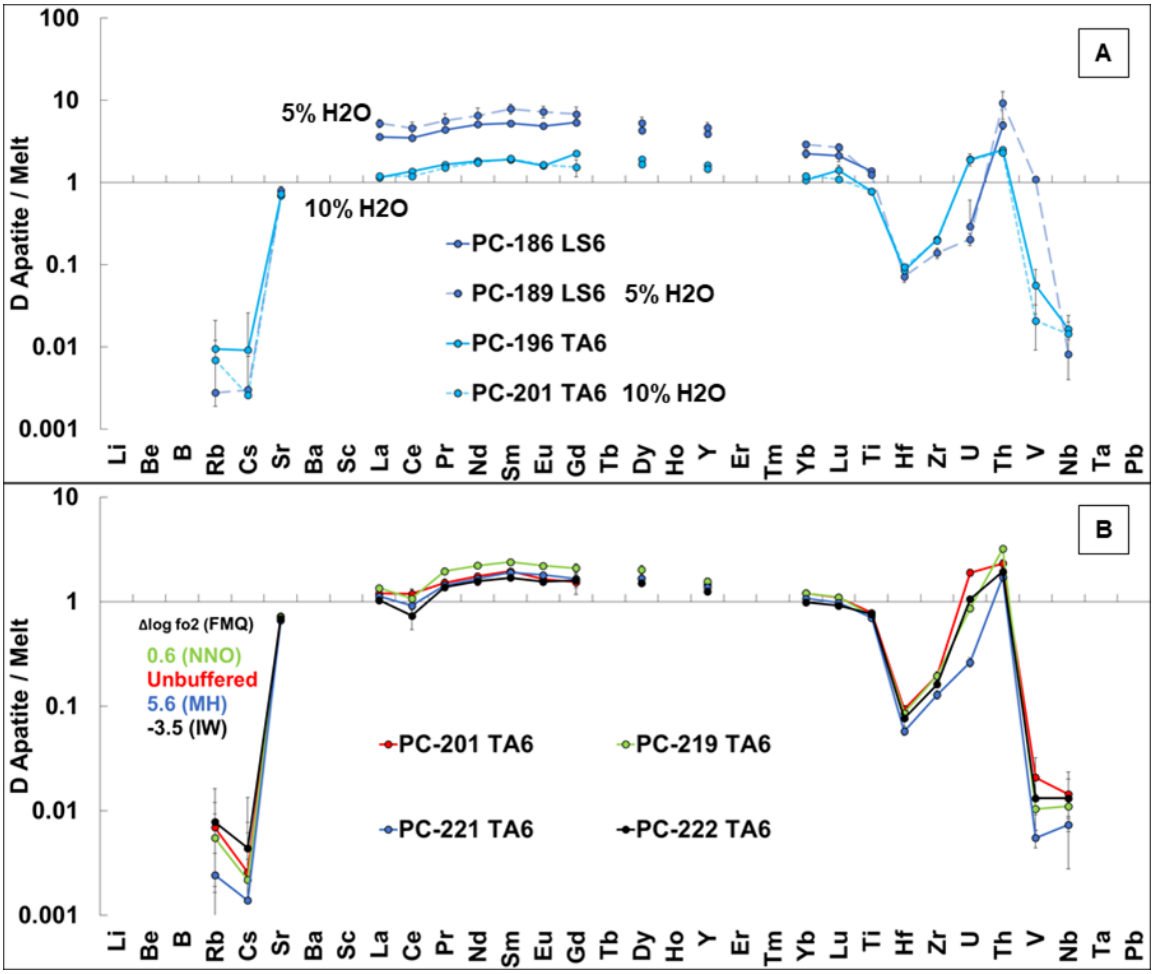

Figure 3.15: The effect of different factors on partition coefficients of trace elements between apatite and melts. **A**) Shows no effect of H_2O (5 and 10 wt%) for TA6 (PC196 and PC201) and LS6 (PC186 and PC189) compositions. Solid lines represent anhydrous runs and dotted lines represent hydrous runs. B) Shows no effect of oxygen fugacity.

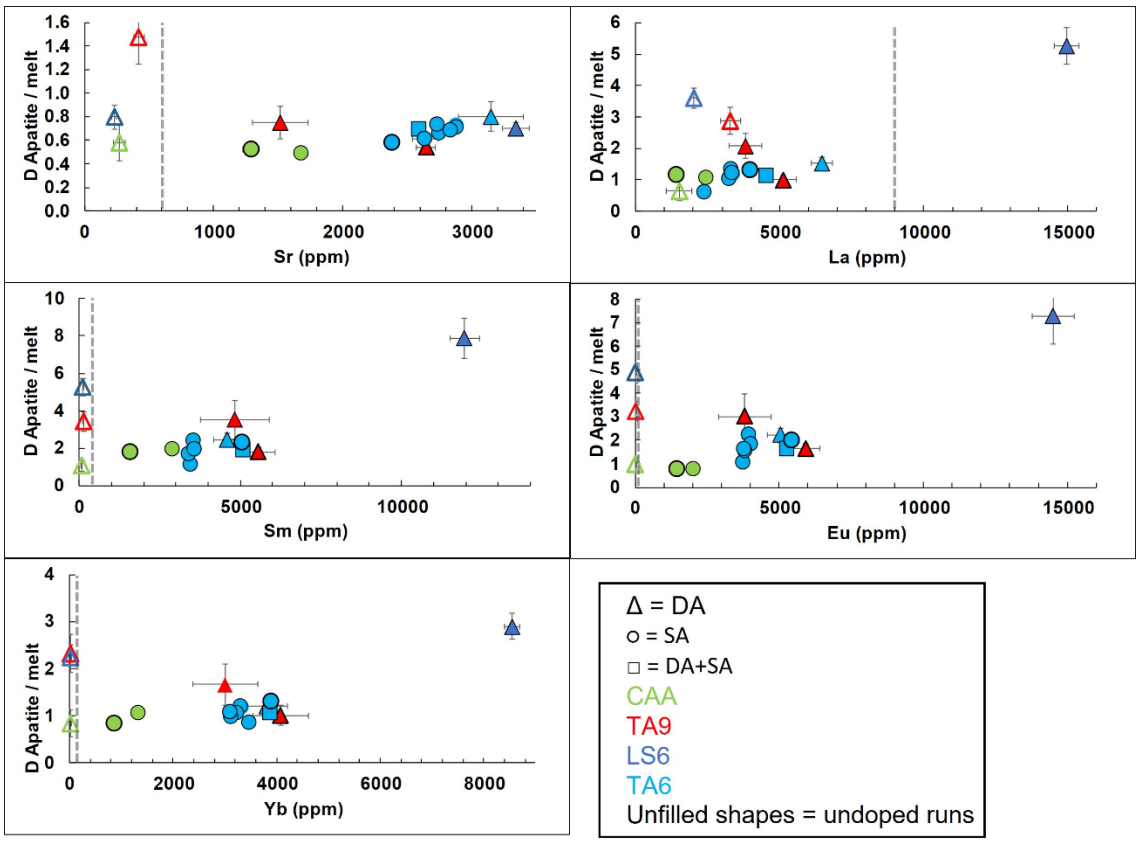

Figure 3.16 - The relationship between the element concentrations in apatite and the estimated partition coefficients (D) for experiments with different starting compositions and experimental parameters showing that our data obeys Henry's Law where the partition coefficients is independent of the element concentration. Experimental runs with different melt compositions and types of apatites are also shown. Partition coefficient error bars calculated as the propagated error in the quotient of two variables (concentration in apatite and melt). Concentration error bars calculated as 2 standard deviations (2σ). Error bars in some cases are smaller than the symbol. The high D_{REE} in the doped run with LS6 is within the uncertainties relative to D_{REE} in undoped LS6 run. *Dashed lines represent upper concentration range observed in kimberlitic apatites from Ekati and Snap Lake Mine except for Sr which is the lower concentration limit, Sr extends to an upper range limit of 28000 ppm (data from (Milligan, 2017)).

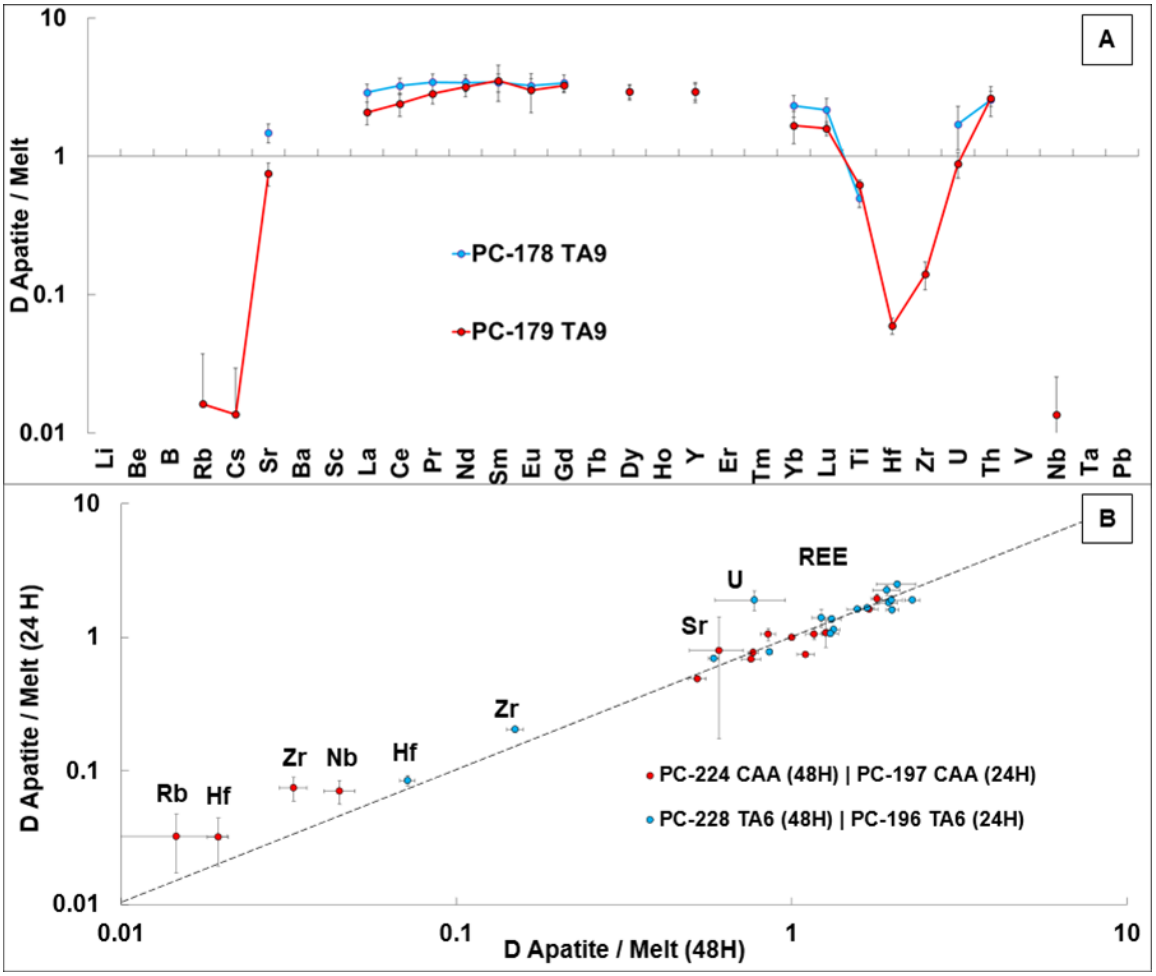

Figure 3.17: The effect of different factors on partition coefficients of trace elements between apatite and melts. **A**) Comparison of D in forward doped run with DA and reverse undoped run indicating achieving of the equilibrium for most or all the elements. **B**) Di from 24H runs vs. Di from 48H runs. Shows no effect of the run duration.

Chapter 4 Discussion

4.1 Comparison to the previous estimates of apatite / melt partition coefficients

Previous estimates of element partitioning in apatite have been focused primarily on silicate and carbonatite melt compositions. This study aims to provide estimates using low-SiO_2 melts analogous to kimberlitic melts and to investigate discrepancies seen in previous carbonatite experiments. Studies of silicate melts ranging from basanite to granite at 7.5 kbar and 950-1120°C (Watson and Green, 1981) and basalt to andesite at 1 GPa and 1250°C (Prowatke and Klemme, 2006) showed increasing compatibility of REEs in apatite with increasing SiO_2 melt content. These studies found REEs along with Y and Sr to be compatible, LILE to be strongly incompatible, MREE were found to be more compatible than LREE and HREE, and Sr compatibility was found to be independent of melt composition and temperature. Watson and Green (1981) also concluded that a decrease of 130°C in temperature contributed to an increase in partition coefficient by a factor of 2 in silicic melts of 40-80 wt. % SiO_2. However, the studied compositions had SiO_2 well above that suggested for kimberlites. Partitioning behaviour of trace elements between apatite and carbonate melts have been explored using both natural samples (Guzmics et al., 2008) and experimental studies (Klemme and Dalpe, 2003, Hammouda et al., 2010). Hammouda et al. (2010) also established that D_{REE} <1 depends on the SiO_2 content of apatite. In contrast to these two studies, Klemme and Dalpe (2003) found that all REE were incompatible in apatite.

This study shows significant effect of melt composition on REE partition coefficients in apatite for low-SiO_2 kimberlitic melt (Figure 4.1), which has D_{REE} similar to those from experiments with basalt. The effect of SiO_2 is especially notable in our experiments with

Durango apatite (Figure 3.13 A; Figure 4.2). In the runs with synthetic apatite this effect is less clear. Experiments with SA only produced analyzable apatite for CAA and TA6 compositions. Runs with TA6 and SA which produced melt with SiO_2 content ~12.57-17.11 wt. % show similar Ds to the run with TA6 and DA (17.89 wt. % SiO_2) (Figure 3.13 A). Partitioning of trace elements in the run with SA and CAA is similar to partitioning in the run with DA and CAA for some elements, whereas other elements show higher compatibility (Figure 3.13 B).

Our experiments with a carbonate melt produced lower D_{REE} than in Hammouda et. al (2010) (D = 1.3-3.17) and Guzmics et al. (2008) but higher than Klemme and Dalpe (2003) (D = 0.34-0.49) (Figure 3.13 A B; Figure 4.1). We observed difference in the behavior of LREE and HREE between runs with DA and SA. For REE between La and Sm D = 0.69-1.95 in the run with SA and but lower in the two runs with Durango apatite (D = 0.66-1.10), whereas HREE show similar D<1 in the three runs. Behaviour of LREE and MREE in our experiments is similar to the results of Hammouda et. al (2010) and Guzmics et al. (2008).

There are a few possible causes for the discrepancies in REE compatibility between D_{REE} estimated for carbonate melts in the previous and this study (see Table 4.1 for the summary). Here I attempt to explain them using differences in the melt and apatite composition. Since Hammouda et al. (2010) used melt of natural calcite (2.46-2.56 wt.% SiO_2) with Durango and In Ouzzal fluorapatite (5.12 wt.% SiO_2, 2.52 wt. % SO_2) while Klemme and Dalpe (2003) used mixtures of synthetic $CaCO_3$ with synthetic apatite, the presence of other elements such as sulfur and SiO_2 may have increased the compatibility

of REE in Hammouda et al. (2010) by providing additional substitution mechanism 2 and possibly 1:

$$REE^{3+} + SiO_4^{4-} = Ca^{2+} + PO_4^{3-}$$

$$REE^{3+} + Na^{+} = 2\ Ca^{2+}$$

Similarly, the study by Guzmics et al. (2008) calculated D using Mg-rich carbonatite melt inclusions which included: SiO_2 poor (7.35 wt.% SiO_2), SiO_2 bearing (26.08 wt.% SiO_2), and sulfate-bearing (9.62 wt.% SO_3; 4.26 wt.% SiO_2) inclusions. SO_3 and MgO in the melt correlate with higher D_{REE} (Figure 4.2, 4.3) providing additional mechanism 4:

$$REE^{3+} + S^{2-} = Ca^{2+} + F^{-}.$$

The type of apatite may also be responsible for different D_{REE}. Hammouda et al. (2010) observed lower D_{REE} in their run with Durango apatite than in the runs with In Ouzzal apatite. Our results also showed that Durango apatite yielded a lower compatibility than synthetic hydroxyapatite runs. While Klemme and Dalpe (2003) show similar incompatible behaviour for the three varieties of synthetic apatite (-Cl, -F, and -OH), their simplified composition does not provide any elements to support REE substitution using mechanisms 1, 2, and 4. Run temperature and pressure used in our experiments are identical to Klemme and Dalpe (2003) but produces differing compatibility behaviour. It is agreed upon that pressure and temperature does not have a significant effect on compatibility behaviour (Hammouda et al. 2010; Watson and Green, 1981). This is also supported by our results (Figure 3.14 D; Figure 3.15 E).

Table 4.1: Summary of the differences and similarities between apatite/melt partitioning studies based on carbonatitic melt compositions.

Study	This Study	Klemme and Dalpe (2003)	Hammouda et al. (2010)	Guzmics et. al. (2008)
T and P	1 GPa at 1250°C	1 GPa at 1250°C	6 GPa at 1350-1380°C	2.2-3.8 GPa at 1120°C
Apatite	Durango (fluorapatite) and synthetic apatite (hydroxylapatite)	Synthetic chlorapatite, hydroxylapatite, fluorapatite	In Ouzzal (fluorapatite) – rich in S, SiO_2, Sr, LREE Durango (fluorapatite)	Natural apatite (unspecified halogen).
Starting Mixture	$CaCO_3$	$CaCO_3$	Natural calcite (melt with 2.46-2.56 wt.% SiO_2)	Apatite hosted carbonatite melt inclusions (S-rich, Si-rich, Si-poor) Mg-rich
D_{REE}	Less compatible in Durango than in synthetic	Mostly incompatible	In Ouzzal mostly compatible Durango is imcompatible with REE	Compatible but slightly less compatible than Hammouda et al. (2010)

Hammouda et al. (2010) suggested that D apatite/carbonatite melts is mostly controlled by SiO_2 content of apatite, whereas Klemme and Dalpe (2003) suggest that the main control is the silica content of the melt. Our data confirms higher apatite D_{REE} in natural SiO_2-bearing systems and shows that the SiO_2 content in the melt has the strongest effect on the compatibility of REE in apatite (Figure 4.2) in agreement with Klemme and Dalpe (2003). We observed no clear correlation of SiO_2 content of apatite with D_{REE} (Figure 4.3). However, our apatite have much lower SiO_2 content (<1.45 wt. %) than apatites in Hammouda et al.'s (2010) with 3.5-5 wt. % SiO_2. We also observed a minor positive correlation of MgO and SO_3 with D.

Our data and most previous studies show that Rb, Cs, Ba, Hf, Zr, and Nb are incompatible in apatite for all melt compositions (except for the compatible behaviour of Rb, Ba, Hf,

and Zr in Hammouda et. al., 2010), whereas compatibility of Sr is not significantly affected by the melt composition. The slightly more compatible behaviour of MREE (Sm, Eu, Gd) relative to LREE (La, Ce, Pr) and HREE (Yb, Lu) in this study agrees with other studies (Watson and Green, 1981; Klemme and Dalpe, 2003; Prowatke and Klemme, 2006; Guzmics et. al, 2008). Given that D_{Sr} remains relatively constant in different melt compositions, ratio of LREE/Sr could be used to examine the composition of kimberlite melt during crystallization of apatite. We would expect to see higher LREE/Sr in apatites from a more silica-rich kimberlite than in a silica-poorer kimberlite.

In summary, the experimentally determined partition coefficients between apatite and kimberlite-like melts are lower than in mafic to felsic silicate melts. Partition coefficients in carbonate melts depend on the type of apatite, where Durango fluor-apatite shows lower compatibility than synthetic hydroxyl-apatite. Use of pure synthetic vs. natural apatite in previous experimental studies with carbonate melts can be the reason of the discrepancy in their reported Ds as elements like Si, Na, S provide additional substitution mechanisms. SiO_2 and SO_3 content in the melt show the strongest control on the D's. SiO_2 content of melt has a greater effect on D than SiO_2 apatite content. SO_3 content in melt and apatite has an equally significant effect of D_{REE}.

4.1.1 Comparison to Partition Coefficient in Immiscible Melts

I compare partition behaviour of trace elements in carbonate and silicate melts in this study to partition coefficients between immiscible carbonatite and silicate melts (Martin et al., 2013). The study by Martin et al. (2013) shows that REE favours carbonatite melts and an increase in the silica content of the silicate melt significantly increases D_{REE} into the

carbonatite melt. This is due to the increased polymerization of the silicate melt. This is similar to our experiments where D_{REE} increases for apatite as the silica content of the melt increases. This is demonstrated by calculating $D_X{}^{carbonate/silicate} = \frac{D_X{}^{Ap/Silcate\ melt}}{D_X{}^{Ap/Carbonate\ melt}}$ (where X = trace element) and comparing the obtained $D_X{}^{carbonate/silicate}$ to those obtained for immiscible melts by Martin et al (2013). Figure 4.4 illustrates a good agreement of our obtained partition coefficients for CAA and TA6 melts and those from Martin et al.'s (2013) study for silica-undersaturated melts.

4.2 Substitution mechanisms

REE and other trace elements preferentially substitute into one of the two Ca sites in apatite. LREE favour substitution into the Ca1 site, while HREE prefer the Ca2 site. MREE have no preference to either Ca sites and substitute equally in both (Chakhmouradian et al., 2017). Figure 4.5 examines the three main substitution mechanisms (Pan and Fleet, 2002) for the incorporation of REE into apatite (Rønsbo, 1989):

$$REE^{3+} + Na^{+} = 2\ Ca^{2+} \quad (1)$$

$$REE^{3+} + SiO_4^{4-} = Ca^{2+} + PO_4^{3-} \quad (2)$$

$$2\ REE^{3+} + [v] = 3\ Ca^{2+} \quad (3)$$

and shows that substitution mechanism in apatite in our study depends on the type of apatite (Durango vs. synthetic) rather than melt composition. REE partitioning in Durango apatites (fluorapatite) uses a mix of mechanisms (2) and (3), whereas synthetic apatite (hydroxylapatite) shows a mix of mechanisms (1) and (3) (Figure 4.5 A). This is opposite to the experiments by Fleet et. al (2000b), which demonstrated that REE substitution in hydroxylapatite is preferentially through mechanism (2) while fluorapatite is a combination

of mechanism (1) and (2). Although synthetic apatite incorporates REE with a contribution of Na^+ mechanism (1) (Figure 4.5), Figure 4.2 shows no notable correlation between Na melt content and D_{REE}. However, the correlation is more prominent in the Na content uptake by SA as compared DA (Figure 4.6A). It is also possible Na^+ is being substituted by another monovalent cation which was not analyzed for such as Li^+ (Pan and Fleet 2002). The incorporation of REE in Durango apatite via SiO_4^{4-} mechanism (2) is in agreement with the positive correlation between SiO_2 content of the melt and D_{REE} (Figure 4.2). This difference in the preferred substitution mechanism for SA and DA may explain the discrepancy in $D_{LREE}^{Ap/carb}$ between our runs with SA and DA and the same carbonate melt. Since DA favours more so the SiO_4^{4-} mechanism (2), the Si-poor carbonate melt results in lower D_{REE}. In addition, preferential uptake by Ca1 site of LREE with larger radius would also suggest that Na is preferred on the same site. Since substitution in synthetic apatite is mostly controlled by mechanism Na^+ (1), it will mostly affect the Ca1 site and promote LREE uptake by apatite. Table 3.5 and Figure 4.6A shows higher Na^+ uptake in SA despite similar Na_2O content in all the carbonate melts, along with higher D_{REE} as a result of mechanism (1). However, the uptake of Si is still prominent in both SA and DA suggesting there is still a combination of substitution mechanisms (Figure 4.6B).

Another possible substitution mechanism for REE is the vacancy mechanism (3). The observed low totals in apatite analyses of SA doped with trace elements may be due to carbonate component and/or vacancy. To examine the case where it is a vacancy mechanism, the apfu of Si + P was divided by the ideal apfu of 3 to calculate the percent proportion and multiplied the sum of apfu of cations. The difference from the ideal apfu of 5 represents the vacancy apfu. Figure 4.6C shows a slight positive correlation between REE

content and the stoichiometric vacancy calculated. In summary, the main substitution mechanisms we observe in our experiments are mechanisms (1) and (3) for synthetic apatite, and mechanism (2) for Durango apatite.

Other possible substitution mechanisms include 1) mechanism (4) based on sulfur anions and 2) mechanisms based on CO_3^{2-} substituting for PO_4^{3-}. Indeed, SO_3 melt content shows a slight positive correlation with D_{REE} (Figure 4.2). However, this correlation is not strong since sulfur was not added in appreciable amounts in our experiments and S uptake compared with REE in apatite does not show a significant positive correlation (Figure 4.6D). Possible presence of CO_3 is indicated by low totals only present in doped runs. However, this would require further confirmation. Synthetic apatites have been shown to contain up to 16.65 wt.% CO_3 (Pasteris et al., 2012). The incorporation of carbonate into apatite is made possible by two main types of replacement. Type A involves the direct substitution of CO_3^{2-} for OH^-, where two hydroxyl sites are left vacant (Pasteris et al., 2012):

$$CO_3^{2-} + [v] = 2\ OH^- \quad (5)$$

The more dominant and common, type B, refers to the substitution of the PO_4^{3-} group for CO_3^{2-} as outlined by the following substitution mechanisms possible (Fleet and Pan, 2002):

$$CO_3OH^{3-} = PO_4^{3-} \quad (6)$$

$$CO_3F^{3-} = PO_4^{3-} \quad (7)$$

$$2\ CO_3^{2-} + [v] = 2\ PO_4^{3-} + Ca^{2+} \quad (8)$$

$$CO_3^{2-} + SiO_4^{4-} = 2\ PO_4^{3-} \quad (9)$$

$$CO_3^{2-} + Na^+ = PO_4^{3-} + Ca^{2+} \quad (10)$$

$$CO_3^{2-} + H_3O^+ = PO_4^{3-} + Ca^{2+} \quad (11)$$

Difficulties associated with the measurement of non-stoichiometry of apatite in EMPA such as the presence of H and the lack of C or O measurements, can make determination of CO_3 difficult without structural or spectroscopic studies (Chakhmouradian et al., 2017). Thus, the assumption is made here that low totals is equal to the CO_2 content. The most probable mechanisms for the incorporation of CO_3 in our experimental apatites is mechanisms (8), (9), and (10). This could be associated with the negative correlation between PO_3 and CaO content in apatite and the presumed CO_3 content (Figure ES 8). There is also a weak positive correlation between Na_2O and the CO_3 content. Type A substitution is unlikely as there is no inverse correlation between OH and the presumed CO_3 content.

Comparison to the substitution mechanisms in natural kimberlitic apatites from Leslie, Panda, Grizzly and Snap Lake kimberlites (Milligan, 2017) shows that the majority of Leslie and Snap Lake apatites follow a -1/2 slope (Na^+ mechanism 1), with the more OH-rich apatite from Panda plotting along slope -3/4 (vacancy mechanism 3) (Figure 4.5 B). This may be related to the medium from which the apatites crystallized from. Snap Lake apatites likely crystallized from a fluid and shows that a Na^+ substitution is favoured. Whereas apatites from Panda crystallized from a melt and favours a SiO_4^{4-} mechanism (Milligan, 2017). Based on our experimental results, there is no clear conclusion on whether our specific low-Si melt compositions have any influence on the preference of a particular substitution mechanism but rather a combination of them.

4.3 Apatite solubility

Numerous studies have confirmed that apatite saturation depends on melt composition, temperature, and pressure. Experiments on silicate melts demonstrated that apatite solubility decreases when SiO_2 melt content increases and when temperature decreases (Figure 4.7 C) (Green and Watson, 1982). The effect of pressure on apatite saturation is minor (Green and Watson, 1982; Tollari et al., 2008) and varies with SiO_2 melt content. When the SiO_2 content is >50 wt. %, apatite solubility slightly decreases with increasing pressure, whereas when SiO_2 is <45 wt.%, the effect of pressure is reversed and apatite solubility increases with increasing pressure (Green and Watson, 1982). Water was found to have a minimal effect on P_2O_5 saturation limit where there is a slight increase in apatite solubility with decreasing water content (Green and Watson, 1982). Tollari et al. (2008) also concluded that SiO_2 and CaO content of the melt have the most significant effect on apatite saturation in their silicate melt experiments. CaO was found to have a positive correlation with P_2O_5 content of apatite-saturated melt whilst SiO_2 had a negative correlation – as was with the findings by Green and Watson (1982). The addition of fluorine was found to lower the P_2O_5 content required for apatite saturation (Tollari et al., 2008). Tollari et al. (2008) specify that for melts with approximately 55 wt. % SiO_2, P_2O_5 would attain saturation in the melt at 1.5 wt.% in a fluorine free melt compared to 0.6 wt.% P_2O_5 in a fluorine bearing one.

Compared to silicate melts, carbonate melts, where SiO_2 content is much lower (1.5-9.9 wt. %), were found to be able to dissolve high amounts of P_2O_5 (up to 24 wt. %) (Baker and Wyllie, 1992; Ryabchikov and Hamilton, 1993; Ryabchikov et al., 1993) (Figure 4.7 A). While not directly comparable to calcitic melts, these studies which used phosphate-

carbonate peridotite systems still demonstrate the considerable amount of P_2O_5 that can be in a carbonate melt. In natural and synthetic calcite systems, P_2O_5 content is within 3.39-11.09 wt. % (This study; Hammouda et. al, 2010; Klemme and Dalpe, 2003; Guzmics et. al, 2008). Baker and Wyllie (1992) report a positive correlation between CaO and P_2O_5 similarly to silicate melts, and no effect of alkaline content on apatite solubility (Figure 4.7 B). Additionally, CO_2 has been found to have a negative correlation with P_2O_5 due to the ability of P_2O_5 to depress the solubility of CO_2 in carbonate and Na-SiO_2 melts (Figure 4.7 D) (Baker and Wyllie, 1992). In contrast to the other studies, Hammouda et. al (2010) suggests instead that apatite solubility in a carbonatite melt is inversely related to CaO melt content. In summary, the major controls on apatite saturation in both silicate and carbonate melt systems are SiO_2, CaO, P_2O_5, CO_2 melt content, and temperature, where an increase in SiO_2 and CO_2, decrease in CaO and temperature can trigger crystallization of apatite.

The low-SiO_2 kimberlite-like melts of this study, in agreement with the trends observed in the previous studies, also show that higher SiO_2, higher CO_2 and lower CaO increases apatite saturation (Figure 4.7 A B). P_2O_5 solubility is lower in our study than in Baker and Wyllie, 1992; Ryabchikov and Hamilton, 1993; Ryabchikov et al., 1993 but is similar to Hammouda et al. (2010) and Klemme and Dalpe (2003) which use similar simple carbonate compositions (Figure 4.7 B). Hammouda et al. (2010) suggested that the reason might be the more dolomitic composition of the carbonatite melts equilibrated with mantle-like melts which have lowered Ca activity and thus more P can be contained in the melt prior to reaching apatite saturation. The coexistence of apatite and melt depends on the activities of the dissolved apatite components (Harrison and Watson, 1984).

When applying to kimberlites, in addition to apatite crystallization due to magma cooling, presence of euhedral apatites with resorption and overgrowth rims could mark a boundary of volatiles exsolution from the melt where loss of CO_2 from the melt increases apatite solubility causing resorption in some kimberlites (Grizzly) or almost complete apatite consumption in other (Misery, Beartooth). The accompanying increase in SiO_2 activity due to CO_2 degassing upon decompression (Moussallam et al., 2016) assimilation of country rock can lower the P_2O_5 solubility in the melt that triggers crystallization of apatite. This may explain formation of apatite rims in Grizzly.

Segregation of CO_2 fluid from the melt as well as assimilation of country rock would result in an increase of SiO_2 activity in the melt, which aids to decrease apatite solubility and promote apatite crystallization. Thus, the degree of crustal contamination could be reflected in the presence of kimberlitic apatite. This is evident in our natural kimberlites where we see apatite localized in and around assimilated crustal xenoliths or magmaclasts with diopside laths (Figure 3.4 C D E and 3.7 C D). While the absence of kimberlitic apatite could indicate: 1) exsolution of CO_2 fluid (increasing apatite solubility) early during ascent when high temperature promotes apatite dissolution (e.g. Misery, Beartooth); 2) low degree of assimilation of crustal rocks where due to lower SiO_2 apatite saturation limit is high supressing its crystallization. These various factors have potential economic implications relating to diamond quality due to the eruptive style of the kimberlite. A volatile rich kimberlite magma is associated with a rapid eruption, which results in less time for the dissolution of diamonds to occur thus preserving their quality (Fedortchouk, 2017).

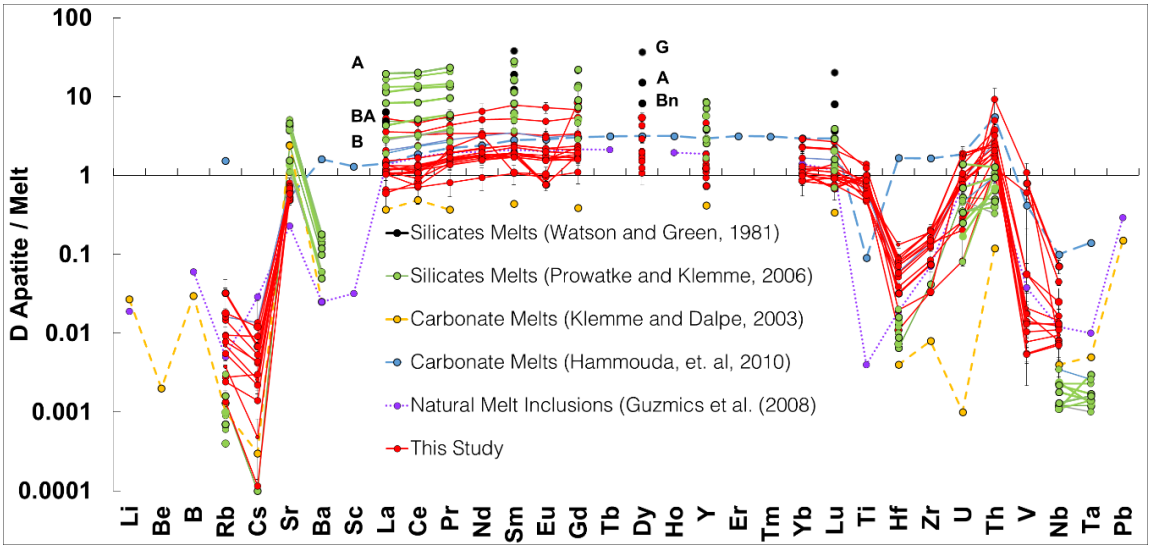

Figure 4.1: Comparison of apatite partition coefficients from this study with literature. A = andesite, BA = basaltic andesite, B = basalt, G = granite, Bn = basanite. Hammouda et al., 2010 used average of $n_{apatite}$= 3, n_{melt} = 4; Klemme and Dalpe, 2003 used average of $n_{apatite}$= 3, n_{melt} = 8.

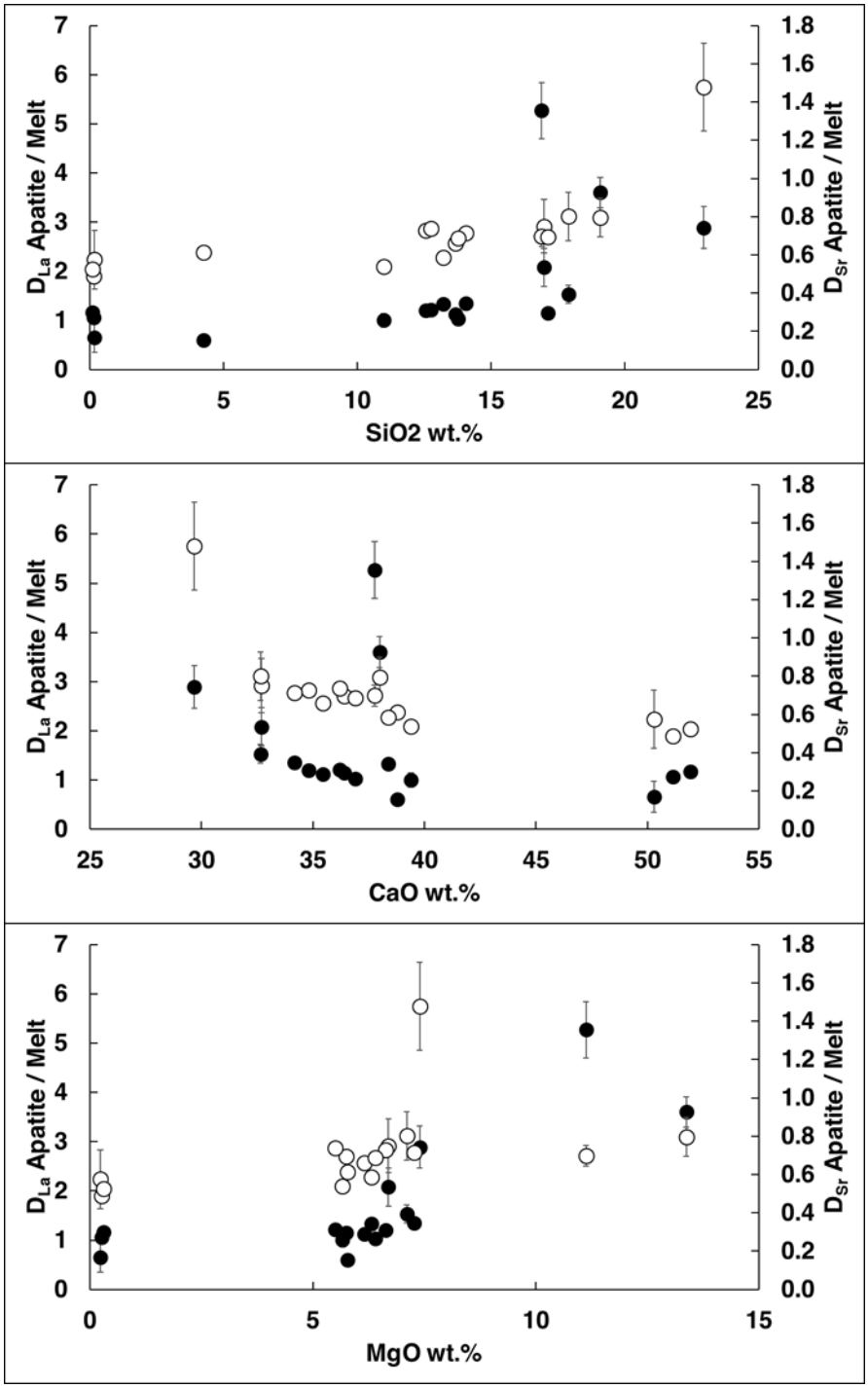

Figure 4.2: Apatite/melt partition coefficients for La (solid symbols) and Sr (unfilled symbols) as a function of melt composition (wt. % EMPA).

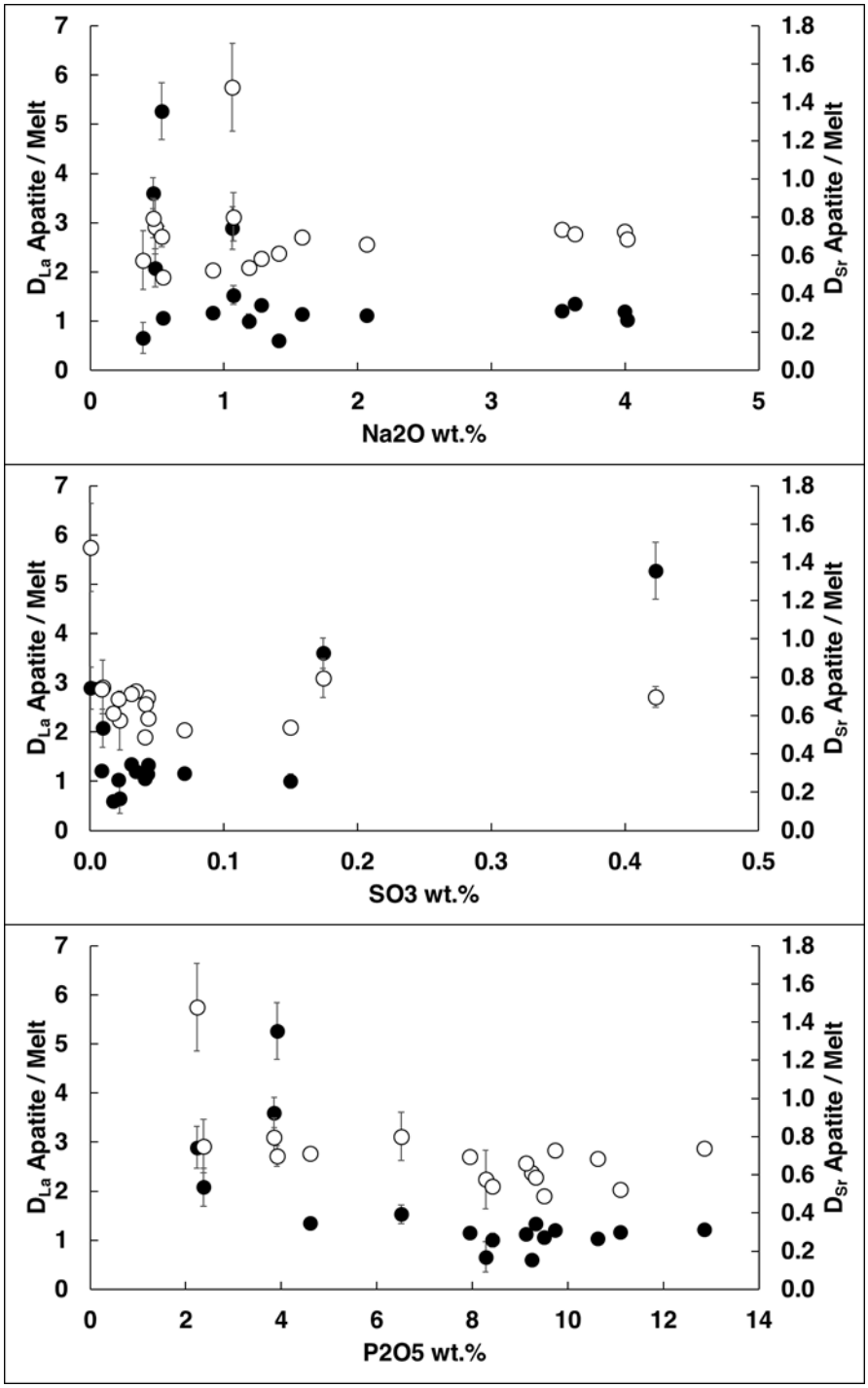

Figure 4.2 Continued: Apatite/melt partition coefficients for La (solid symbols) and Sr (unfilled symbols) as a function of melt composition (wt. % EMPA).

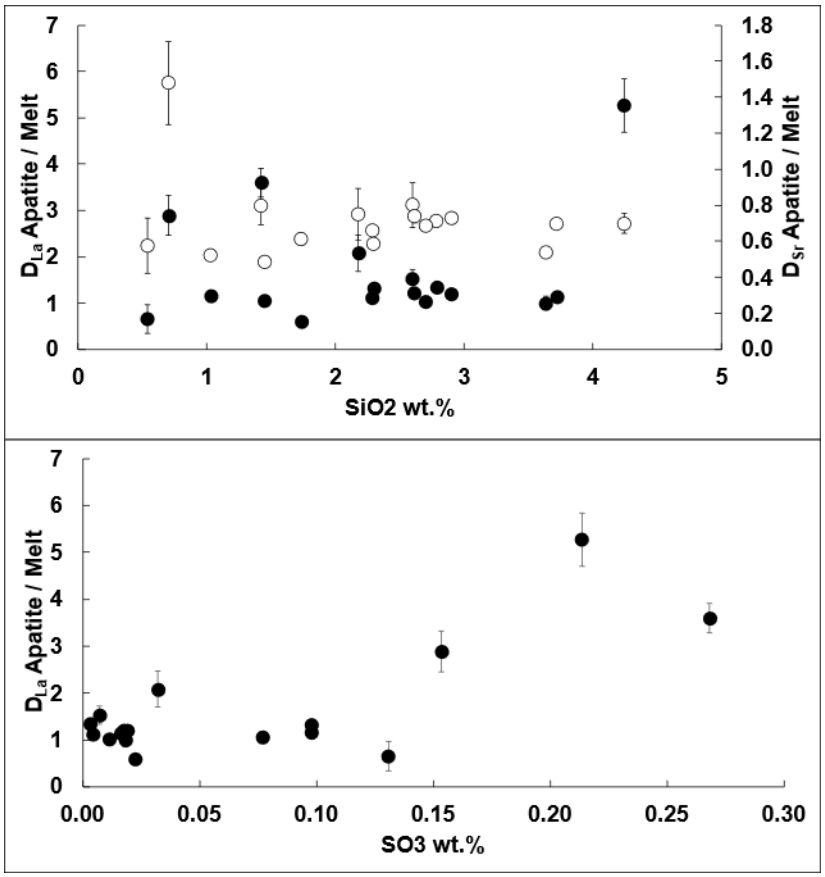

Figure 4.3: Apatite/melt partition coefficients for La (solid symbols) and Sr (unfilled symbols) as a function of apatite composition (wt. % EMPA).

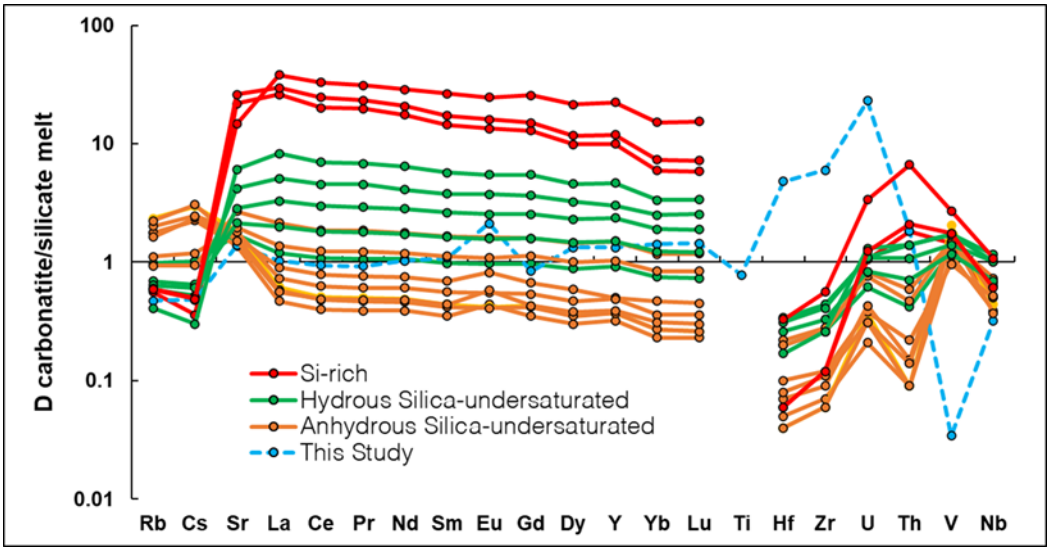

Figure 4.4: Partition coefficients $D^{carbonatite/silicate\ melt}$ for different trace elements obtained for different melt compositions by Martin et al., (2013) compared to $D^{carbonatite/silicate\ melt}$ calculated using $D^{Ap/carbonate}$ and $D^{Ap/silicate}$ from CAA and TA6 melt compositions in this study.

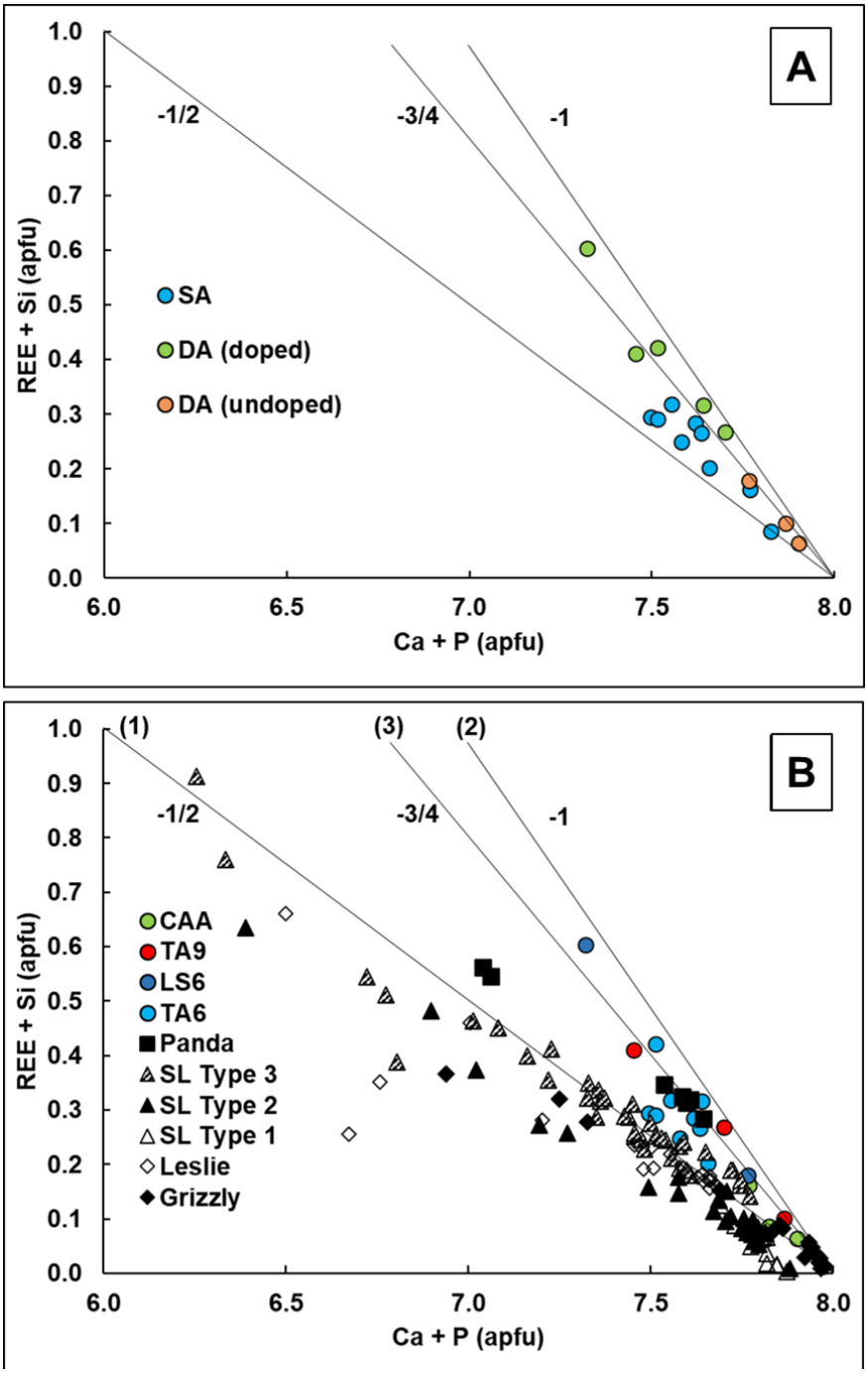

Figure 4.5: (A) The different substitution mechanisms observed in runs with SA and DA. SA favours a mix between reactions (1) and (3) while DA favours (3) and (2). (B) Substitution mechanisms of apatite (after Rønsbo, 1989). The slopes -1, -3/4 and -1/2 corresponds to reactions (2,4), (3), and (1) respectively. Natural kimberlite data from (Milligan, 2017) (triangle symbols). SL = Snap Lake kimberlite. Type 1 refers to radial acicular apatites found in fresh coherent kimberlite; Type 2 refers to subhedral apatite found in carbonate veins; Type 3 refers to prismatic apatites found in more altered kimberlite.

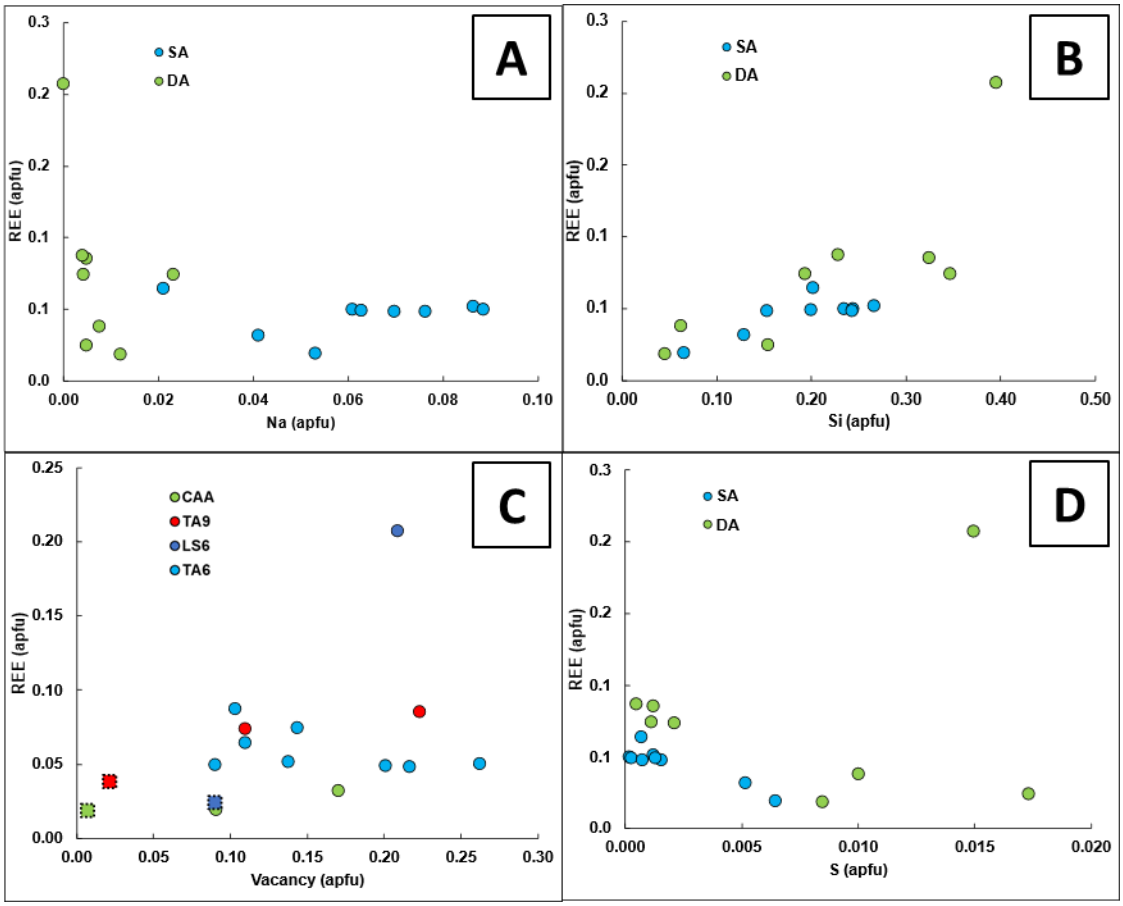

Figure 4.6: (A) Comparison between the REE and Na content in apatite. Synthetic apatite shows greater uptake of Na compared to Durango apatite. (B) Comparison between the REE and Si content in apatite, showing a positive correlation. (C) Comparison between the REE content and the vacancy present in apatite. There is a correlation where there is higher vacancy with higher REE content. Dotted square shapes represent undoped experiments. (D) Comparison between the REE and S content in apatite. No significant correlation is present.

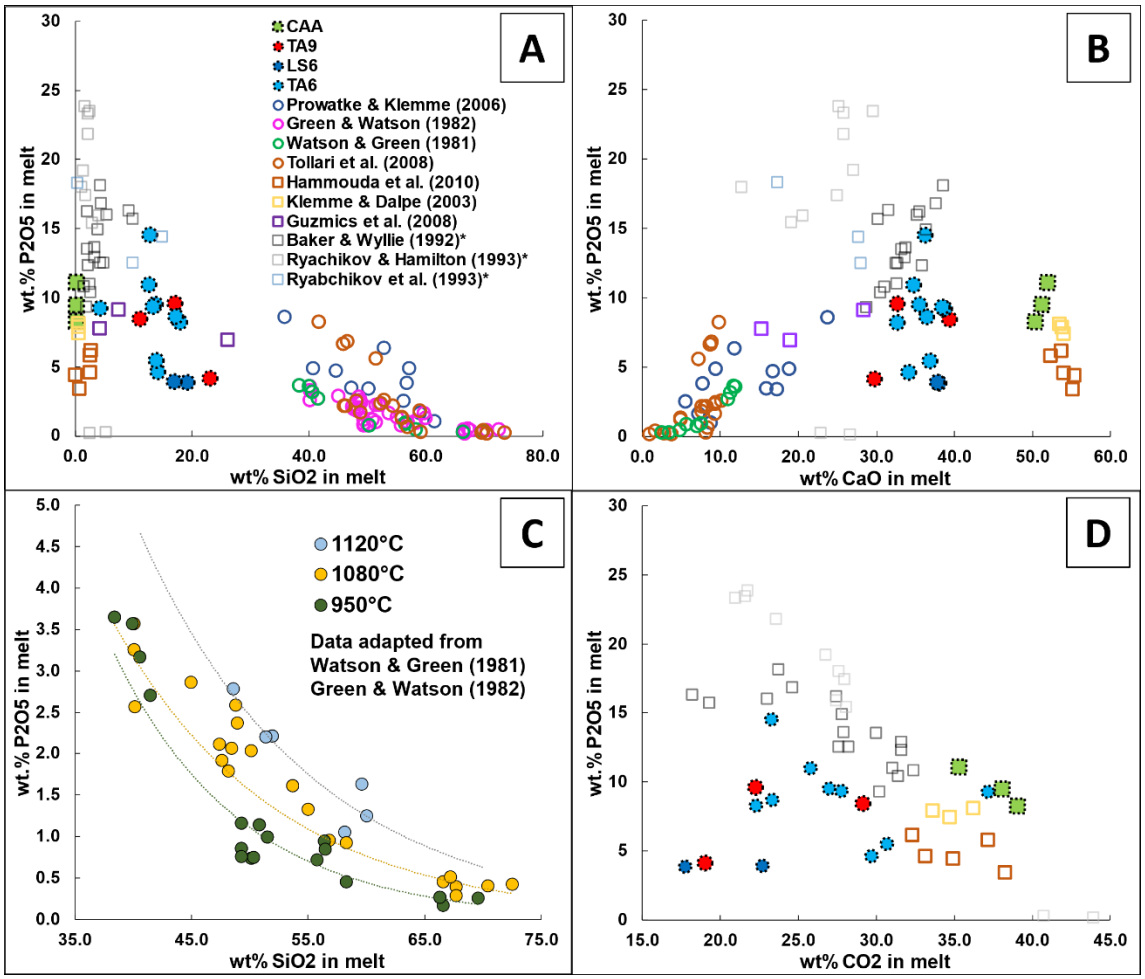

Figure 4.7: Comparison between apatite solubility, in terms of wt. % P_2O_5 in the melt, determined in this study with previous measurements. (A) and (B) show solubilities as a function of wt. % SiO_2 and wt. % CaO, respectively, and (D) as a function of wt. % CO_2. (*) Baker & Wyllie (1992), Ryabchikov et al. (1993), and Ryachikov & Hamilton (1993) are based on phosphate-rich carbonate melts in a mantle peridotite system. (C) Summarizes the temperature dependence of the apatite solubility as a function of wt. % SiO_2 in the melt, as determined by Watson and Green (1981) and Green and Watson (1982). Square symbols indicate carbonatitic melt and shapes with dotted outlines highlight this study.

4.4 Application to natural apatites from Lac de Gras and Orapa kimberlites

4.4.1 Crystallization conditions of apatite in kimberlites

Apatite's ubiquitous nature and its sensitivity to trace element uptake makes it a valuable indicator for inferring the evolution of melt composition during kimberlite ascent and emplacement. Therefore, by examining the changes in apatite abundance, texture and composition from natural kimberlite systems we can determine crystallization conditions for kimberlitic apatite and infer changes to the SiO_2 content of kimberlite melt.

Natural apatite data in this work allows to compare emplacement conditions of class 3 (Leslie and Boa kimberlites) with class 1 kimberlites (BK1 and AK15), and to examine differences between coherent and volcaniclastic facies of the same kimberlite. In coherent Leslie kimberlite, apatite forms abundant aggregates of acicular apatite crystals at the top 23 – 60 m of the pipe. This is followed by euhedral single crystals at deeper levels, which are small and less abundant towards the top (at 60 m) and at the bottom near the contact with country rocks. These are most abundant and large in the 127 – 162 m depth interval. Variation in SiO_2 content of the melt cannot explain variation in apatite abundance as bulk rock composition of Leslie samples from different depths show constant SiO_2 content (Fedortchouk and Canil, 2004). The abundant aggregates of acicular apatite crystals at shallow depth suggest high degree of undercooling due to rapid cooling at the surface and/or degassing (Höche et al. 2001; Milligan, 2017) and likely imply crystallization from a fluid. On the contrary, euhedral crystals at depths likely indicate low degrees of undercooling due to crystallization from a melt (Höche et al. 2001). In this case, the high abundance of apatite is in the middle, away from areas expected to be cooling faster. Instead, it is likely that crystallization was triggered by CO_2 loss which increases SiO_2

activity. Comparison of experimental runs using a bulk Leslie starting mixture produces groundmass phases and textures similar to that of natural Leslie kimberlite (Figure 4.8). This suggest that the experimental temperature of 1150°C and primary melt composition closely resembled the natural crystallization conditions at this interval of emplacement. Other Leslie based starting mixtures containing more CO_2 increased diopside stability.

The composition of acicular and euhedral apatite in Leslie kimberlite also shows distinct differences (Figure 3.8 A). Both groups form a continuous trend for most elements except for more abrupt increase in SrO in acicular apatite. The use of SiO_2 vs. SrO proposed by Soltys et al. (2020) for discriminating between hypabyssal and root zone coherent kimberlites (CK) shows that euhedral apatite plots in the hypabyssal field (low Sr, high and variable Si), whereas acicular trends towards root zone CK (high and variable Sr, low Si) (Figure 3.8 C). Overall, acicular apatite shows lower SiO_2 and F but higher REE and Sr (Figure 3.8 B D). Higher Sr points towards crystallization in equilibrium with fluid due to high SrO partitioning in apatite in aqueous fluid (Ayers and Watson, 1993), whereas higher SiO_2 in euhedral apatite agrees with its crystallization from a CO_2-rich melt as proposed by Soltys et al. (2020) due to coupled substitution of $[SiO_4]^{4-}$ and $[CO_3]^{2-}$ instead of two $[PO_4]^{3-}$. The similar acicular texture of aggregated Leslie apatite to the Type 1 and 2 Snap Lake apatite would also point towards a fluid origin (Milligan, 2017). In the emplacement model by Nowicki et al. (2008), partial melt fragmentation occurs when the lighter ash particles are lost along with incompatible elements upon eruption at the surface. This is in agreement with our data in two ways. First, where we see that the euhedral apatite composition of Leslie CK is not just purely apatite from hypabyssal kimberlite. This composition would be the result of LREE depletion through melt fragmentation. Second,

exsolution of the magma led to a fluid phase accumulating towards the top of the pipe evident by the higher Sr and acicular textured apatites.

Boa kimberlite from Ekati Mine comprises volcaniclastic (PK) facies with low apatite abundance and coherent facies (CK) with most abundant apatite near the contact with PK at 53.3m and 66.2m and becoming less abundant at 84.8m. The radial acicular nature of the shallower apatites found in high abundance would indicate high degrees of undercooling and possibly crystallization of fluid. Acicular and euhedral apatites in Boa are similar in composition. At the same time, they also show the same compositional trends as Leslie apatites and both varieties follow "hypabyssal" SiO_2 vs. SrO trend from Soltys et al. (2020). Similarity of Boa crystallization conditions to that hypabyssal dykes bodies is further supported by similarity of Boa apatites to the apatite described in Snap Lake hypabyssal dyke, which also contain euhedral and acicular aggregated apatite varieties (Milligan, 2017).

AK15 kimberlite CK intrusion contains discrete euhedral to subhedral apatite with low LREE and Sr contents throughout the groundmass (Figure 3.6, 3.8) which suggest crystallization from a melt probably CO_2-rich due to elevated SiO_2 content. The CK here shows a "hypabyssal" SiO_2 vs. SrO trend trend following Soltys et al. (2020) (Figure 3.8 C) Apatite is abundant at the top (56.16m) becomes rare and extremely small at depths (98.48m) and completely disappear at 191 m. The possible reasons for lowering P_2O_5 solubility and reaching apatite saturation resulting in abundant apatite towards the top of the intrusion are: 1) temperature decrease, 2) loss of CO_2-rich fluid phase and/or crustal contamination increasing SiO_2 content or activity in the melt, 3) the crystallization of other

groundmass minerals increases P_2O_5 melt content, and 4) decrease in CaO and CO_2 content of the melt due to the separation of a carbonate phase lowering P_2O_5 solubility.

BK1 kimberlite pipe contains apatite in both CK facies (CK-A and CK-B) and in KPK facies. In the KPK facies, apatite forms euhedral crystals with oscillatory zoning overgrown cores of olivine in drillhole H002 and aggregates of acicular crystals within serpentine – diopside replacements of assimilated crustal xenoliths in drillhole H003. The euhedral apatite shows low Sr and higher LREE whereas acicular apatite has high Sr and lower LREE (Table 3.1; Figure 3.8 A). In CK-A occurring above KPK in both drillholes, apatite is associated with groundmass phlogopite following it in crystallization sequence forming acicular aggregates in H002 and small irregular grains intergrown with phlogopite in H003. Both KPK and CK-A apatite follow "root zone CK" trend defined by Soltys et al (2020) with low SiO_2 and elevated SrO (Figure 3.8 A) indicating contribution of fluid. However, high F in CK-A and low in KPK in addition to much higher Sr in KPK than in CK-A suggest that apatite likely formed from fluid in KPK but from volatile-saturated melt in CK-A. Apatite is scarce in CK-B occurring as aggregates of acicular crystals in the top samples and forming small euhedral crystals in the bottom sample. This is similar to the morphology of apatite in CK from Leslie and Boa kimberlites. Unlike apatite from Ekati kimberlites showing high REE content, apatites from the Orapa cluster kimberlites have much lower REE due to early crystallization of perovskite, another large host of trace elements and REE. Apatite from the three facies in BK1 follow trend of Sr increase from CK-B to CK-A to KPK.

Variation in Sr content in apatite from the three kimberlite units (Figure 3.8 A). confirms the effect of fluid on their emplacement processes. Apatite/fluid partition coefficient for Sr

is 33 compared to 28 for Ce (Ayers and Watson, 1993), whereas in apatite/melt partitioning of Sr is >1 in this study. Composition of apatites from BK1 show an increasing presence of fluid from CK-B to CK-A to KPK.

These interpretations are in close agreement with kimberlite-induced diamond resorption textures that suggest CK-B crystallized from a fluid-free melt, whereas CK-A and KPK formed from a melt with an abundance of free fluid (Fedortchouk et al., 2017).

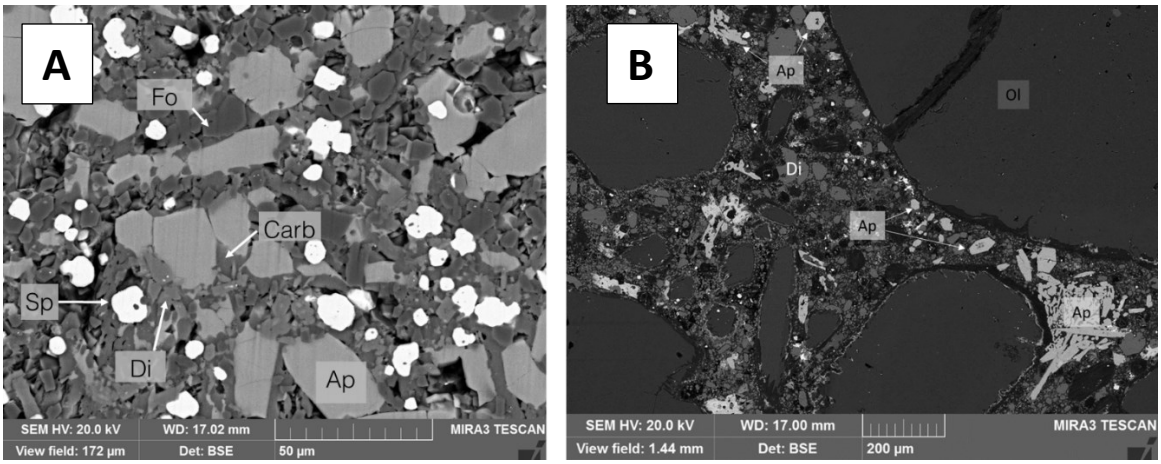

Figure 4.8: Comparison of textures observed in experimental run PC-186 using LS15 starting mixture (A) and natural Leslie kimberlite (B). Similar phases and texture are reproduced in our experimental run.

4.4.2 Modeling of kimberlite composition

The partition coefficients obtained in this study was used to assess the composition of kimberlite melt during apatite crystallization using two approaches. In both approaches, I obtain trace element content of the groundmass by doubling their concentration in the bulk rock composition. This is because the majority of hypabyssal kimberlite around the world consist of ≈25% of olivine macrocrysts and ≈25% of olivine micro-phenocrysts (Scott Smith, 2008), which do not take trace elements and REE in appreciable amounts. The remaining 50% is the finer grain groundmass which crystallized from kimberlitic melt.

Subsequent removal of various percentages of early groundmass phases (spinel, monticellite) which do not take REE, allows for estimating how much crystallization needs to occur in order to match the composition of kimberlite melt obtained from D_{REE} and REE composition in apatite obtained in this study.

The first approach calculates the partition coefficients of trace elements between apatite and melt using composition of apatite from Milligan (2017) and bulk rock composition of kimberlites from Fulop et al. (2017) and Nowicki et al. (2008) for different kimberlites as $D_i = X^{Ap}_i / X^{bulk\ rock}_i$ and compares them to our experimental partition coefficients. Figure 4.9 shows that for Leslie and Panda calculated $D_{LREE} >> D_{HREE}$. Partitioning of Sr and LREE (e.g., La) shows dependence on the composition of apatite-forming media. In addition to $D_{Sr} >> D_{La}$ when apatite crystallizes from aqueous fluid (Ayers and Watson, 1993), our data shows $D_{Sr} \approx D_{La}$ when apatite crystallizes from a carbonate melt, but $D_{Sr} < D_{La}$ when apatite crystallizes from silicate melt. Modelling of D in Figure 4.9 suggests that the melt of Leslie was more carbonate-rich than Panda during crystallization of apatite. Higher CO_2 content in Leslie would agree with its less explosive eruption than Panda (Nowicki et al., 2008) and late exsolution of fluid (Moussalam et al., 2016). Snap Lake data for type 3 apatite on Figure 4.9 suggest that Snap Lake is even more carbonatitic melt then Leslie. This agrees with bulk rock data. In Panda and Leslie, D_{LREE} match closely to the compatibility of silicate + synthetic apatite experiments from this study when 97% of material is removed but result in far lower D_{HREE} (Figure 4.9 B). This indicates that these late kimberlite melts are far from a pure carbonate composition. The presence of perovskite would not be able to explain the depletion of LREE and Sr as there is no depletion observed in the HFSE which it is highly compatible in perovskite (Bayer, 2013). In addition, textural

relationships show that apatite crystallized relatively early in Leslie, lowering the likelihood of perovskite depletion (Milligan, 2017).

All SL apatites show similar slopes and patterns of Ds for all trace elements to those determined in this study except for Sr (Figure 4.9 A). SL (Snap Lake) Type 1 (radial acicular apatites in CK) and 2 (subhedral apatite in carbonate) is very close to the pattern of experiments with silicate melt in this study. However, the $D_{Sr} >> D_{La}$ for Type 1 and Type 2 indicates crystallization from fluid rather than a melt. The main difference is in SL Type 3 (prismatic apatites in altered kimberlite) which also shows a similar pattern except where LREEs and Sr are considerably more compatible and $D_{Sr} \approx D_{La}$. This implies that Type 1 and 2 had a similar origin history and Type 3 is different. Textures and Sr enrichment of Type 1 and 2 apatites suggest a fluid related origin and this is supported by the pattern of Ds observed where $D_{Sr} >> D_{La}$. Prismatic Type 3's LREE enrichment points to a magmatic one which agrees with $D_{Sr} \approx D_{La}$ (Milligan, 2017). It is not unreasonable to say that the melt composition of Snap Lake was likely a low-SiO_2 (10-20 wt. %) based on our experimental melts that experienced decoupling of a fluid that causes a depletion seen in Type 3. The fluid went on to form Type 1 and 2 apatites and the remaining melt formed Type 3.

A proportion of 3% residual melt would be necessary at the time of apatite crystallization to achieve D_{LREE} of Leslie and Panda to match the D_{LREE} of silicate DA. A residual melt of less than 1.5% would be required to achieve D_{LREE} of the experimental carbonate D_{LREE}. It is less reasonable to crystallize 97% of the melt to achieve D_{LREE} of silicate DA and 99% for the carbonate D_{LREE} because there would be no explanation for the extreme enrichment of HREE in the melt. A depletion event prior to crystallization is more reasonable in the

case of Leslie and Panda. For SL Type 3 apatite crystallization from a residual melt of approximately 25% would be required to match the D_{REE} of silicate DA, 12% for silicate SA, and 6% for carbonate compositions. Similar D_{REE} in carbonate compositions would require approximately 25% of residual melt in SL Type 1 and 2.

The second approach uses experimentally determined in this study trace element partition coefficient and compositions of natural apatite from Milligan (2017) to calculate concentration of trace elements in a hypothetical evolved kimberlite magma and compare it with the bulk compositions of kimberlites after removal of 50% xenocrystal material. This approach produces melts with similar trace element patterns to the bulk rock kimberlite (Leslie and Panda) composition from Nowicki et al. (2008) normalized to Cl-chondritic values from McDonough and Sun (1995) (Figure 4.10). Both silicate and carbonate based melt models produce similar patterns to each other and to the bulk rock concentrations. The silicate D based melts fit the best, confirming that the original kimberlite melt composition was most likely a low-SiO_2 one. Comparing Leslie and Panda, there is a greater depletion of HREE and enrichment in Sr in Leslie. In both Leslie and Panda, we see the same depletion of LREE, Sr, and Th in the bulk. HREE in all Leslie models fit very well with the bulk Leslie.

The Ds obtained in runs with carbonate melt and DA shows higher concentration due to lower Ds compared to SA (Figure 4.9). In all cases, LREE, MREE, and Sr would require over 99% melt crystallization to match the bulk and model compositions. It is unlikely apatite only started crystallization once these residual melt portions had been reached even as a late stage phase in kimberlite groundmass. Therefore, apatite crystallized before the fluid exsolution of the melt.

Partitioning of La and Sr in apatite is different in different melt compositions where melts with higher SiO_2 show much higher compatibility in La than in Sr. As such, we attempt to use the La and Sr concentration in apatite as an indicator of melt composition as illustrated in Figure 4.11. The melt compositions that produce low D_{REE} between apatite and melt (PC-178 CAA, carbonate with DA and PC-198 TA6, run that produced a very low SiO_2 melt) have the lowest La and Sr concentrations (circle 1) which can be linked to melts with very low SiO_2 content/carbonatitic in nature (Figure 4.11). Melt compositions that produced high D_{REE} between apatite and melt (more SiO_2 rich melt compositions) group together in circle 2 (Figure 4.11). The lack of diopside phase in the TA9 outlier (PC-179 TA9) from circle 2 may be the cause of the lower Sr and La, as a lower proportion of melt due to the presence of an addition phase could results in higher concentration of trace elements.

While the data shows that both La and Sr increase in compatibility with an increase in SiO_2 melt content, the Sr/La ratio which it increases by remains relatively constant when excluding the outlier (slope = ~1) despite the different melt compositions. Therefore, the Sr/La ratio cannot be used as an indicator for a specific melt composition in the kimberlitic range due to the limited difference in behavior of Sr and La with increasing SiO_2 melt content (Figure 4.11). However, it can be useful as an indicator for fluid as shown by the concentrations of natural apatites from Panda, Leslie, Boa, and BK1 kimberlite (Figure 4.11; Figure 3.8). Natural apatites trend towards higher Sr concentrations than the experimental runs due to some degree of apatite crystallization or re-equilibration with a fluid. This is supported by previous experiments which suggest that D_{Sr} is greater than D_{La} in an apatite/fluid system (Ayers and Watson, 1993). Apatite

textures discussed in chapter 3.1 also support a fluid origin which can also be seen by the Sr enrichment and low La most prominently in BK1's acicular apatites (Figure 4.11). Experiments which included the addition of water do not show a clear distinction from anhydrous runs. This may be in part due to the fluids in these runs not reaching saturation.

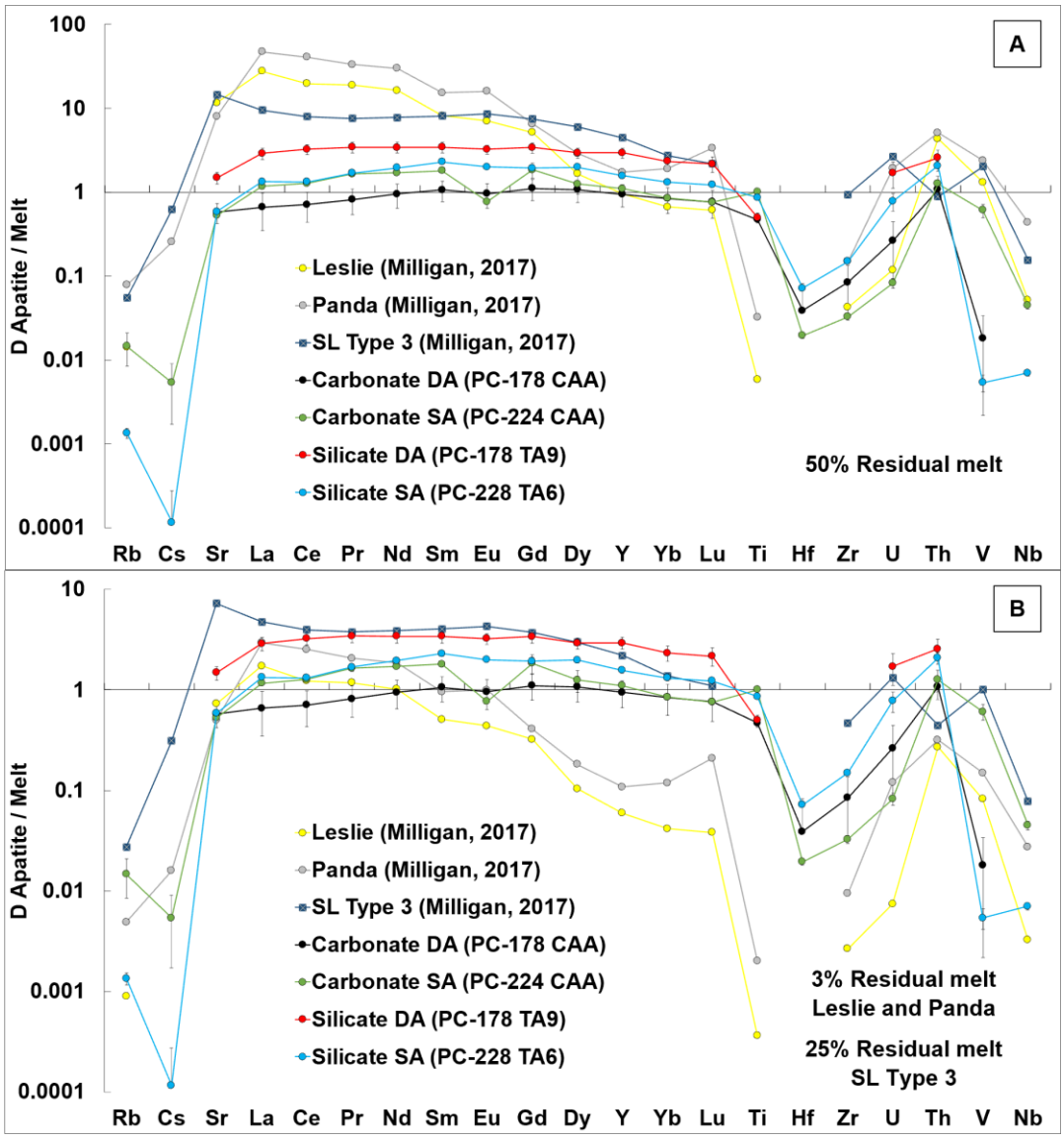

Figure 4.9: Partition coefficients calculated using compositions of bulk composition of kimberlite from Nowicki et al., 2008 and apatite compositions from Milligan, 2017). A) Trace element concentrations of the melt at 50% residual melt. (B) Trace element

concentrations of the melt at 3% residual melt for Leslie and Panda, 25% residual melt for SL Type 3.

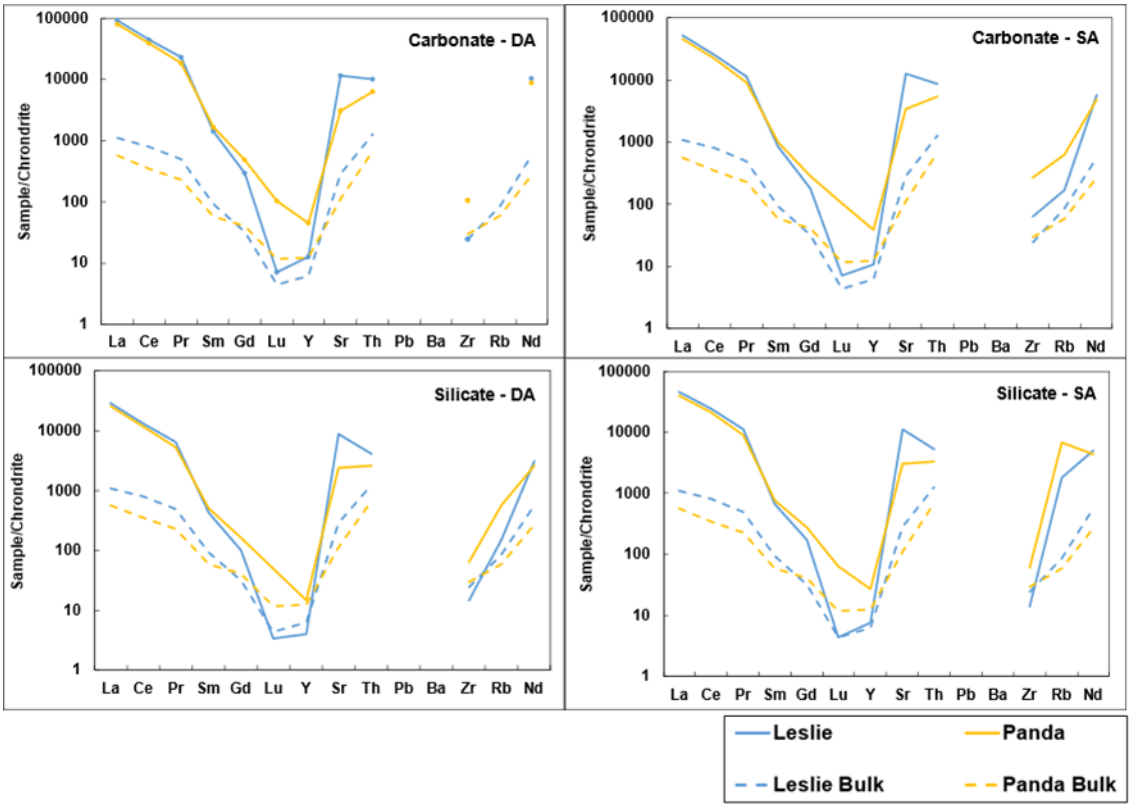

Figure 4.10: Modeling of kimberlite melt composition using natural apatite trace element concentrations (Milligan, 2017) with experimentally determined partition coefficients in melts (from this study) are solid lines (Leslie and Panda). In comparison is bulk kimberlite compositions from whole rock analyses shown as dashed lines (Leslie Bulk and Panda Bulk) (Nowicki et al., 2008). All melts are corrected for 50% macrocrystal phases removed (50% residual melt).

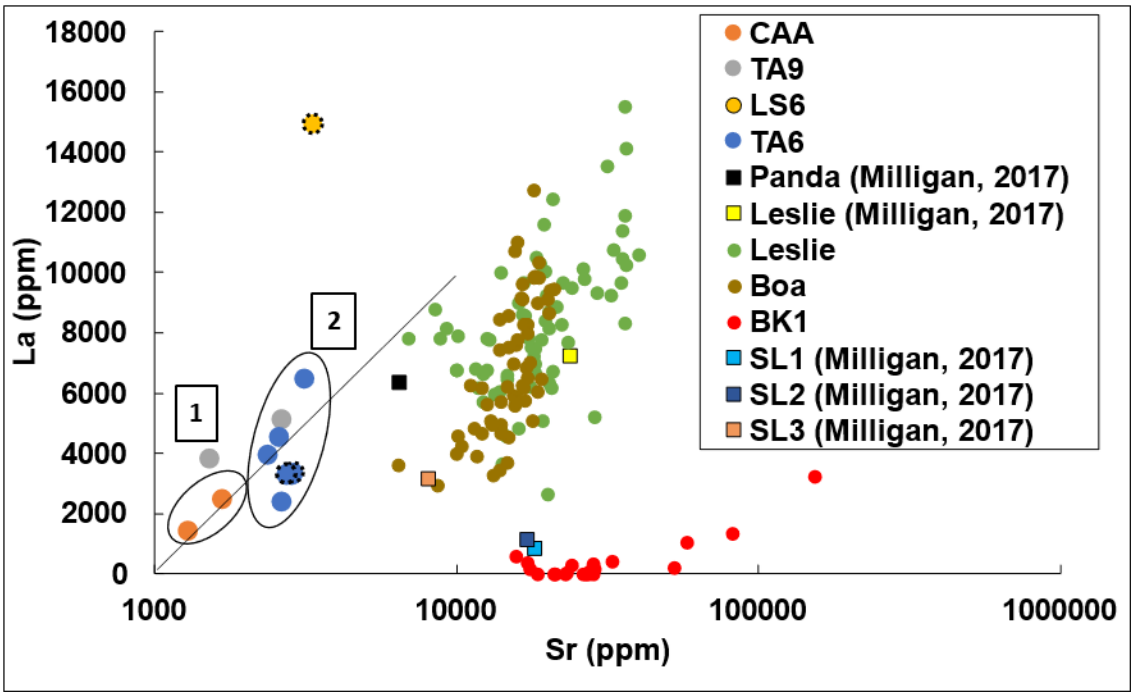

Figure 4.11: Comparison of La and Sr concentrations in apatites from experimental runs and natural apatites. Data points with dotted outline indicate experimental runs with water. All samples shown are doped experiments. (1) carbonate group, (2) low SiO_2 group.

Chapter 5 Conclusions

5.1 Conclusions

1. Apatite occurrence varies widely across different kimberlite pipes but also within a single kimberlite pipe. Apatite texture and chemical compositions is found to change throughout one kimberlite unit and even more so between different facies. We find that presence of free fluid phase in kimberlite magma results in apatite with acicular aggregated textures and will cause a distinct Sr enrichment in apatite. Apatite from CK in class 1 kimberlite (BK1, Orapa cluster) and class 3 pipe-infill kimberlite (Leslie, Ekati Mine) follow distinct LREE-Sr trends. In BK1 kimberlite KPK samples show textures and geochemical signatures suggesting significant role of fluids, while transitional CK-A apatites plot in the middle between KPK and root zone CK-B. This shows a progressive role of fluid in crystallization of large class 1 kimberlites. Pipe-infill CK in Ekati, on the contrary, follow the hypabyssal trend (determined for sills and dykes) with high LREE, low Sr as apatites from sills and dykes. Thus, suggesting crystallization from the melt. However, an enrichment in Sr in acicular apatite from Leslie kimberlite also demonstrates the role of fluid in crystallization of Leslie.

2. Experimentally determined apatite/melt partition coefficients in low-SiO_2 melts analogous of kimberlitic melts show that trace elements are less compatible than in mafic to felsic silicate melts but more compatible than for carbonatitic melts. A positive correlation is found between D_{REE} and increasing SiO_2 and SO_3 content of the melt. Temperature, pressure, water content, and oxygen fugacity had no notable effect on D_{REE} in these low SiO_2 melts. The REE apatite/melt partition coefficient in

carbonate melt composition depend on the type of apatite (higher compatibility in synthetic vs. lower compatibility in natural Durango).

3. This study demonstrated that discrepancy in partitioning coefficients between apatite and carbonatitic melt in previous experimental studies is due to the presence of other elements such as sulfur and SiO_2 in the starting apatite and melt compositions, which may have increased the compatibility of REE.

4. The modelled partition coefficients and evolved kimberlite melt composition using our experimental partition coefficients for carbonate and silicate melts show good agreement with bulk rock compositions of CK and PK given the constraints of volatile loss. This shows that apatite crystallizes from silicate-carbonate melts and that the content of carbonate components increases from VK (Panda) to extrusive CK (Leslie) to hypabyssal (Snap Lake) – likely contributing to the differences in the emplacement processes of these magmas.

5. The solubility of apatite in low SiO_2 melts follows the trend of silicate melts where increasing SiO_2 melt content lowers apatite solubility. Carbonate melts show lower apatite solubility with higher CaO (>50 wt. %) content. Decreasing CO_2 content in melt decreases apatite solubility. However, the use of apatite solubility and partition coefficients alone is insufficient in evaluating changes in fluid content in kimberlites. Instead, the La/Sr ratio in apatite is better suited for indicating the presence of fluids which can indicate greater diamond preservation potential of a kimberlite.

5.2 Further Work

1. Low totals in apatite analyses require a robust analytical method to determine the exact composition and to better understand the substitution mechanisms involved, particularly with the vacancy and carbonate substitutions.

2. Given the complexity of kimberlites, a larger sample size of large apatites from more localities would be ideal in order to obtain more robust data.

3. The cause of the partitioning discrepancy between synthetic and natural apatites is still not well understood and further investigation would be needed.

4. Fractionation of trace elements is an important process in kimberlites but is difficult to estimate the exact proportions due to separation of phases and contamination. Producing models that account for different specific depletion mechanisms may help better interpret the emplacement processes.

References

Ayers, J.C., and Watson, E.B. 1993. Apatite/fluid partitioning of rare-earth elements and strontium: Experimental results at 1.0 GPa and 1000°C and application to models of fluid-rock interaction. Chemical Geology 110: 299-314

Arima, M., Kozai, Y., 2008. Diamond dissolution rates in kimberlitic melts at 1300-1500 °C in the graphite stability field. Eur. J. Mineral. **20**: 357-364

Baker M. B., and Wyllie P. J. 1992 High-pressure apatite solubility in carbonate-rich liquids: implications for mantle metasomatism. Geochimica et Cosmochimica Acta **56:** 3409-3422

Beyer, C., Berndt, J., Tappe, S., and Klemme, S. 2013. Trace element partitioning between perovskite and kimberlite to carbonatite melt: New experimental constraints. Chemical Geology **363:** 132-139

Bellis, A., and Canil, D. 2005. Ferric Iron in CaTiO3 Perovskite as an Oxygen Barometer for Kimberlitic Magmas I: Experimental Calibration. Journal of Petrology **48:** 219-230

Bellis, A., and Canil, D. 2005. Ferric Iron in CaTiO3 Perovskite as an Oxygen Barometer for Kimberlitic Magmas II: Applications. Journal of Petrology **48:** 231-252

Blundy, J., and Wood, B. 2003. Partitioning of trace elements between crystals and melts. Earth and Planetary Science Letters **210**: 383-397

Boyce, J.W., Hervig, R.L. 2008. Magmatic degassing histories from apatite volatile stratigraphy. Geological Society of America **36**: 63-66

Belousova, E.A., Griffin, W.L., O'Reilly, S.Y., and Fisher, N.I. 2002. Apatite as an indicator mineral for mineral exploration: trace-element compositions and their relationship to host rock type. Journal of Geochemical Exploration **76**: 45-69

Brooker, R.A., and Kjarsgaard, B.A. 2011. Silicate–Carbonate Liquid Immiscibility and Phase Relations in the System SiO2–Na2O–Al2O3–CaO–CO2 at 0·1–2·5 GPa with Applications to Carbonatite Genesis. Journal of Petrology **52**: 1281-1305

Cousens, L.B. 2000. Geochemistry of the Archean Kam Group, Yellowknife Greenstone Belt, Slave Province, Canada. The Journal of Geology **108**: 181-197

Chakhmouradian, A.R., Reguir, E.P., Mitchel, R.H. 2002. Strontium-Apatite: New occurrences, and the extent of Sr-FOR-Ca substitution in apatite-group minerals. Canadian Mineralogist **40**: 121-136

Chakhmouradian, A.R., Reguir, E., Kamenetsky, V.S., Sharygin, V.V., Golovin, A.V. 2013. Trace-element partitioning in perovskite: Implications for the geochemistry of kimberlites and other mantle-derived undersaturated rocks. Chemical Geology **353**: 112-131

Chakhmouradian, A.R., Reguir, E.P., Zaitsev, A.N., Couëslan, C., Xu, C., Kynický, J., Mumin, A.H., Yang, P. 2017. Apatite in carbonatitic rocks: Compositional variation, zoning, element partitioning, and petrogenetic significance. Lithos **274-275**: 188-213

Clement, C.R. 1982. A comparative geological study of some major kimberlite pipes in the Northern Cape and Orange Free State. Unpublished Ph.D. thesis. University of Capetown

Clement, C.R., and Reid, A.M. 1989. The origin of kimberlite pipes: an interpretation based on a synthesis of geological features displayed by southern African occurrences. Geological Society of Australia Special Publication **14**: 632-664

D'Oriano, C., Pelo, S.D., Podda, F., Cioni, R. 2008. Laser-Ablation Inductively Coupled Plasma Mass Spectrometry (LA-ICP-MS): setting operating conditions and instrumental performance. Periodico di Mineralogia **77(3)**: 65-74

Fedortchouk, Y., Canil, D. 2004. Intensive Variables in Kimberlite Magmas, Lac de Gras, Canada and Implications for Diamond Survival. Journal of Petrology **45**: 1725-1745

Fedortchouk, Y., Canil, D., Carlson, J.A. 2005. Dissolution forms in Lac de Gras diamonds and their relationship to the temperature and redox state of kimberlite magma. Contributions to Mineralogy and Petrology **150:** 54-69

Fedortchouk, Y., Matveev, S., Carlson, J.A. 2010. H_2O and CO_2 in kimberlitic fluid as recorded by diamonds and olivines in several Ekati Diamond Mine kimberlites, Northwest Territories, Canada: Earth and Planetary Science Letters **289**: 549–559

Field, M., and Scott Smith, B. H. 1999. Contrasting Geology and near-surface emplacement of kimberlite pipes in Southern Africa and Canada. *In* Proceedings of the 7th International Kimberlite Conference, Vol. 1, 214-237

Fleet, M.E., Liu, X., and Pan, Y. 2000b. Site preference of rare earth elements in hydroxyapatite [Ca10(PO4)6(OH)2]. Journal of Solid State Chemistry **149**: 391-398

Fulop, A., Kopylova, M.G., Ellemers, P., and Squibb, C. 2017. Geology of the Snap Lake kimberlite dyke, Northwest Territories, Canada, and its metasomatic interaction with grantie. In Long Abstracts 11th International Kimberlite Conference, Gaborone.

Green, T.H., and Watson, E. B. 1981. Crystallization of Apatite in Natural Magmas Under High Pressure, Hydrous Conditions, with Particular Reference to 'Orogenic' Rock Series. Contributions to Mineralogy and Petrology **79**: 96-105

Guzmics T., Zajacz Z., Kodola´nyi J., Halter W., Szabo, C. 2008. La-ICP-MS study of apatite- and K feldspar-hosted primary carbonatite melt inclusions in clinopyroxenite from lamprophyres, Hungary: implications for significance of carbonatite melts in the Earth's mantle. Geochimica et Cosmochimica Acta **71**: 1864–1886

Hammouda, T., Chantel, J., Devidal, J. L. 2010. Apatite solubility in carbonatitic liquids and trace elements partitioning between apatite and carbonatite at high pressure. Geochimica et Cosmochimica Acta **7:** 7220-7235

Höche, T., Moisescu, C., Avramov, I., and Rüssel, C. 2001. Microstructure of SiO2-Al2O3-CaO-P2O5-K2O-F- glass ceramics. 1. Needlelike versus isometric morphology of apatite crystals. Chemistry of Materials **13**: 1312-1319

Jochum, K.P., Nohl, L., Herwig, K., Lammel, E., Stoll, B., Hofmann, A. W. 2005. GeoReM: A new geochemical database for reference materials and isotopic standards Geostandards and Geoanalytical Research **29**: 333-338

Ketcham, R. A. 2015. Calculation of stoichiometry from EMP data for apatite and other phases with mixing on monovalent anion sites. American Mineralogist **100**: 1620-1623

Klemme, S., Dalpe, C., 2003. Trace element partitioning between apatite and carbonatite melt. American Mineralogist **88**: 639-646

Lorenz, V., 1975. Formation of phreatomagmatic maar–diatreme volcanoes and its relevance to kimberlite diatremes. Physics and Chemistry of the Earth **9**: 17–29

Martin, L.H.J., Schmidt, M.W., Mattsson, H.B., Guenther, D. 2013. Element Partitioning between Immiscible Carbonatite and Silicate Melts for Dry and H2O-bearing Systems at 1–3 GPa. Journal of Petrology **54**(11): 2301-2338

Mao, M., Rukhlov, A.S., Rowins, S.M., Spence, J., and Coogan, L.A. 2016. Apatite trace element compositions: a robust new tool for mineral exploration. Economic Geology **111**: 1187-1222

McDonough W. F. & Sun S-s. (1995) “The Composition of the Earth” Chemical Geology **120:** 223-253

Milligan, R. S. 2017. Features of apatite in kimberlite from Ekati diamond mine and Snap Lake: modelling kimberlite composition. M.Sc. thesis, Department of Earth Science, Dalhousie University, Halifax, N.S

Mitchell, R. H. 1986. Kimberlites: Mineralogy, Geochemistry, and Petrology. New York: Plenum

Moussallam, Y., Morizet, Y., Massuyeau, M., Laumonier, M., Gaillard, F., 2015. CO_2 solubility in kimberlite melts. Chemical Geology **418**: 198-205

Moussallam, Y., Morizet, Y., Gaillard, F., 2016. H_2O-CO_2 solubility in low SiO_2-melts and the unique mode of kimberlite degassing and emplacement. Earth and Planetary Science Letters **447**: 151-160

Pan, Y., and Fleet, M.E. 2002. Compositions of the apatite-group minerals: substitution mechanisms and controlling factors. Reviews in Mineralogy and Geochemistry **48** (1): 13-49

Pasteris, J. D., Yoder, C. H., Sternlieb, M. P., Liu, S. 2012. Effect of carbonate incorporation on the hydroxyl content of hydroxylapatite. Mineralogical Magazine **76 (7)**: 2741-2759

Piccoli, P., and Candela, P. 2002. Apatite in Igneous Systems. Reviews in Mineralogy and Geochemistry **48**: 255-292

Prowatke, S., and Klemme, S. 2006. Trace element partitioning between apatite and silicate melts. Geochimica et Cosmochimica Acta **70**: 4513-4527

Rønsbo, J.G. 1989. Coupled substitutions involving REEs and Na and Si in apatites in alkaline rocks from the Ilimaussaq intrusion, South Greenland, and the petrological implications. Am Mineral **74**: 896-901

Russell, J.K., Porritt, L.A., Lavallée, Y., Dingwell, D.B. 2012. Kimberlite ascent by assimilation-fuelled buoyancy. Nature **481**: 352-356

Ryabchikov I. D., and Hamilton D. l. 1993. Interaction of carbonate-phosphate melts with mantle peridotites at 20–35 kbar. S. Afr. J. Geol. **96**: 143–148

Ryabchikov I. D., Orlova G. P., Senin V. G. and Trubkin N. V. 1993. Partitioning of rare earth elements between phosphaterich carbonatite melts and mantle peridotites. Mineral. Petrol. **49**: 1–12

Scott Smith, B. H. 2008. Canadian kimberlites: Geological characteristics relevant to emplacement. Journal of Volcanology and Geothermal Research **174**: 9-19

Scott Smith, B.H., Nowicki, T. E., Russell, J. K., Webb, K. J., Mitchell, R. H., Hetman, C. M., Robey J. A. 2018. A Glossary of Kimberlite and Related Terms. Scott-Smith Petrology Inc., North Vancouver, BC, Canada

Scott Smith, B.H., Nowicki, T. E., Russell, J. K., Webb, K. J., Mitchell, R. H., Hetman, C. M., Harder, M., Skinner, E. M. W., Robey J. A. 2013. Kimberlite Terminology and Classification. *In* Proceedings of 10th International Kimberlite Conference, Vol. 2, pp. 1-17

Skinner, E. M. W, Marsh, J. S. 2004. Distinct kimberlite pipe classes with contrasting eruption processes. Lithos **76**: 183-200

Soltys, A., Giuliani, A., Phillips, D., 2017. Apatite from the Kimberley Kimberlites (South Africa): Petrography and Mineral Chemistry. *In* Proceedings of 11th International Kimberlite Conference Extended Abstract No. 11IKC-4491

Soltys, A., Giuliani, A. & Phillips, D., 2020. Apatite compositions and groundmass mineralogy record divergent melt/fluid evolution trajectories in coherent kimberlites caused by differing emplacement mechanisms. Contributions to Mineralogy and Petrology **175:** 49

Stamm, N., Schmidt, M.W., 2017. Asthenospheric kimberlites: Volatile contents and bulk compositions at 7 GPa. Earth and Planetary Science Letters **474**: 309-321

Stone, R. S., and Luth, R.W. 2016. Orthopyroxene survival in deep carbonatite melts: implications for kimberlites. Contributions to Mineralogy and Petrology **171**: 63

Sparks, R. S. J., Baker L, Brown RJ, Field M, Schumacher J, et al. 2006. Dynamics of kimberlite volcanism. Journal of Volcanology and Geothermal Research **155**: 18–48

Sparks, R. S. J. 2013. Kimberlite Volcanism. Annu. Rev. Earth Planet. Sci. **41**:497–528

Tollari, N., Baker, D.R., and Barnes, S.-J. 2008. Experimental effects of pressure and fluorine on apatite saturation in mafic magmas, with reference to layered intrusions and massif anorthosites. Contributions to Mineralogy and Petrology **156**: 161-175

Watson, E. B., and Green, T.H. 1981. Apatite/liquid partition coefficients for the rare earth elements and strontium. Earth and Planetary Science Letters **56**: 405-421

Watson, E., Wark, D., Price, J., Van Orman, J., 2002. Mapping the thermal structure of solid-media pressure assemblies. Contrib. Mineral. Petrol. **142**: 640-652

Appendix A: Supplemental Figures

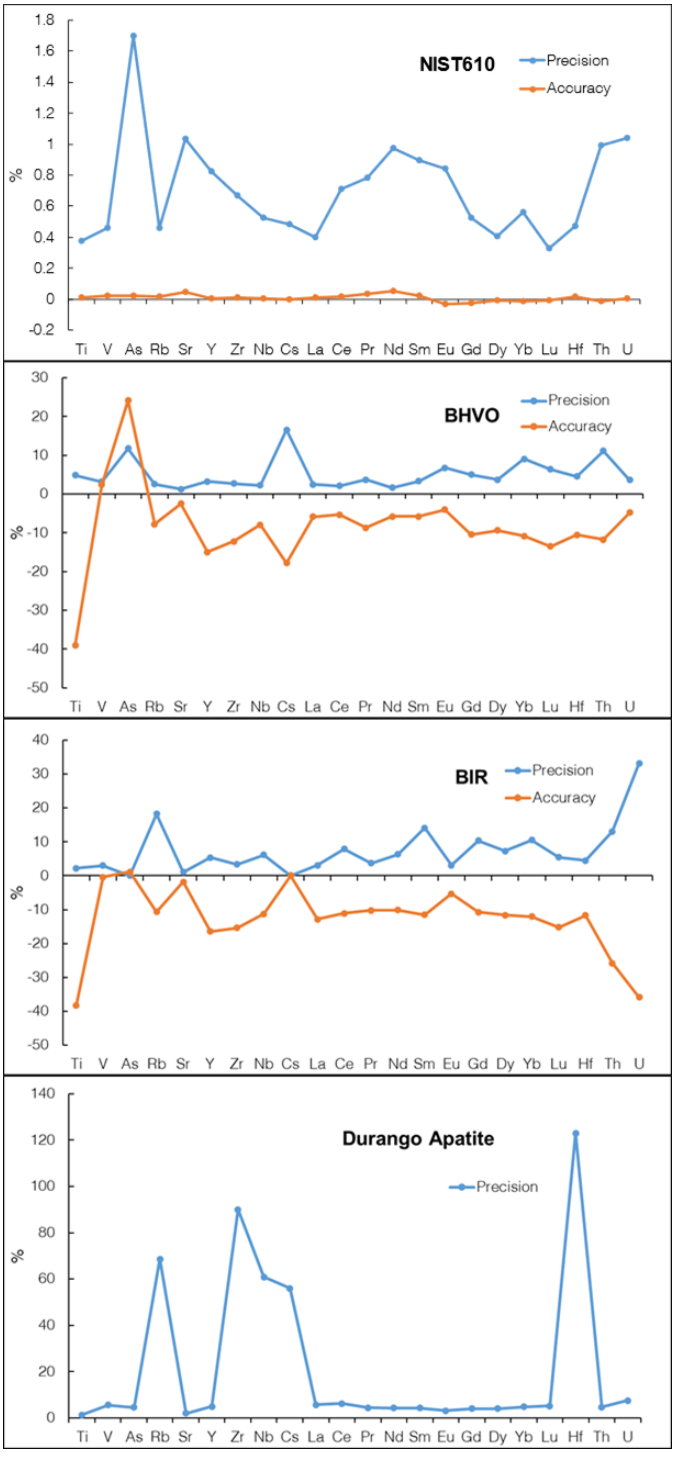

Figure ES 1: Precision (relative standard deviation %) and accuracy (relative deviation % from the reference values) of the LA-ICP-MS analyses when comparing measured standards to reference values using a spot size of 25 µm, 10 Hz repetition rate, and laser output energy of 5.2 J/cm^2 (method after D'Oriano et al., 2008; reference values from Jochum et al., 2005). Durango apatite accuracy not shown due to range of reference values.

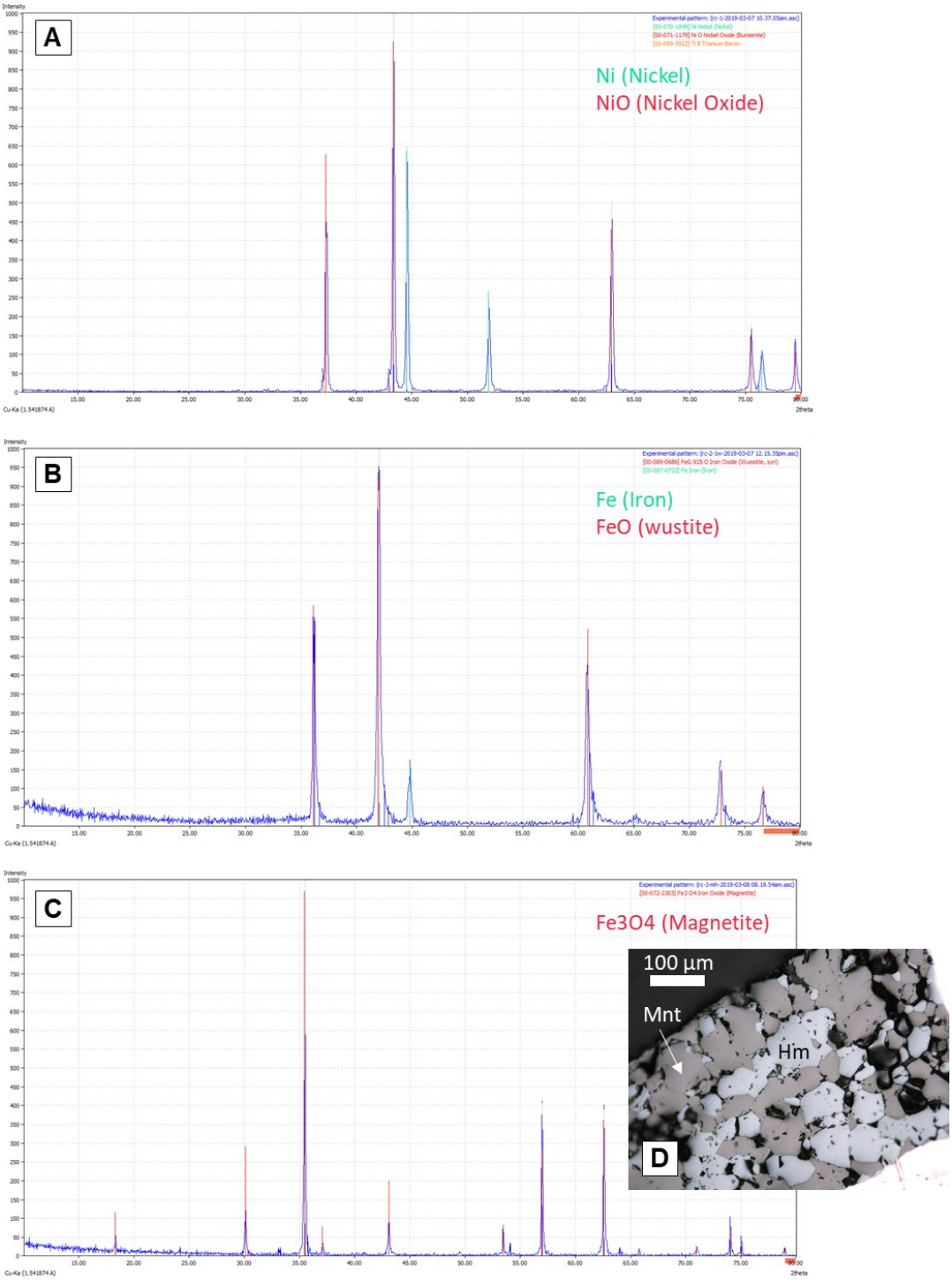

Figure ES 2: XRD patterns of the buffer mixtures after the runs with variable oxygen fugacity. A) Presence of Ni and NiO in run PC-222 with NNO buffer; B) Presence of iron and wustite in run PC-222 with IW buffer; C) Presence of magnetite in run PC-221 with MH buffer. D) Hematite and magnetite presence confirmed in run PC-221 with petrographic microscope.

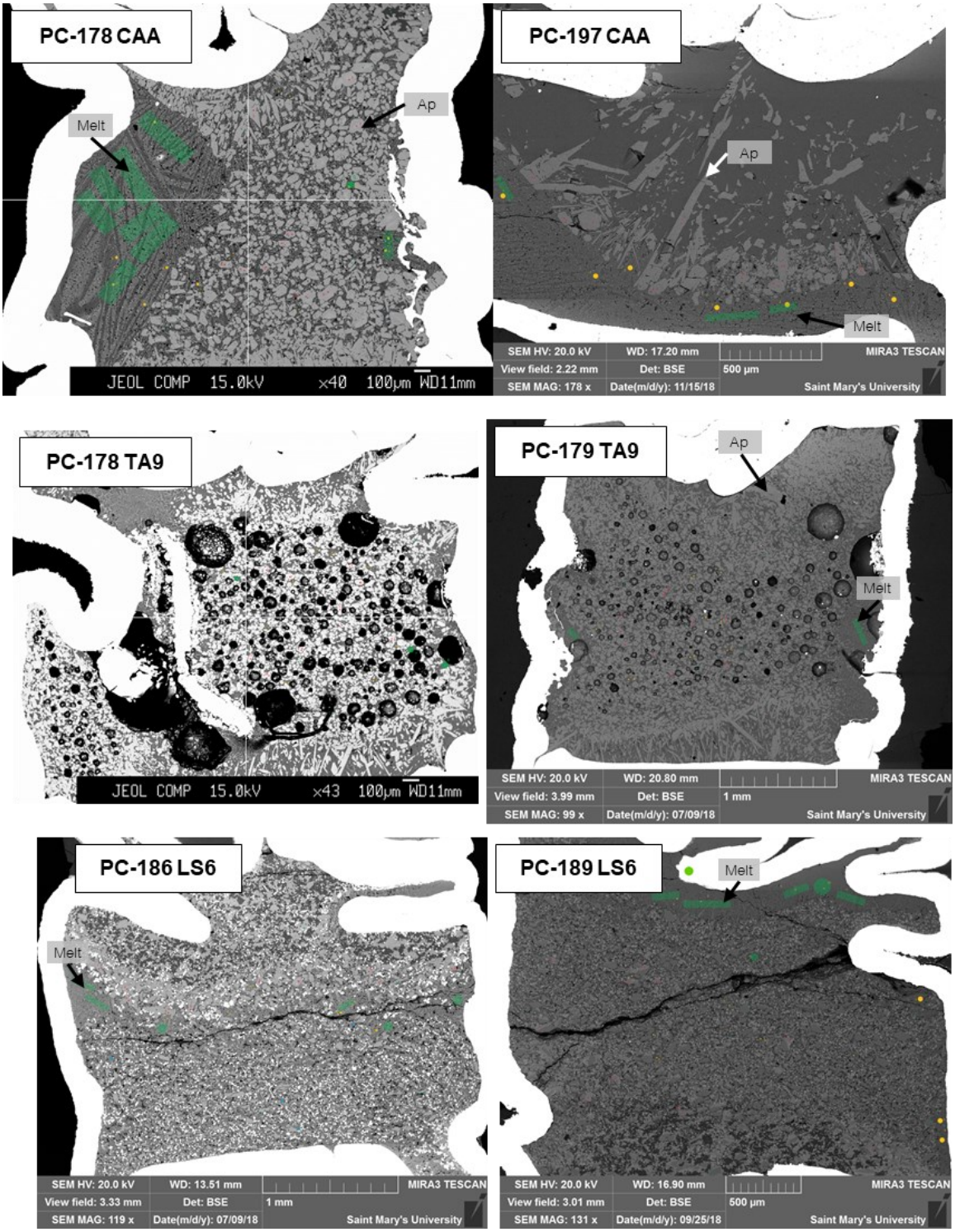

Figure ES 3: BSE images of all the run products showing the areas used for LA-ICP-MS analyses (green areas) and EMP analyses (yellow and red dots).

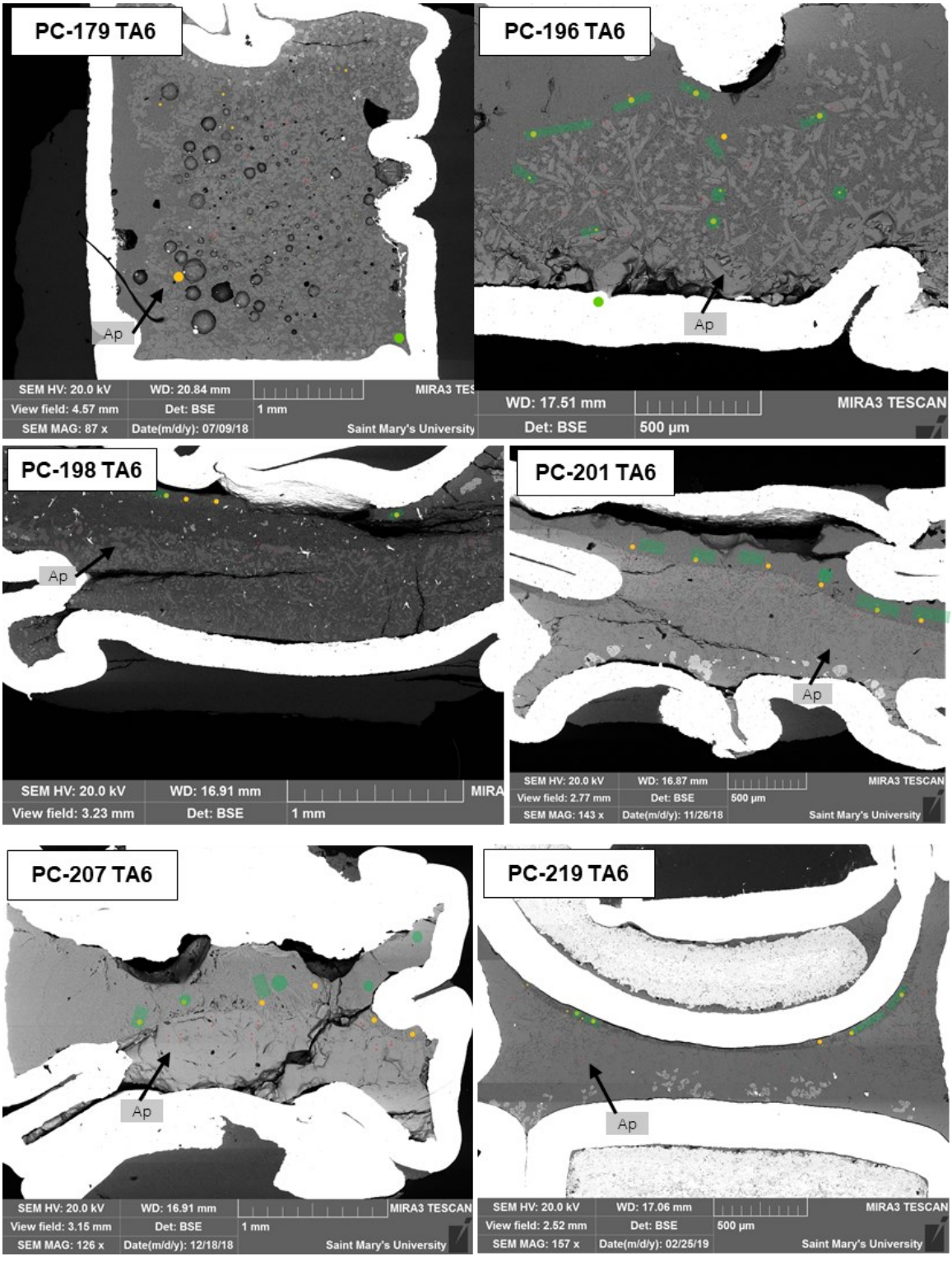

Figure ES 3 Continued: BSE images of all the run products showing the areas used for LA-ICP-MS analyses (green areas) and EMP analyses (yellow and red dots).

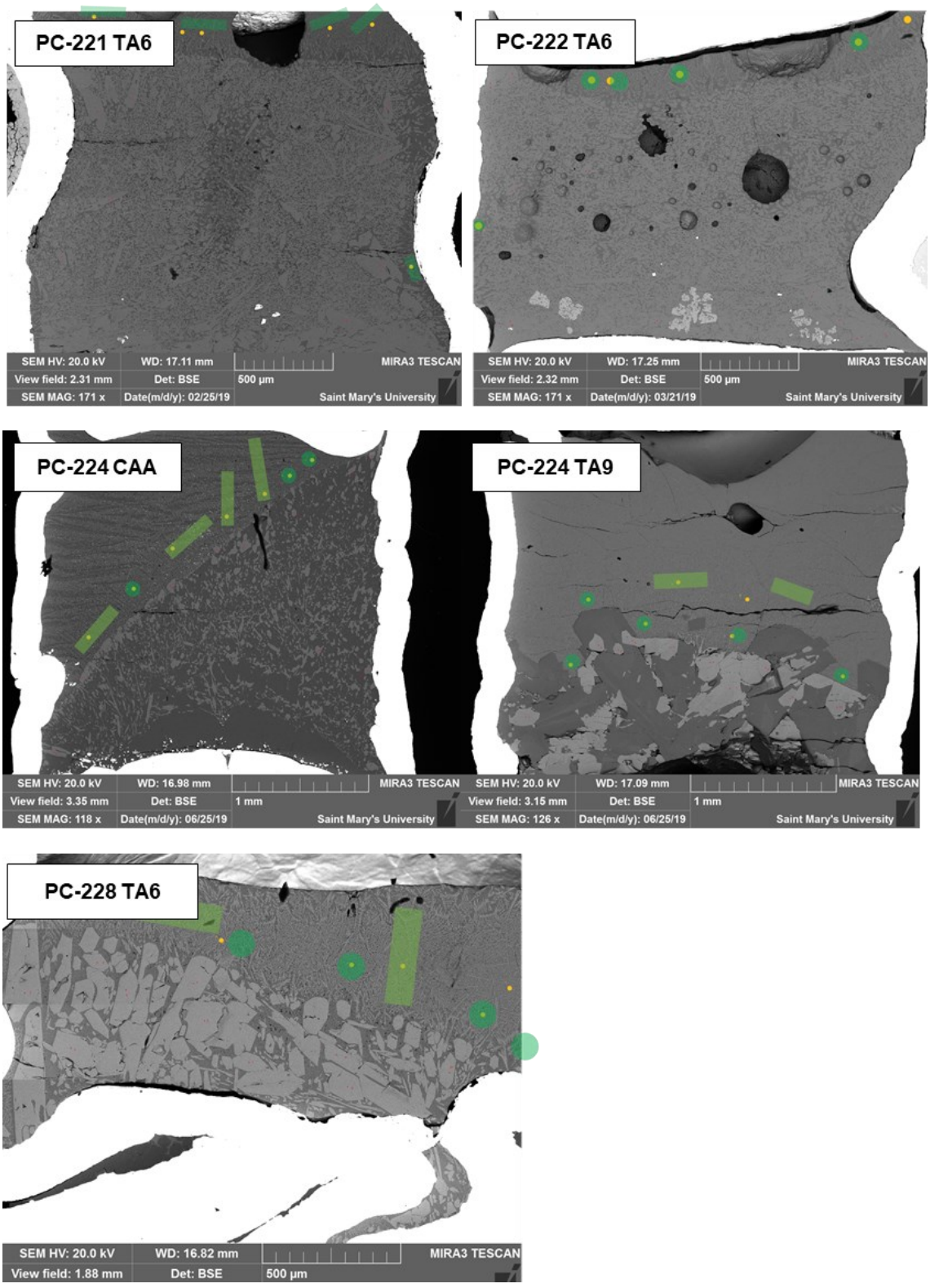

Figure ES 3 Continued: BSE images of all the run products showing the areas used for LA-ICP-MS analyses (green areas) and EMP analyses (yellow and red dots).

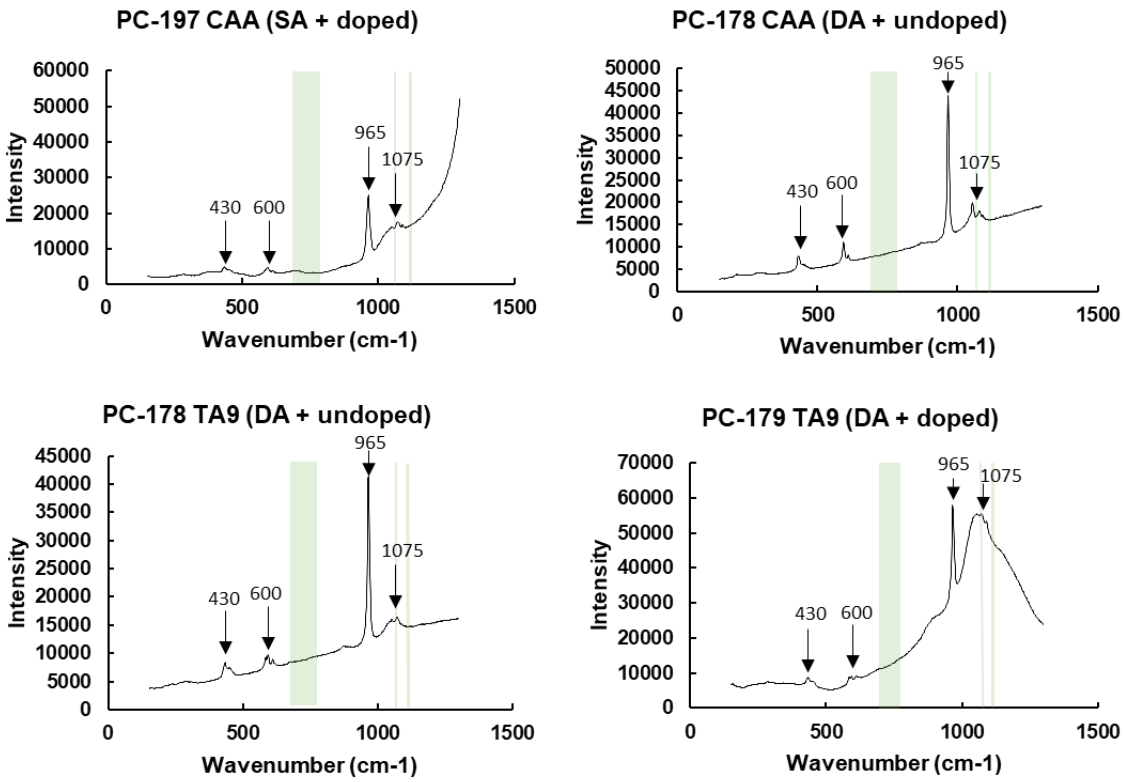

Figure ES 4: Raman spectra of synthetic and Durango apatites in doped and undoped experiments. Doped experiments contain lower totals compared to the normal totals of undoped runs. The arrows indicate the peaks that define apatite. Carbonate peaks have been reported to be present in various apatites at 675-765 cm^{-1}, 1070 ± 1 cm^{-1}, and 1102–1107 cm^{-1} (Chakhmouradian et al., 2017) shown as shaded bars. However, they do not appear as definitive peaks in our samples to be conclusive on the presence of CO_2 incorporated in the structure.

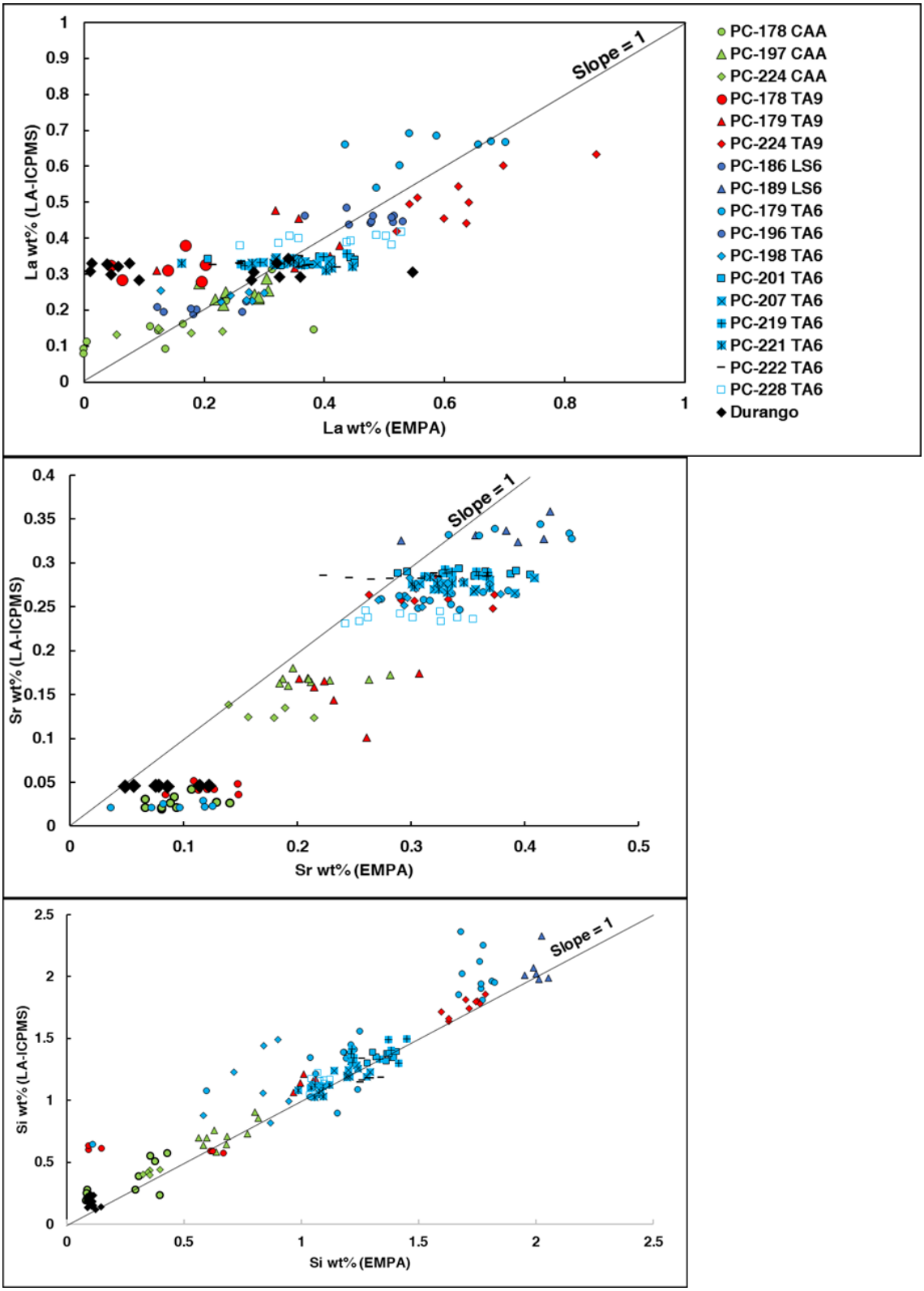

Figure ES 5: Comparison of EMPA and LA-ICPMS analyses of apatite.

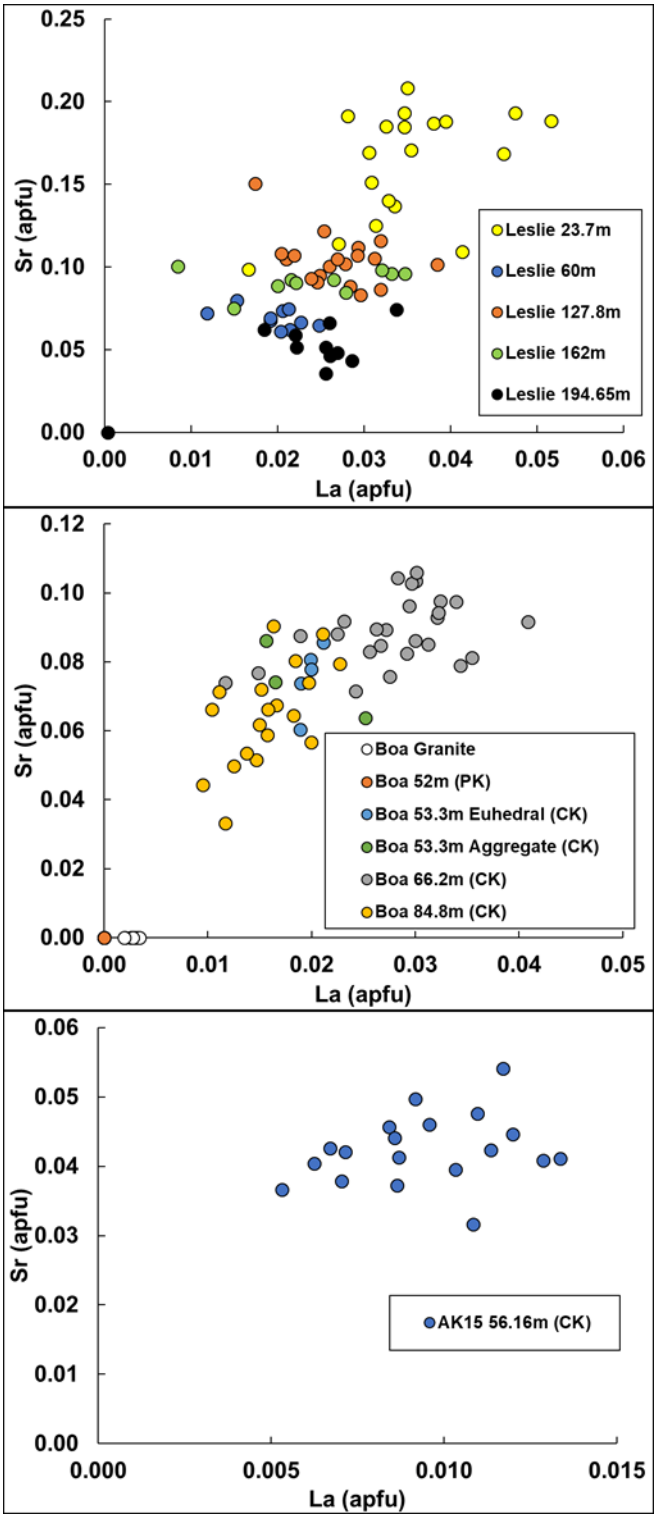

Figure ES 6: La and Sr content in apatite from kimberlite with relation to depth.

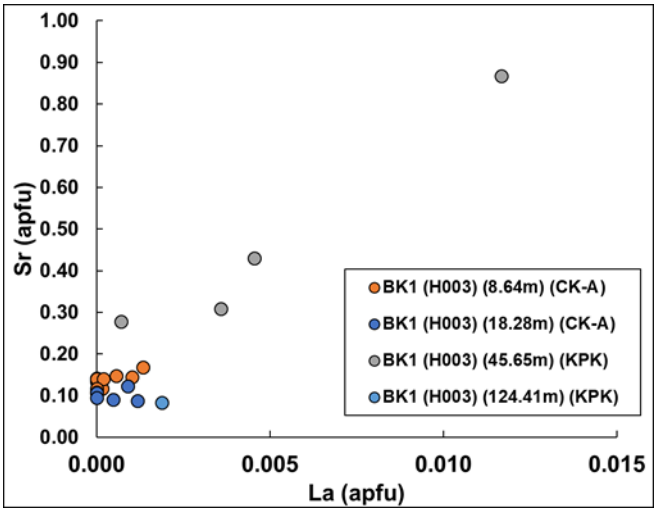

Figure ES 6 Continued: La and Sr content in apatite from kimberlite with relation to depth.

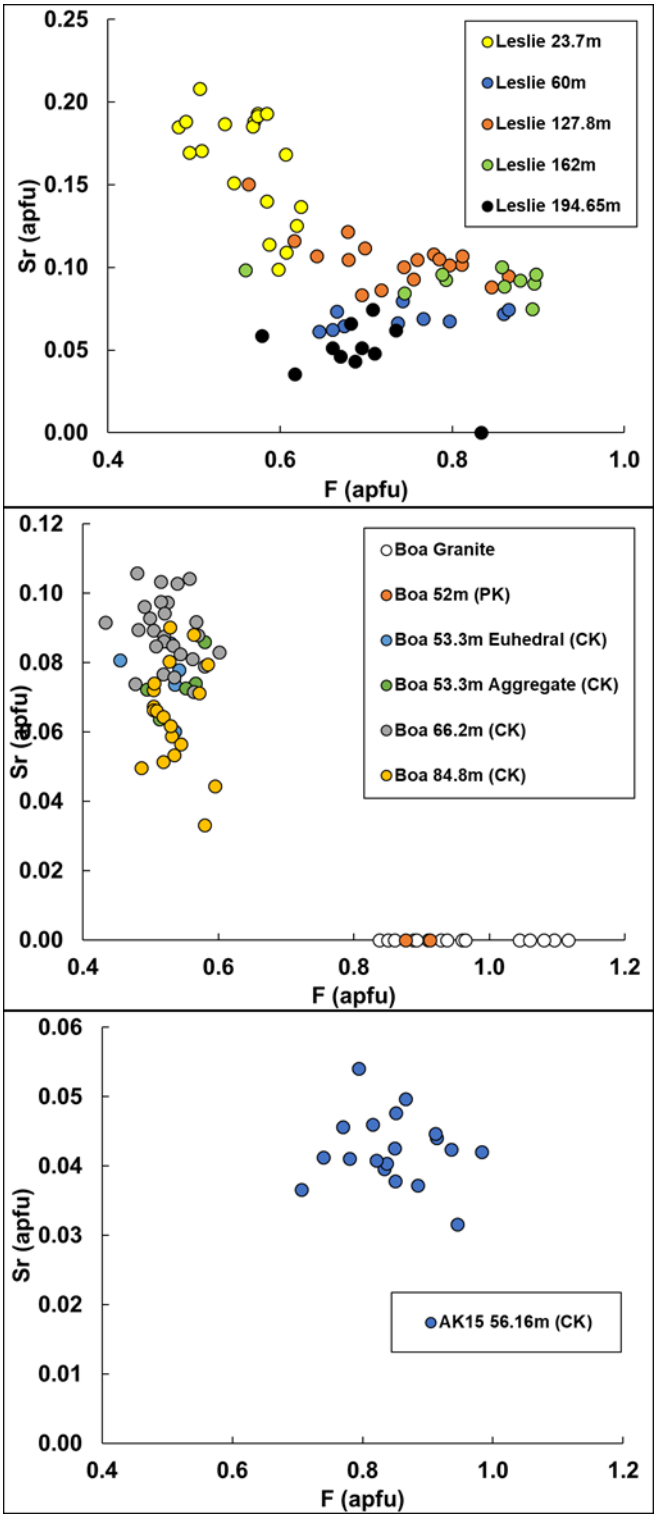

Figure ES 7: F and Sr content in apatite from kimberlite with relation to depth.

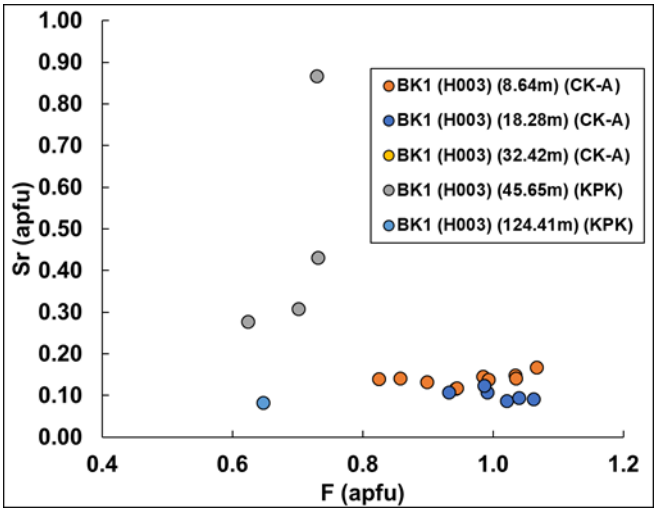

Figure ES 7 Continued: F and Sr content in apatite from kimberlite with relation to depth.

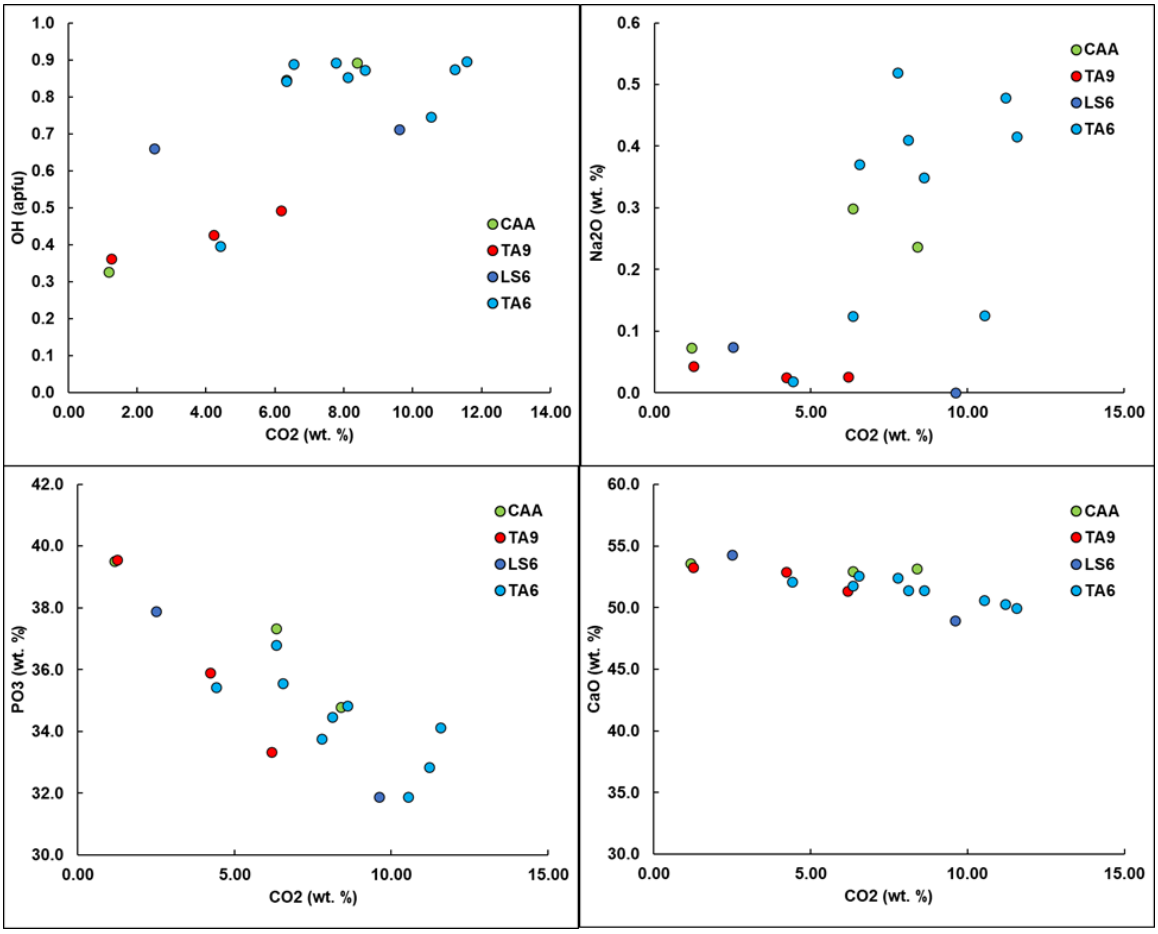

Figure ES 8: Comparison of relationships between presumed carbonate content in apatite (calculated as difference between EPMA total and 100) with various major apatite elements.

Appendix B: Electronic Supplementary Data

Supplementary data in electronic appendix is available through DalSpace, and includes:

1. All major and trace element analyses of natural and experimental apatite from this study
2. All major and trace element analyses of experimental melts
3. Trace element analyses of LA-ICPMS standards